Scanning Capacitance Microscopy in the Quantum Hall Regime

Matthew Edmund Suddards, BSc MRes

Thesis submitted to the University of Nottingham
for the degree of Doctor of Philosophy
July 2007

Contents

Acknowledgements

I would like to thank:

Firstly my supervisor, Chris Mellor for giving me the opportunity to work on this project and for his tuition and encouragement throughout.

The EPSRC and the School of Physics and Astronomy for funding my research.

Andreas Baumgartner for all his advice, 'positive' criticism of drafts of my thesis and sharing his experience when everything in the lab seemed broken!

Fergal Callaghan and Xi Yu for all their work on the project.

The technical support staff especially Malcolm Carter and Pete Smith for all those mechanical jobs I needed yesterday, Bob Chettle and the electronics technicians for help with the various boxes of electronics, Chris Pallender for the provision of liquid Helium and Steve Booth for all his modifications to the probe.

The late Chicken Licken, the late Chicken Bingo, Mrs Wilberforce, Henny Penny and Marilyn although showing little interest in my project provided me with many hours amusement and eggs!

Jill and John for all their support and Jill for proof reading the thesis.

Mum, Kate, Nan, Dad and Mag for their continuing support.

Finally a huge thanks to Baz for everything.

Abstract

This thesis discusses the development of a novel scanning capacitance microscope (SCM) that enables the investigation of the local capacitance and conductivity of surfaces and near-surface nanostructures at cryogenic temperatures and high magnetic fields.

Simultaneous atomic force microscopy (AFM) and SCM measurements can be made at a temperature of 1.5 K and a magnetic field of 12 T. The AFM/SCM sensor is based on a quartz-tuning fork with an etched metal tip. SCM measurements are made using an RF tuned filter design which allows changes in capacitance to be measured with sub-attofarad resolution and a bandwidth of 200 Hz.

Test measurements were made over an evaporated gold film. The capacitance distance curve was recovered from the measured quantities using a deconvolution scheme normally used for force-distance curves.

Measurements have been made of a two-dimensional electron gas in the quantum Hall effect (QHE) regime. Highly conductive stripes form near the edge of the sample at integer Landau level filling factors in agreement with theoretical predictions. These measurements are the first direct imaging of the compressible stripes at the physical edge of a Hall bar device. Measurements were also made by point spectroscopy in a region that was locally depleted. Around this region a ring-shaped stripe of considerably larger width than at the sample edge is observed. The increased width was explained in terms of a shallower potential gradient compared to the physical edge of the sample.

Preliminary measurements have demonstrated that the microscope is capable of imaging edge states whilst passing current through the device.

Chapter 1

Introduction

1.1 The quantum Hall effect

The quantum Hall effect (QHE) is a fascinating macroscopic quantum phenomenon which occurs in two-dimensional electron gases (2DEG) at low temperatures and strong perpendicular magnetic fields. It was discovered in 1980 when Klaus von Klitzing was investigating the properties of a Si-MOSFET device at low temperature and high magnetic fields [1]. The QHE is characterized by plateaus in the Hall resistance at integer multiples of e^2/h. The amazing result is that this quantization is accurate to one part in ten million and is indifferent to disorder, or sample geometry. At corresponding magnetic fields the longitudinal resistance falls to zero, indicating a dissipationless flow of current. In 1985 von Klitzing was awarded the Nobel prize for his discovery.

The behaviour of charged particles in a magnetic field is important in a wide range of fields, for example high-energy physics, atomic physics and astrophysics. Since the discovery of the quantum Hall effect in 1980, more than 7000 publications have been written on the subject. There are publications linking the QHE to the physics of quarks [2], black hole theories [3] and string theory [4]. The main application of the QHE is as a resistance standard [5].

In spite of the extensive experimental and theoretical work, some fundamental questions remain, (for example, the influence of the device edges or the mechanism behind

the breakdown at high currents [6]).

The quantum Hall effect is discussed in detail in Chapter 2.

1.2 Scanning probe microscopy

The invention of the first optical microscope 400 years ago increased understanding of the world by enabling objects too small to be visible to the eye to be seen for the first time. Since its invention the magnification of the microscope has increased from a few hundred to nearly a million. In 1980 the scanning probe microscope was invented. This technique measures an interaction between a sharp probe and a surface and enables the measurement of physical properties of materials on a nanometre scale.

The first example of a scanning probe microscope (SPM) was the scanning tunnelling microscope (STM), which was invented in 1982 by Binnig and Rohrer [7]. The STM measures the tunnel current between a sharp conductive tip and a conductive sample. Within a year of its discovery atomic resolution of the silicon 7×7 reconstruction was achieved [8]. This marked a watershed in microscopy techniques as it was now possible to image surfaces at the atomic level in three dimensions. A whole family of scanning probe microscopes has been developed enabling a huge range of local properties to be measured.

Atomic resolution on the surfaces of solids [9] and force spectroscopy of single chemical bonds have been demonstrated using atomic force microscopy (AFM) [10]. Scanning near-field optical microscopy (SNOM) has been used to measure the optical spectra of single molecules [11] and perform lithography on a molecular scale [12]. The STM can be used to manipulate single atoms or molecules [13]. Magnetic force microscopy can be used to investigate magnetic structure on data storage devices [14].

Scanning probe microscopy is discussed in detail in Chapter 3.

1.3 Overview of thesis

This thesis discusses the development of a low-temperature scanning capacitance microscope and measurements made of the quantum Hall effect. The structure of the thesis is as follows: Chapter 2 gives a short introduction to the physics of two-dimensional electron gases focusing on electron transport in GaAs/AlGaAs heterostructures at high magnetic fields. Chapter 3 gives an overview of scanning probe microscopy. In Chapter 4 the development of the low-temperature scanning probe microscope is described. In Chapter 5 the capacitance detection scheme is described. In Chapter 6 measurements over a gold film are discussed. In Chapter 7 measurements of a near surface 2DEG at zero field and in the quantum Hall regime are presented. Chapter 8 contains a brief summary and suggestions for future work.

Chapter 2

The Quantum Hall Effect

2.1 Introduction

The quantum Hall effect (QHE) is observed in a two-dimensional electron gas (2DEG) at low temperature and high magnetic field. The effect was discovered in 1980 by Klaus von Klitzing whilst investigating the transport properties of a Si-MOSFET device [1].

Figure 2.1(a) is a schematic diagram of transport measurements made on a Hall bar. A current I flows in a 2DEG of width W with a magnetic field B applied perpendicular to the plane of the sample. A longitudinal voltage V_{xx} is measured between two voltage probes separated by a distance L. At the same time, the transverse or Hall voltage V_H is measured. Figure 2.1(b) shows a typical measurement of the longitudinal resistance $R_{xx} = \frac{V_{xx}}{I}$ and Hall resistance $R_H = \frac{V_H}{I}$ for a GaAs heterostructure sample as a function of magnetic field at low temperature. The classical Drude model predicts that the longitudinal resistance should be independent of field and that the transverse or Hall resistance should increase linearly with field. At low temperatures and low magnetic fields the behaviour of the 2DEG is described by the classical model. At high fields the longitudinal resistivity oscillates with $1/B$ periodicity and plateaus appear in the Hall resistance. The two main features of the QHE effect are plateaus in the Hall resistance at $R_H = \frac{1}{n}\frac{h}{e^2}$ (where $n = 1, 2, 3, 4 \ldots$), and at corresponding fields the longitudinal resistance falls nearly to zero.

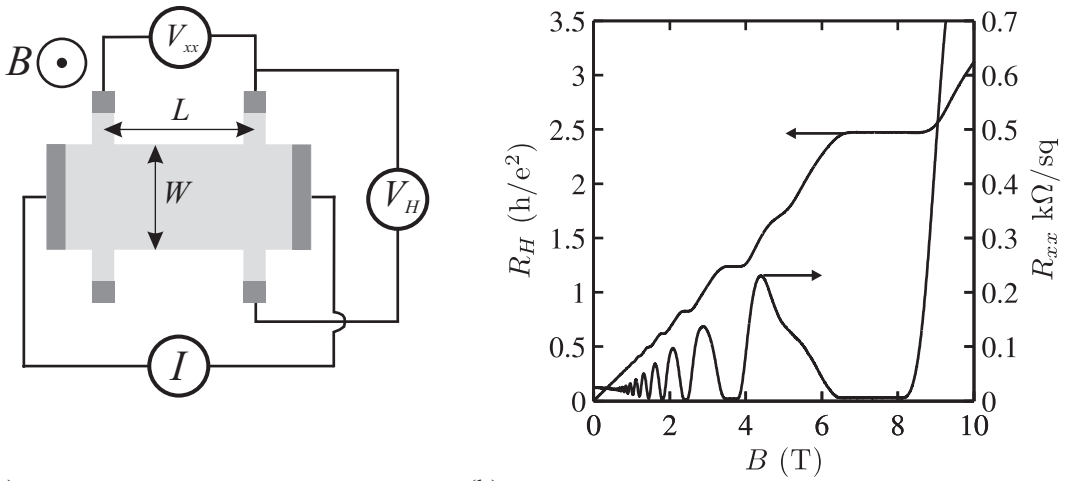

(a) (b)

Figure 2.1: (a) Schematic showing transport measurements with a Hall bar geometry. (b) A typical magnetoresistance measurement for a GaAs heterostructure at low temperature.

The quantization of the Hall resistance has been shown to be independent of host material, device and plateau number at a level of a few parts in 10^{10}. Since 1990 the QHE has been used as a secondary standard of electrical resistance [5].

2.2 Formation of 2DEG in a GaAs heterostructure

In a 2DEG the electrons are quantum mechanically confined in one spatial direction. A 2DEG can be formed in a number of types of system, including electrons trapped on the surface of liquid He below 2.2 K, metal-oxide-semiconductor space charge layers, and semiconductor heterostructures. The systems used in this work are GaAs/AlGaAs heterostructures grown by MBE [15]. These two materials have different band gaps which results in a 2DEG accumulating at their interface.

A layer of GaAs a few μm thick is grown onto a GaAs(100) wafer, followed by a layer of $Al_{0.3}Ga_{0.7}As$. The interface between these two layers is where the 2DEG is formed. A spacer layer of AlGaAs is then grown into which the dopants are added before a further layer of GaAs is deposited. Finally, a capping layer of GaAs is grown to protect the structure. Separating the dopants from the 2DEG by a spacer layer is

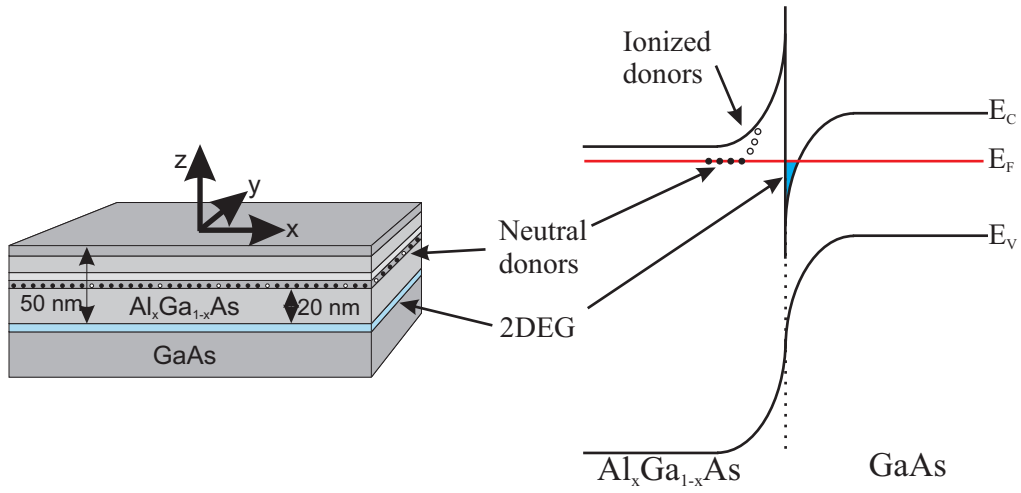

Figure 2.2: (a) Schematic of the layers in a heterostructure used to form a 2DEG. (b) Band diagram at the heterojunction between AlGaAs and GaAs. Figure from [16].

called modulation doping. This technique reduces Coulomb scattering, with the aim of increasing the mobility. The donors can be introducing over a number of layers referred to as volume doping or to a single monolayer known as δ-doping.

Figure 2.2 shows the layer structure and band diagram of a near surface 2DEG heterostructure. A ratio of gallium to aluminium of 7:3 in AlGaAs gives a crystal structure with a lattice constant nearly identical to GaAs, enabling an atomically sharp interface to be realised without distorting the lattice. The difference in the band gap between the two materials introduces a discontinuity in the conduction band at the interface. Donors in the AlGaAs layer are easily ionized and some of these donor electrons diffuse into the GaAs setting up a potential gradient. The potential gradient from the migration of donor electrons and the band gap discontinuity creates a triangular potential well in the conduction band [17]. At low temperature electrons are confined in the growth direction but are free to move orthogonally and form a 2DEG. They occupy states within a two-dimensional Fermi circle of radius k_F. The density of states in two dimensions is given by [17]:

$$\frac{dn}{dE} = \frac{4\pi m^*}{\hbar^2} \tag{2.1}$$

where m^* is the effective mass. Note that the density of states is independent of energy unlike the three-dimensional case. In the following section the effect of a magnetic field perpendicular to the interface is explored.

2.3 Electron wavefunctions in a magnetic field

2.3.1 Classical analogy

Classically, electrons in a uniform magnetic field **B** execute circular trajectories in the plane normal to the field whilst motion parallel to **B**, defined as the z-axis, is unaffected. The circular trajectories are known as cyclotron orbits and have a constant angular frequency ω_c, known as the cyclotron frequency:

$$\omega_c = \frac{eB}{m^*} \tag{2.2}$$

and an orbit radius R_c, known as the cyclotron radius:

$$R_c = \frac{\sqrt{2m^* E_K}}{eB} \tag{2.3}$$

where E_K is the kinetic energy.

In this classical description the angular frequency is independent of the energy whilst the amplitude is proportional to the energy. This behaviour is reminiscent of a harmonic oscillator and this will be reflected in the quantum-mechanical results derived in the next section.

2.3.2 Quantum-mechanical description

In this section the solution of the Schrödinger equation is considered for independent two-dimensional spinless electrons in a magnetic field. The following derivation can be found in various forms in the literature and in the following section the method presented by Prange is summarised [18].

The Schrödinger equation for a single electron in an electromagnetic field is given by:

$$\left[\frac{1}{2m}(i\hbar\vec{\nabla} + e\vec{A})^2 + V\right]\Psi = E\Psi \tag{2.4}$$

where V is the electric potential and $\vec{A}$ is the vector potential of the magnetic field [19]. For a 2DEG with no boundaries and the growth direction defined as the z-axis then $V(x,y) = 0$ and $V(z)$ is the potential well confining the electrons. For a magnetic field in the z-direction (perpendicular to the interface) and using the Landau gauge for the vector potential, in which $\vec{A} = (0, Bx, 0)$, the Schrödinger equation can be rewritten as:

$$-\frac{\hbar^2}{2m^*}\frac{\partial^2\Psi_{xy}}{\partial x^2} + \frac{1}{2m^*}\left(-i\hbar\frac{\partial}{\partial y} + eBx\right)^2\Psi_{xy} = E\Psi_{xy} \tag{2.5}$$

expanding the inner bracket:

$$\left[-\frac{\hbar^2}{2m^*}\nabla^2 - \frac{ie\hbar Bx}{m^*}\frac{\partial}{\partial y} + \frac{(eBx)^2}{2m^*}\right]\Psi_{xy} = E\Psi_{xy} \tag{2.6}$$

The magnetic field produces two terms: a parabolic term which tends to confine the wavefunctions in x, and a first derivative which couples x and y, analogous to the Lorentz force.

The vector potential does not depend upon y which suggests that the wavefunction should be a product of a plane wave in y with an unknown function of x. Substituting $\Psi_{xy} = \exp(iky)\psi(x)$ then:

$$\left[-\frac{\hbar^2}{2m^*}\frac{d^2}{dx^2} + \frac{1}{2}m^*\omega_c^2\left(x + \frac{\hbar k}{eB}\right)^2\right]\psi(x) = E\psi(x) \tag{2.7}$$

Equation 2.7 has the same form as the one-dimensional harmonic oscillator equation with the motion centred at the point $x_k = -\hbar k/eB$. The length scale is the magnetic length $l_B = \sqrt{\hbar/eB}$ and is of the order 50-100 Å. Note that this is independent of material properties. The energies and wavefunctions for the motion in the xy plane are then given by:

$$E_{nk} = \left(n + \frac{1}{2}\right)\hbar\omega_c \tag{2.8}$$

$$\psi_{nk}(x,y) \propto H_{n-1}\left(\frac{x - x_k}{l_B}\right)\exp\left[-(x - x_k)^2/2l_B^2\right]\exp(iky) \tag{2.9}$$

where $n = 1, 2, 3\ldots$ and H_n are Hermite polynomials.

The energy depends only on n not k and the constant density of states found at zero field collapses into a series of δ-functions with energies given by Eqn. 2.8. These are known as Landau levels (LLs). The wavefunctions are plane waves in the y-direction with different k values spatially separated in the x-direction. The spread of the wavefunction in the x-direction Δx_k is given by magnetic length l_B which depends on the magnetic field.

The distinction between x and y is due to the choice of gauge, it would have been possible to choose a circularly symmetric vector potential and this symmetry would have been reflected in the wavefunctions. Irrespective of the choice of gauge the eigenvalues and underlying physics are the same.

Consider a sample with dimensions $L_x \times L_y$, using periodic boundary conditions then the k vectors of the plane waves in the y-direction are separated by $\Delta k = 2\pi/L_y$ and the separation in x is $\Delta x_k = \frac{\hbar \Delta k}{eB}$ therefore the total number of states N is given by:

$$N = \frac{L_x}{\Delta x_k} = \frac{eB}{h} L_x L_y \tag{2.10}$$

or that the number of states per unit area of a full Landau level $n_L = eB/h$. These definitions do not include a factor of two for spin as the up and down spin states are not degenerate in a magnetic field.

As the magnetic field increases, the separation in energy between the Landau levels increases but so too does the number of states in each Landau level. The density of states averaged over a number of Landau levels remains the same as in the zero field case. The effect of the magnetic field is to condense the continuous distribution of energies into discrete Landau levels.

Most experiments are carried out with a constant density of electrons, n_s, and as a result the number of occupied Landau levels changes with magnetic field. The number of occupied Landau levels is called the filling factor, ν, and is given by:

$$\nu = \frac{n_s}{n_L} = \frac{h}{eB} n_s \tag{2.11}$$

At integer filling factors then $n_s = \frac{eB}{h}$. Substituting this into the expression for the classical Hall effect [20] $R_H = B/en_s$ this gives $R_H = \frac{h}{ie^2}$ as in the experiments. This

can explain why the quantum Hall effect is seen for specific values of magnetic field but it cannot explain the presence of plateaus in the Hall resistance. The plateaus are a consequence of disorder in the system which is discussed in the next section.

2.4 Effect of disorder

The results so far are for an ideal system with no scattering. In a real sample defects cause scattering and potential fluctuations which result in the Landau levels acquiring a characteristic width Γ. This can be estimated from the scattering time τ where Γ is given by [17]:

$$\Gamma = \frac{\tau}{\hbar} \tag{2.12}$$

Prange solved the Schrödinger equation with the addition of a single δ-function impurity potential [21]. The result of this is that each Landau level has a single localized state with an energy well above or below the Landau level energy. This localized state carries no current. Extending this to a system of many defects or other potential fluctuations, and in a sufficiently strong magnetic field, then the Landau levels will be broadened into a band. The central part of the band consists of extended states and away from this in the tails of the distribution there are localized states which cannot carry current.

At low magnetic fields the separation of the Landau levels is smaller than their characteristic width and they overlap forming a continuous density of states, see Fig. 2.3(a). At high magnetic fields then the Landau levels are well separated, the extended states are found at the centre of the Landau levels and the localized states in the tails of the distribution, see Fig. 2.3(b). The density of states is high in the centre of the Landau levels and low in the gaps between Landau levels. At the highest magnetic fields then spin splitting of the Landau levels into two sublevels is observed, see Fig. 2.3(c).

The density of states at the Fermi energy depends upon the filling factor. At integer filling factors the Fermi energy lies in a gap between Landau levels where the density of states is low. At half integer filling factors the Fermi level lies in the centre of a

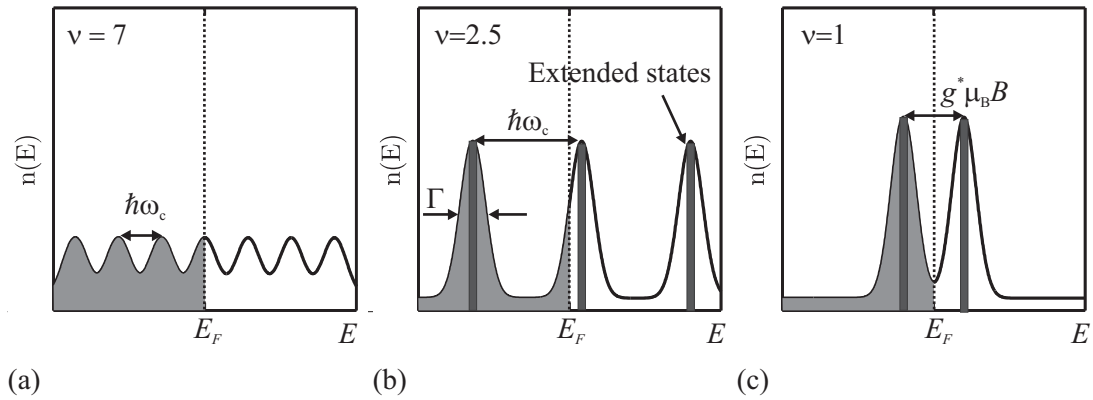

Figure 2.3: The DOS of a 2DEG in a magnetic field. (a) At low magnetic fields the separation of the Landau levels is smaller than their width. (b) At high magnetic fields the Landau levels are well separated. The centre of the Landau bands are populated by extended states (dark shading) and the tails by localized states. (c) At the highest fields then spin splitting means that the Landau levels split into two sublevels.

Landau level where the density of states is high. A number of observable properties of a 2DEG depend on the DOS at the Fermi energy, including, the heat capacity [22] and conductivity. As a result these depend strongly upon filling factor.

At zero temperature the only states that can carry current are the extended states. As the Fermi energy passes through the region of localized states the occupation of extended states does not change. These are the only states to carry a current and as a result the Hall resistance will not change giving rise to a plateau. Simultaneously the longitudinal resistance vanishes as only localised states are in the vicinity of the Fermi energy. As the Fermi energy approaches the next Landau level then the longitudinal resistance becomes finite and the Hall resistance makes the transition to the next plateau.

This argument is missing one important detail. If some of the electrons are tied up in localized states then it is incorrect to use the number of states in a Landau level as the total number of carriers. If this was a factor then the Hall resistance would depend upon the degree of disorder in a given sample, something which is not observed experimentally. However, it has been shown that electrons passing an impurity speed

up and this effect is able to compensate for electrons trapped in localised states [18]. A more general argument by Laughlin [23] and later refined by Halperin [24] used gauge invariance and the conservation of energy to show that the extended states carry more current but without reference to a specific mechanism.

Without disorder the quantized Hall resistance would only be seen at exact filling factors and not at range of values. Prange [18] discusses an argument based upon relativistic transformations. It is possible to show that some breaking of translational invariance, either by disorder or the sample boundaries, is necessary to observe the quantum Hall effect. The quantum Hall effect would not be observed in an infinite and defect-free 2DEG.

2.5 Edge states

The analysis so far has considered a 2DEG with no boundaries whereas in real measurements finite samples are of course used. Halperin was the first to realise the importance of the sample edges [24] and, in combination with the Landauer formalism, made the edge state approach a very efficient description of transport at high magnetic fields [25].

Consider a narrow channel where the 2DEG is confined in the x-direction and free in the y-direction. This can be described by a potential $V(x)$. Note that each wavefunction is centred around a different location $x = x_k$ (see Eqn. 2.7). Assuming the potential varies slowly on the length scale of the wavefunction then a good approximation for the energy is given by

$$E(n,k) = (n+1)\hbar\omega_c + V(x_k) \tag{2.13}$$

where $x_k = -\hbar k/eB$. The effect of the edges is to break the degeneracy of the Landau levels. States in the centre of the sample have the same energy as an unconfined system whilst the energy of states near the edges is increased. The states near the edges have a continuous distribution of energies and are referred to as 'edge states'.

The group velocity of a state $v_{n,k}$ is given by [26]:

$$v_{n,k} = \frac{1}{\hbar}\frac{\partial E(n,k)}{\partial k} = \frac{1}{\hbar}\frac{\partial V(x)}{\partial x}\frac{\partial x_k}{\partial k} = \frac{1}{eB}\frac{\partial V(x)}{\partial x} \tag{2.14}$$

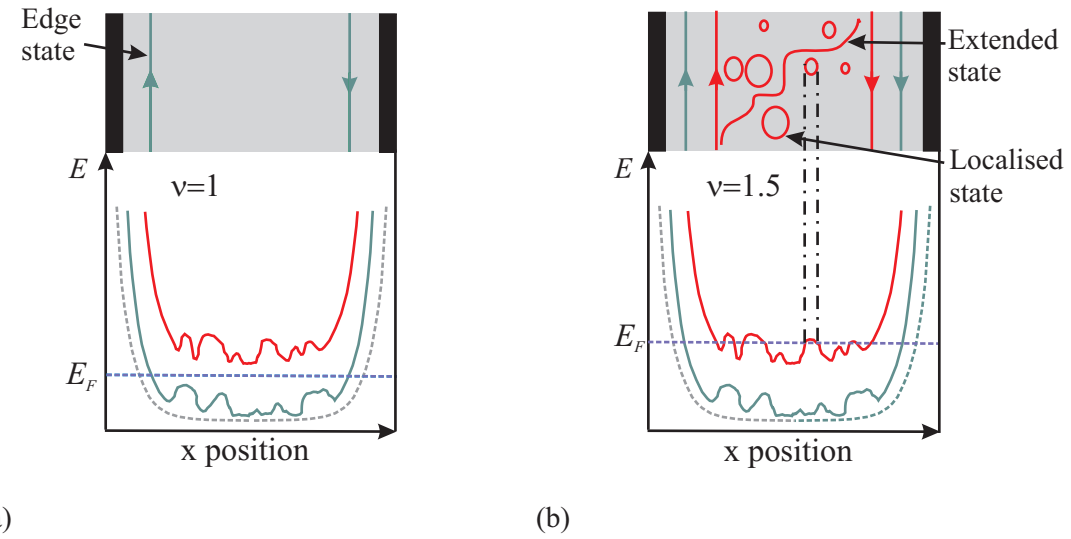

Figure 2.4: Distribution of states at the Fermi energy at different filling factors ν. Upper pane shows a top view of the plane of the 2DEG indicating the spatial location of states at the Fermi energy. Lower pane shows the energy of the Landau levels as a function of position across a narrow channel and indicates the intersection of the Landau levels with the Fermi energy. (a) At integer filling factors the only states at the Fermi energy are at the edges. (b) At non-integer filling factors states at the Fermi energy include localised states in the bulk.

The edge states have a non-zero group velocity and therefore carry a current. The two edges carry currents in opposite directions, since the quantity $\frac{\partial V(x)}{\partial x}$ changes sign. With no external potential the currents at opposite edges cancel out.

Consider the effect of filling factor upon the distribution of states at the Fermi energy. At integer filling factors the Fermi energy lies between Landau levels, and states at the Fermi energy are located at the edges, see Fig. 2.4(a). States carrying current in opposite directions are spatially separated, the overlap of their wavefunctions is extremely small making scattering between them unlikely, as a result backscattering is suppressed. This explains the strong minima in the longitudinal resistance at integer filling factors.

At non-integer filling factors the Fermi energy lies in a bulk Landau level. Local potential fluctuations mean that states at the Fermi energy exist in the bulk, these can either be localized around a local defect or can form extended states which connect

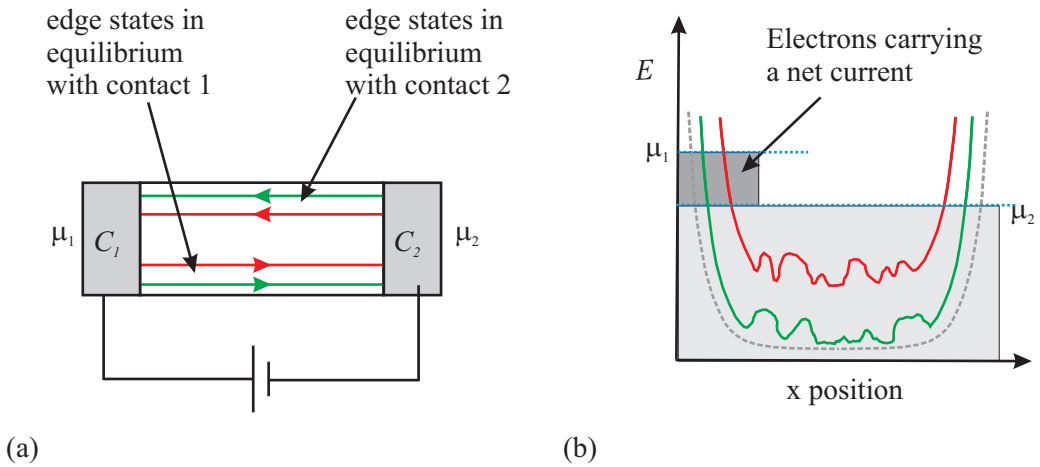

Figure 2.5: (a) A conductor in the quantum Hall regime. The edge states carrying current to the right are in equilibrium with the left contact while those carrying current to the right are in equilibrium with the right contact (based upon [26]). (b) Occupation of the Landau levels illustrating that net current is carried by electrons between μ_1 and μ_2.

the two edges, see Fig. 2.4(b). This distribution of allowed states between the two edges means that backscattering is not suppressed and a finite longitudinal resistance is measured.

Quantization of the Hall resistance

In this section the quantization of the Hall resistance is briefly described in terms of the theory of edge states. This follows the approach of Buttiker [25]. Consider the case where the sample is connected by ideal contacts to two reservoirs with chemical potential μ_1 and μ_2, see Fig. 2.5(a). If $\mu_1 > \mu_2$ as in Fig. 2.5(b) then all the states below μ_2 are occupied (assuming $T = 0$) and do not carry any net current. Any net current arises from the states between μ_2 and μ_1. At integer filling factors backscattering is suppressed which means electrons originating in C_1 (see Fig. 2.5(a)) enter the edge states carrying current to the right and empty into C_2, while electrons originating in C_2 enter the edge states carrying current to the left and empty into C_1. Edge states carrying current to the right are in equilibrium with C_1 and edge states carrying current to the left are in equilibrium with C_2. Clearly the longitudinal voltage drop

V_{xx} measured between two voltage probes on the same edge of the sample is zero, while the Hall voltage, V_H, is equal to the applied potential.

$$V_{xx} = 0 \text{ and } V_H = \frac{\mu_1 - \mu_2}{e} \tag{2.15}$$

In the absence of scattering, the current carried by a single edge state $\nu = n$ is given by:

$$I_n = ev_n \left[\frac{dn}{dE}\right]_n (\mu_1 - \mu_2) \tag{2.16}$$

For a 1-dimensional channel, the density of states in k-space is $dn/dk = 1/2\pi$ therefore

$$\frac{dn}{dE} = \frac{1}{2\pi}\frac{dk}{dE} = \frac{1}{2\pi\hbar v_n} \tag{2.17}$$

where the density of states $D(E) = 2\pi\hbar v_n$ is the same as a 1D channel. The number of edge states is the same as the number of occupied Landau levels in the bulk, ν, the filling factor. Substituting into Eqn. 2.16 then:

$$I = \nu\frac{e}{h}\Delta\mu \tag{2.18}$$

The Hall resistance R_H is then given by:

$$R_H = \frac{V_H}{I} = \frac{h}{e^2}\frac{1}{\nu} \tag{2.19}$$

Equation 2.19 has the same form as the quantized resistance of ballistic conductors with the number of edge states equivalent to the number of modes. The quantization in a ballistic conductor is not precise because backscattering is not completely suppressed.

In the derivation of the Hall resistance there are two conflicting boundary conditions. The left and right contacts are at chemical potentials of μ_1 and μ_2 respectively and the top and bottom edges are at chemical potentials of μ_2 and μ_1. Buttiker resolves this problem by introducing a disordered region between the contacts and the 2DEG. The chemical potential is then dropped across this disordered region and equipotentials form along the remainder of the sample.

2.6 Compressible and Incompressible stripes

The model of edge states presented so far is a single electron picture. In this model the Landau levels are moved up in energy by the confining potential and the position of the edge states is then given by the intersection of the Landau levels with the Fermi level. The Landau levels are well separated and the electron density increases from zero at the edge in steps of $n_L = \frac{eB}{h}$. The local filling of the Landau levels and the electron density as a function of distance to the edge are shown in Figs. 2.6(a), 2.6(b).

The discontinuities in the electron density are very unphysical as they indicate regions of high electric field which mobile carriers would be expected to screen.

Coulomb interactions were considered by Chklovskii *et al* [27] using self consistent descriptions of the edge potential. They found that the sample divided into incompressible and compressible strips. The argument presented in Ref. [27] is summarized below.

At zero field the electron density increases smoothly from zero at the edge to the bulk value n_s and has the form:

$$n(x) = \left(\frac{x - l_d}{x + l_d}\right)^{1/2} \text{ for } x > l_d \tag{2.20}$$

where l_d is the depletion length and for an etched structure can be approximated by [28]:

$$l_d \approx \frac{4V_g \epsilon \epsilon_0}{\pi e n_s} \tag{2.21}$$

where V_g is the band gap potential. This expression is plotted as a dashed line in Fig. 2.6(d).

In a magnetic field the electron distribution obtained from the electrostatics (Eq. 2.20) would not be expected to alter significantly. This is because of the huge amount of work that would need to be performed against the electric field. The electron distribution in a magnetic field with a self consistent approach is shown in Figs. 2.6(c) and 2.6(d).

The energy gap between the Landau levels means that the electrostatic solution derived at zero field is no longer the lowest energy state. In regions where there is a transition between filling one Landau level and the next, for example at x_1 in Fig. 2.6(c),

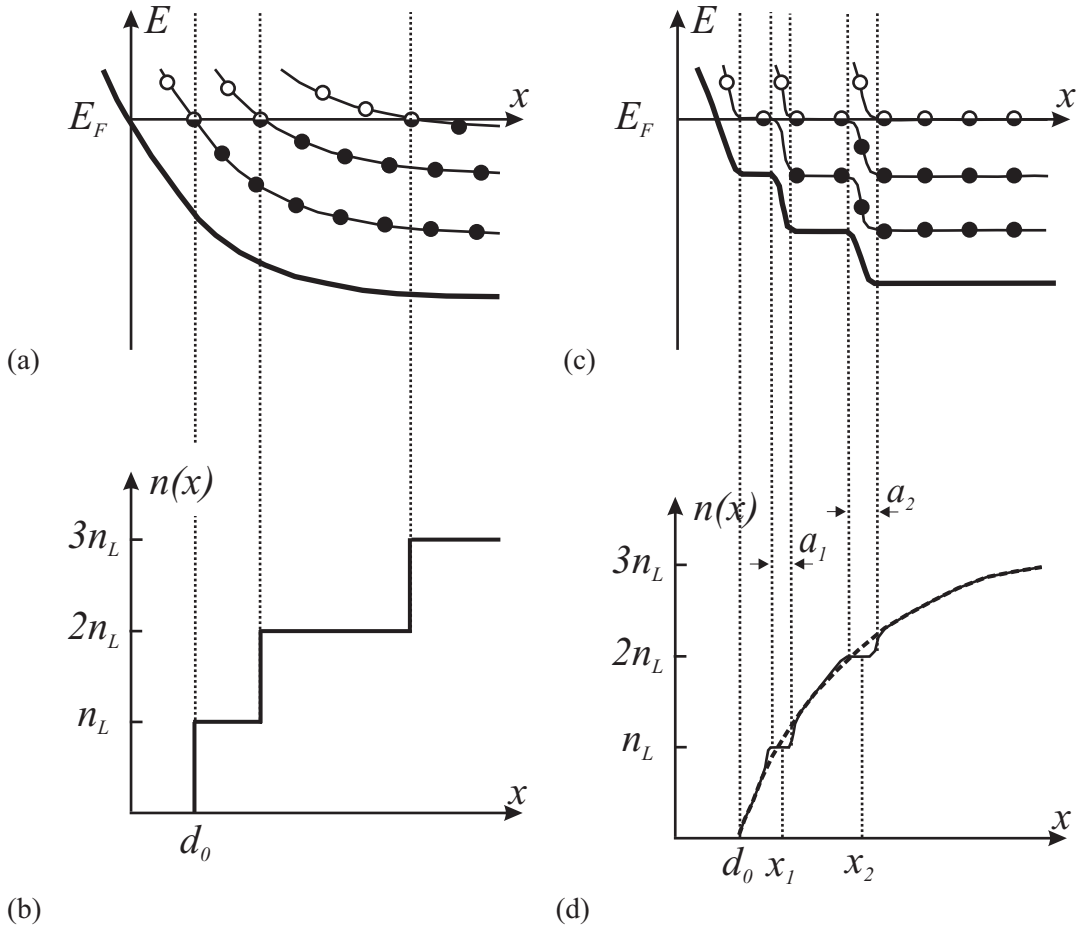

Figure 2.6: Structure of spinless edge states in the integer quantum Hall regime. (a) and (b) single electron picture. (a) Bending of the Landau levels by the confining potential, edge states are then formed at the intersection of the Landau levels with the Fermi energy . (b) Electron density as a function of distance to the boundary, the sudden changes in density would require high electric fields and are unphysical. (c) and (d) Self-consistent electrostatic picture. (c) 2DEG separates into regions of: (i) non-integer filling factor, where Landau levels are pinned at the Fermi energy. Here the 2DEG is compressible and screens the confining potential, and, (ii) regions of integer filling factor where a dipolar stripe has been formed. Here the 2DEG is incompressible and is unable to screen. (d) Density as a function of distance from the boundary. The dashed line shows the density distribution at zero field. At high field this is not significantly modified except in the regions where the next Landau level begins to fill. Based upon Ref. [27].

the energy gap means it is energetically favourable to relocate some electrons from the higher Landau level to the lower one. This relocation of charge forms dipolar stripes at the positions x_d where $n(x, B = 0)$ takes on integer multiples of n_L, the Landau level density [27]:

$$x_d = \frac{l_d}{1 + (\frac{k}{\nu})^2} \tag{2.22}$$

where ν is the bulk filling factor and $k = \text{int}(\nu)$ the number of completely filled Landau levels. The potential drop across the dipolar stripes equals the energy gap between the Landau levels $\hbar\omega_c$, the width of the stripes a_k can then be estimated from the zero field density gradient at the points x_d:

$$a_k = \frac{4x_d}{\nu}\sqrt{\frac{ka_b}{\pi l_d}} \tag{2.23}$$

where a_b is the effective Bohr radius.

The compressibility κ of an electron gas is defined as [29]:

$$\kappa^{-1} = n_s^2 \frac{\partial \mu}{\partial n} \tag{2.24}$$

Within the dipolar stripes it costs energy $\hbar\omega_c$ to add an electron, the compressibility is therefore zero and these regions are described as 'incompressible'. Away from the dipolar stripes electrons can be added at infinitesimally small energies and are described as compressible.

The effect of the magnetic field is to divide the 2DEG into alternating compressible and incompressible regions. In the compressible regions the 2DEG can screen strongly and the potential is constant. In the incompressible regions the 2DEG is unable to screen and it is in these regions that any potential drop occurs. Figure 2.7 shows the distribution of the compressible and incompressible stripes close to the edge as a function of the bulk filling factor.

2.7 Current distribution

The current distribution has been discussed continuously since the discovery of the QHE and is still controversial. In the previous sections the edge state model was introduced

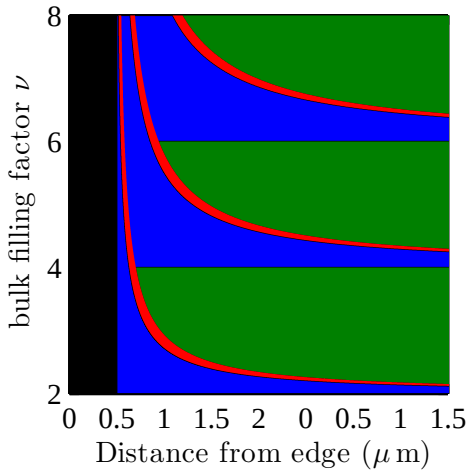

Figure 2.7: Distribution of compressible and incompressible regions close to the edge of a 2DEG as a function of filling factor neglecting spin splitting. The edge of the sample is on the left. Black indicates the depleted area at the edge l_d. Blue indicates compressible regions where the local filling factor is non-integer. Red indicates incompressible dipolar stripes where the local filling factor is an integer. Green indicates the compressible region which extends into the bulk of the sample

and the quantized Hall resistance interpreted as a result of one-dimensional transport in these edge states. The Hall resistance was calculated from the total current and the difference in chemical potential between the edge states. However, this does not mean that the electric current flows exclusively at the edge.

The theoretical discussion in the literature is divided into models which highlight the importance of current at the edges e.g. [24, 25] and models which suggest that the majority of the current is carried in the bulk of the sample e.g. [30–33]. In the edge current picture the current flows in the edge states and the Hall voltage is dropped entirely in these regions. In the bulk picture some proportion of the Hall voltage is dropped across the bulk of the sample and the current is carried by extended states near the centre of the Landau levels. The Hall current is proportional to changes in the local potential and does not depend upon the existence of edges. This bulk picture suggests that in a 2DEG without disorder the Hall voltage should drop gradually across the sample.

A number of experiments have been performed to try to determine the current distribution. The first experiments involved fabricating metal contacts on the top surface of Hall bar samples in an attempt to measure the potential distribution across the width of the device [34–36]. At non-integer filling factors these experiments showed the potential distribution varied linearly across the device. On the quantum Hall plateaus the potential distribution was very inhomogeneous suggesting a bunching up of the current. There are a number of problems with these experiments, however: The contacts may strongly influence the potential, it may be that it is the chemical potential rather than the electrostatic potential that is measured, and, finally, the Corbino effect will tend to isolate the contacts from the 2DEG on quantum Hall plateaus.

To avoid the problems associated with contacts a number of optical techniques were developed based upon the linear electro-optical effect. An applied electric field influences the birefringence of GaAs and the polarization direction of light passing through the crystal therefore changes depending upon the local potential. In a wide Hall bar (2 mm) Fontein *et al* [37] found that on the plateaus with small currents the

majority of the Hall voltage drops near the sample edges. This work was repeated by Knott *et al* [38] with a narrow Hall bar (200 μm) and conversely they found that most of the drop in the Hall voltage was in the middle of the channel. More recently Hall bars have been fabricated with a single electron transistor (SET) mounted on the top [39]. The edge of the 2DEG was then shifted towards the SET by electrostatic depletion with a gate electrode. This experiment was able to resolve the compressible and incompressible stripe pattern and was in qualitative agreement with theoretical predictions.

The experiments outlined so far don't give a conclusive answer to the nature of the current distribution in the quantum Hall effect because it is often difficult to compare the experiments as the experimental conditions vary significantly (sample size, current, resolution). The most recent experiments have been carried out with scanning probe techniques and will be discussed in detail in Chapter 3.

2.8 Summary

This chapter has given a brief overview of the quantum Hall effect a more detailed discussion can be found in a number of books [18, 40, 41].

The next chapter gives an overview of scanning probe microscopy.

Chapter 3

Scanning Probe Microscopy

A scanning probe microscope builds up a spatial image from local measurements made with a sharp probe rastered over a surface. The advent of these techniques has made it possible to make measurements and carry out manipulation on length scales of a nanometre or less.

3.1 Scanning Tunnelling Microscope

The first example of an SPM was the scanning tunnelling microscope (STM) invented in 1981 by Binnig, Gerber and Weibel [7]. In an STM a sharp tip is brought close to a conductive surface with a bias voltage applied between the tip and the surface. When the separation is small enough, typically a few Å, electrons can tunnel between the tip and sample surface resulting in a current. This tunnel current is used as the control signal in a z-feedback loop. A topographic image of a surface can be built up from scanning the tip over the surface and recording the z-position required to keep the tunnel current constant. The tunnel current has an exponential dependence on the separation so that most of the current is carried via the atom on the tip closest to the sample. This feature of the tunnel current is the factor which makes atomic resolution so readily achievable with the STM. Images of the 7×7 reconstruction of silicon were published less than a year after the first STM paper [8]. In 1986 Binnig and Rohrer

were awarded the Nobel prize in physics for their invention.

3.2 Atomic Force Microscope

An atomic force microscope (AFM) probes the cumulative forces that act between the atoms in the tip and sample. These forces act among insulators as well as conductors which gives the technique greater scope than the STM. In an AFM, the tunnelling tip is replaced with a force sensing cantilever.

3.2.1 Tip-sample Forces

In vacuum, the tip-sample force F_{ts} is a mixture of short range chemical bonding forces and long range, van der Waals, electrostatic, and magnetic dipole forces. In air or liquid operation this is further complicated by meniscus or hydrodynamic contributions.

Van der Waals forces

The van der Waals forces originate from fluctuations in the electric dipole moment of atoms and their mutual polarization. For two atoms separated by a distance z the induced dipole-dipole energy varies as $1/z^6$ [42]. The van der Waals energies for macroscopic bodies, such as the macroscopic part of an AFM tip, can be calculated using the Hamaker approach which assumes the individual atom-atom interactions are additive. The resulting forces for various simple tip geometries are given in Ref. [43].

Short range chemical forces

Chemical bonds are treated in a number of quantum mechanics textbooks and simple cases such as the H-H covalent bond can be solved analytically. Some simple models such as the Morse potential or Lennard-Jones potential are commonly used to describe a chemical bond. The Lenard-Jones potential V_{LJ} is given by:

$$V_{LJ} = -\frac{E_0}{\sigma}\left(\left(\frac{\sigma}{z}\right)^{12} - 2\left(\frac{\sigma}{z}\right)^{6}\right) \tag{3.1}$$

where E_b is the bond energy and σ is the equilibrium length. This potential has an attractive term $\propto z^{-6}$ originating from the van der Waals interaction and a repulsive term $\propto z^{-12}$ from Pauli repulsion. The form of the repulsive part is chosen for ease of calculation, in reality it is closer to an exponential dependence. Van der Waals and electrostatic forces are treated in Ref. [44].

Total Force

Excluding magnetic forces (non-magnetic tip), electrostatic forces (tip-sample potential $V_{ts} = 0$), meniscus and hydrodynamic forces (in vacuum) then the tip-sample force F_{ts} can be represented by:

$$F_{ts} = \frac{12E_0}{\sigma}\left(\left(\frac{\sigma}{z}\right)^{13} - \left(\frac{\sigma}{z}\right)^{7}\right) - \frac{A_H R}{6z^2} \tag{3.2}$$

The first part originates from a Lenard-Jones potential representing the interaction between the most prominent atom and the surface [45]. The second term is the van der Waals contribution from the macroscopic part of the tip. This is for a simple spherical tip radius R where A_H is the Hamaker constant and depends on the tip and sample materials. Figure 3.1 shows a plot of Eqn. 3.2 as a function of tip-sample separation for some typical parameters. An important observation is that the tip-sample force is not monotonic over the whole distance range; this makes establishing stable distance feedback much more difficult than for an STM.

3.2.2 Force sensors

A key component of the AFM is the transducer used to convert the tip-sample forces into a measurable quantity. In most AFM experiments the normal component of the tip-sample force is used to image the surface, a cantilever beam geometry is soft in one direction and rigid in the remaining two and is the basis of most force sensors. Cantilevers can be used in a static mode, where the deflection is measured and is directly related to a force. Cantilevers can also be used in a dynamic mode where they are vibrated and the damping and force gradient modify the amplitude and frequency

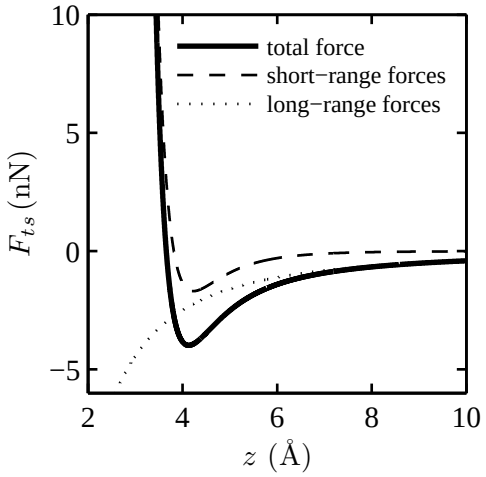

Figure 3.1: Theoretical tip-sample force F_{ts} as a function of tip-sample separation z using a Lennard-Jones short range force and a $1/z^2$ long ranged force as in Eqn. 3.2 with parameters, $E_0 = 3\,\text{eV}$, $\sigma = 3.4\,\text{Å}$, $A_H = 0.2\,\text{aJ}$ and $R = 120\,\text{Å}$.

of the oscillation. These modes of operation are discussed in detail in Sections 3.2.3 and 3.2.4.

The first cantilevers were hand-made, consisting of a strip of gold foil, 0.8 mm long, glued to a diamond tip [46]. Soon after, cantilevers with integrated tips were fabricated from doped silicon or silicon nitride using micromachining technology [47]. These are examples of passive force sensors which require some external method of excitation and detection.

The first detection schemes used an STM tip placed close to the back of the cantilever to measure the cantilever deflection [46]. This type of detection system only works over a fraction of a nanometre, ideally requires UHV conditions and exerts its own force on the cantilever. Optical detection systems followed [48]; these use either a beam deflection or interferometric technique. Optical techniques are used by the vast majority of room temperature AFMs and are discussed in detail by Sarid [49]. In low temperature experiments alignment of the optics in a cryostat is difficult and in semiconductor studies stray laser light can give rise to a persistent photoconductivity effect. Force sensors which exploit piezoelectric or piezoresistive phenomena have been

developed to avoid the problems associated with optical detection systems. Piezoresistive cantilevers are micromachined from silicon and have half of their thickness doped. Any deflection strains the conductive layer and causes a change in its electrical resistance [50]. Piezoelectric cantilevers convert mechnical stress into electric charge and vice-versa. It is difficult to measure the amount of charge created by a static deflection so these are impractical for measuring constant forces. By applying an AC voltage and measuring the current it is possible to excite and detect the motion with no additional components. Another advantage of piezoelectric sensors is that that they have a power dissipation of the order of nW compared to mW for piezoresistive sensors and this is the reason they are used extensively at low temperature. Initially, piezoelectric cantilevers with integrated tips were fabricated [51] but more recently sensors have been based on quartz tuning forks. Quartz tuning forks are the time-keeping element of digital watches. By removing the tuning fork from its can and attaching a sharp tip it can be used as a sensor. Quartz tuning forks are very cheap (less than 20 pence), very stable with age and temperature, and their size makes it possible to attach a variety of different probes. The first application was in scanning acoustic microscopy [52]. Recent applications have included imaging subatomic features on silicon [53]. Quartz tuning forks and the details of our sensor design are discussed in detail in Chapter 4.

3.2.3 Static atomic force microscopy

In static AFM mode the tip is held in contact with the surface and the tip-sample force F_{ts} translates into a deflection q' of the cantilever.

$$q' = \frac{F_{ts}}{k} \tag{3.3}$$

where k is the spring constant. If the spring constant is known then it is simple to calculate the tip-sample force.

A topographic image of a surface can be built up from scanning the tip and recording the z-position required to keep the deflection constant. The force sensitivity depends upon the performance of the deflection detector and the spring constant of the can-

tilever. To avoid deforming the sample the spring constant of the cantilever should be much softer than the bonds between the tip and sample.

Contact AFM is simple to implement and interpret. However, the large lateral forces mean that the tip is subject to wear and soft samples can easily be damaged. The force is determined from the static deflection of the cantilever making this measurement subject to $1/f$ noise.

The smaller the spring constant of the cantilever the greater the deflection for a given force and the greater the sensitivity. However, if the cantilever stiffness is below a certain value then approaching the tip can cause a sudden 'snap-to-contact'. This instability does not occur if the spring constant of the cantilever k is greater than the maximum force gradient of the tip-sample interaction k_{ts}^{max}:

$$k > \max\left(\frac{\delta^2 V_{ts}}{\delta z^2}\right) = k_{ts}^{max} \tag{3.4}$$

where V_{ts} is the tip-sample potential.

Despite these problems it has been possible to demonstrate atomic resolution in a few very specific environments, for example at low temperature in UHV [54].

3.2.4 Dynamic atomic force microscopy

In dynamic measurements the cantilever is vibrated and changes in the oscillation parameters are used as a feedback signal. The advantage of this technique is that noise can be reduced by using lock-in detection and operating at a frequency where $1/f$ noise is no longer significant.

The tip-sample interaction can be separated into conservative and non-conservative forces. Conservative forces are a unique function of the tip-sample separation. Consequently, over a complete oscillation cycle the net work due to these conservative forces is zero. Non-conservative forces depend upon whether the tip is approaching or retracting from the surface and represent hysteresis in the interaction. The net work performed against non-conservative forces over an oscillation cycle is non-zero and causes dissipation of energy from the cantilever. These contributions affect the properties of the

cantilever in different ways, the conservative forces shift the resonant frequency of the cantilever whilst the non-conservative forces reduce the quality factor.

There are two commonly used detection schemes, amplitude-modulation (AM) and frequency-modulation (FM).

AM detection

In AM measurements the cantilever is driven by an AC signal with a fixed frequency and amplitude close to the resonance frequency of the cantilever. The amplitude of the cantilever deflection is then used as the feedback signal [48]. The tip-sample interaction changes the resonance frequency and/or the quality factor of the cantilever and this is reflected in the oscillation amplitude. This detection system is easy to implement but it is difficult to interpret and the response is slow.

It is not possible to separate the conservative and non-conservative contributions of the tip-sample interaction as at a fixed measurement frequency both change the oscillation amplitude.

The response of the amplitude is not instantaneous and has a characteristic time scale $\tau_{AM} \approx 2Q/f_o$ where f_0 is the resonant frequency [55]. In UHV it is possible to achieve quality factors of > 50000 giving a bandwidth $< 1\,\mathrm{Hz}$ which is far too slow.

FM detection

In the FM measurements the frequency of the drive signal is adjusted so that the cantilever is always driven on resonance. This can be achieved by making the cantilever the frequency determining part of an oscillator [56] or by using phase-locked loop techniques. The change in resonant frequency is then used as the feedback signal. The oscillation amplitude can be measured separately and an additional feedback loop can be used to keep the amplitude constant. This technique enables the conservative and non-conservative parts to be separated, making interpretation simpler. The change in frequency occurs within one oscillation cycle on a timescale of $\tau_{FM} = 1/f_0$ which means the quality factor can be increased without restricting the bandwidth [55].

Oscillation amplitude

For very small amplitudes the frequency shift is a very simple function of the tip-sample force gradient, it is proportional to the tip-sample gradient. For large amplitudes it is much more complicated as the direction and size of the force gradient will vary over one cycle. It has been shown that for small amplitudes the frequency shift is very sensitive to short ranged forces as these have a strong force gradient, while for large amplitudes long range forces contribute heavily [57].

The frequency noise of the measurement is inversely proportional to the oscillation amplitude a. The slope of the frequency shift curve is constant at first and drops as $a^{-1.5}$. As a result it has been shown that there is minimal noise for oscillation amplitudes on the length scale of the tip-sample force F_{ts}.

If hysteresis occurs in the tip-sample interaction then energy ΔE_{ts} must be supplied to the cantilever during each oscillation cycle. If the energy loss is large compared to the total energy of the cantilever then controlling the amplitude can become difficult. An approximate criterion for stability is the following [45]:

$$\frac{k}{2} \geq \Delta E_{ts} \frac{Q}{2\pi} \tag{3.5}$$

In order to measure short range interactions with high resolution and to minimise noise then small oscillation amplitudes are required. To maintain stability with small amplitudes then the spring constant needs to be high. Quartz tuning forks have a spring constant two orders of magnitude higher than silicon cantilevers and have made it possible to image with sub-nanometre oscillation amplitudes and demonstrate subatomic resolution [53].

3.3 Electric measurements

Electric measurements have been made indirectly by measuring the additional force acting on a biased AFM probe, for example in Kelvin probe force microscopy (KPFM), or directly with novel sensors such as scanning-single electron transistor microscopy (SSET).

A SET is a sub-micrometre tunnelling device where the current passing between source and drain electrodes is governed by the Coulomb blockade effect of a small metal island. The conductance of the SET is extremely sensitive to the electric potential experienced by the island. A scanning SET was first demonstrated by M.J.Yoo *et al* by fabricating an SET on to the end of a sharp glass fibre [58]. These scanning experiments are very demanding because of the low temperatures required for the SET to operate and the difficulties involved in fabricating the sensor on an AFM probe. A review of the experiments can be found in Chapter 7.

Kelvin force microscopy, first demonstrated by Nonnenmacher *et al.* [59], is a non-contact AFM technique which allows investigation of the contact potential difference between the AFM tip and the sample. A DC bias V_{DC} in combination with an AC modulation V_{AC} at a frequency ω_k is applied between the conductive AFM tip and the sample [59]. The sample potential is the sum of the contact potential difference V_{cpd} (due to the difference in work function of the tip and sample) and the two externally applied potentials. The electrostatic force F_e is given by [49]:

$$F_e = \frac{1}{2}\frac{\delta C}{\delta z}\left(V_{cpd} + V_{DC} + V_{AC}\cos\omega_k t\right)^2 \tag{3.6}$$

$$= \frac{1}{2}\frac{\delta C}{\delta z}\left[\left(V_{cpd} + V_{DC}\right)^2 + 2\left(V_{cpd} + V_{DC}\right)V_{AC}\cos\omega_k t + V_{AC}^2\cos^2\omega_k t\right] \tag{3.7}$$

where C is the tip-sample capacitance and z is the tip-sample separation. The response includes three frequency components, the first term is at DC the second at ω_k and the third at $2\omega_k$. The frequency shift of the cantilever will have two components:

$$\Delta f_{\omega_k} \propto \frac{\delta C}{\delta z}(V_{DC} - V_{cpd})V_{AC}\cos(\omega_k t) \tag{3.8}$$

$$\Delta f_{2\omega_k} \propto \frac{1}{2}\frac{\delta C}{\delta z}V_{AC}^2\cos(2\omega_k t) \tag{3.9}$$

Typically a feedback circuit is used to adjust V_{DC} during scanning to maintain $\Delta f_{\omega_k} = 0$. Images of V_{DC} then represent the local contact potential difference [60]. It is also possible to measure $\Delta f_{2\omega_k}$ simultaneously and construct an image of the local gradient of the capacitance [61].

Kelvin probe measurements have been made on a variety of systems. Two examples

are studies of surface defects [62] on semiconductors and the characterization of pn junctions [63].

A review of the Kelvin probe experiments performed in the quantum Hall regime is given in Chapter 7.

3.4 Scanning capacitance microscopy

Scanning capacitance microscopy is a technique where the capacitance between a sharp tip and a sample is measured as a function of position. It is an important method for the characterization of dopant profiles in semiconductor samples.

The first SCM was demonstrated by Matey and Blanc [64]. An insulating stylus was scanned in the tracks of a pre-grooved disk whilst the capacitance between an electrode and the surface was measured. Bugg and King were the first to demonstrate an SCM with an unguided scanning system and used it to make topographic images of samples with a resolution of 200 μm [65]. The tip-sample separation was modulated and the capacitance variation at this oscillation frequency was measured. This capacitance variation was used by a height feedback loop to keep the average tip-sample separation constant. The disadvantage with this technique is that capacitance depends upon the sample geometry and material properties and changes in these will introduce artefacts to measured topography.

Later Williams *et al* modified an STM to incorporate a capacitance measurement, the surface was scanned with feedback at a constant tip-sample capacitance. Barret and Quate were the first to combine a capacitance measurement with a contact AFM allowing simultaneous topographic and capacitance data to be recorded [66].

Applications of SCM include measurement of dopant profiles in semiconductors [67] and pn junctions [68]. Another application is charge storage on nitride-oxide-silicon (NOS) systems where information densities of 27 Gbits/in^2 have been demonstrated [66]. Carrier relaxation times have been measured by Hamers *et al* using SCM combined with irradiation of ultra-fast laser pulses [69].

3.4.1 Capacitance sensors

Most capacitance sensors use the RCA video disc capacitance pickup design [70]. The circuit consists of an LC-stripline resonator with a frequency $\approx 1\,\mathrm{GHz}$, ultra-high frequency oscillator and peak detector. Driven near resonance, changes in capacitance modulate the amplitude and this modulation is recovered by the peak detector. With an optimized version of this design capacitance variations as small as $10^{-21}\,\mathrm{F}$ can be detected in a 1 Hz bandwidth. A lumped-element version was developed by Bugg and King operating at 90 MHz [65]. Other designs which measure capacitance directly using bridge techniques have been demonstrated but in general are slow and suffer with problems from changes in the stray capacitance [71]. The low temperature SCM we have developed uses a similar detection system to Bugg and King and is discussed in detail in Chapter 5.

3.4.2 Probe design

The type of probe used in SCM can make a large difference to the performance of the microscope. The first probes were made from tungsten wire, sharpened to a diameter of a few tens of nanometres by electrochemical etching. These tips had the advantage of good wear properties and small stray capacitance, however it is difficult to batch fabricate them and the oxide layer is unpredictable. Micromachined silicon tip-cantilever assemblies with an evaporated metal film are currently in regular use. These types of probes are well characterized and easy to use. The disadvantages are that the metal film wears quickly, the tip radius is relatively large (typically 35 nm) and stray capacitance from the cantilever arm can reduce sensitivity. An alternative to the metal coating is to dope the tip. These tips are more resistant to wear but can deplete under bias. A review of probes for electrical measurements can be found in Ref. [72].

3.4.3 Contact SCM

The contact AFM/SCM is the most widely used variant of capacitance microscopy and is implemented on commercial microscopes such as the Veeco D3100.

In contact SCM a conductive AFM probe is brought into contact with a semiconductor sample covered with a thin dielectric layer. The tip-sample contact forms a metal-insulator-semiconductor (MIS) capacitor. The capacitance is a function of the local carrier concentration and the bias voltage [73]. AFM measurements are used to maintain a constant contact force with the surface. At the same time measurements of the tip-sample capacitance are made with a high frequency resonant circuit. In this way an image of the sample's topography and capacitance variation are obtained simultaneously, enabling correlation of sample location with electrical properties. An important application of this technique is profiling dopants in semiconductor samples. An extensive review of the technique is given by Williams [67].

The tip-sample capacitance is typically a few tens of aF for a tip radius of 50-150 nm [74]. Stray capacitances are of the order of 0.5 pF [74, 75]. To reduce the influence of stray capacitance it is usual to measure a modulated component of the tip-sample capacitance. The most common approach is to apply a small AC bias between the tip and the sample and to measure the derivative dC/dV with lock-in detection. The sign of the derivative gives the type of carrier and the amplitude can be related to the carrier concentration. No signal is measured over dielectric or metallic regions since these cannot be depleted.

Figure 3.2(a) is a schematic of a contact SCM measurement. The conductive probe is connected to the capacitance detector and the tip-sample bias voltage is applied to a backgate on the sample. Figure 3.2(b) shows capacitance-voltage (C-V) curves measured at high frequency for two n-type semiconductor samples with different densities. The measured tip-sample capacitance consists of the capacitance of the oxide layer C_o in series with the capacitance of the depletion layer C_D. The variation in the capacitance as a function of bias voltage is due to the varying size of the depletion region. With a positive bias voltage electrons are accumulated under the tip, the tip-sample capacitance saturates at a maximum given by the capacitance of the oxide layer. With negative bias voltages the region under the tip is depleted and the capacitance is reduced until there is no free carrier density. Waveforms between the dashed lines

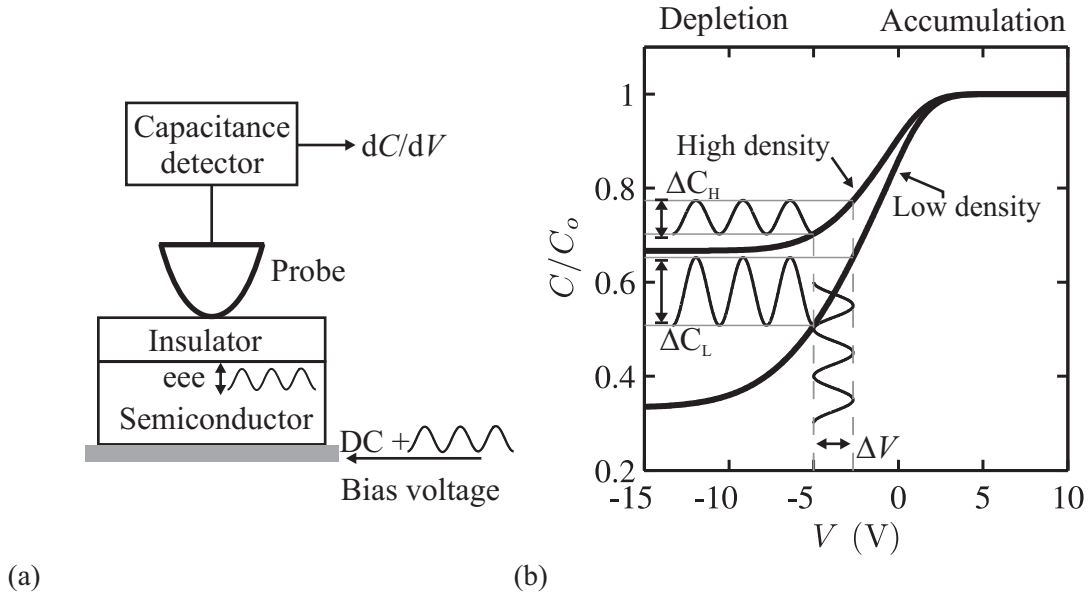

(a) (b)

Figure 3.2: (a) Schematic of contact mode SCM. A conductive probe is held in contact with a semiconductor sample with a thin insulating layer on the surface. A DC bias voltage with a small AC modulation is applied to the sample. The capacitance detector measures the capacitance change in response to the AC modulation. (b) C-V curves for n-type semiconductor samples with different densities. Waveforms between the dashed lines show an AC modulation ΔV and the resulting capacitance for the high and low density samples ΔC_H and ΔC_L respectively.

show an AC modulation ΔV and the resulting capacitance change for the high and low density samples ΔC_H and ΔC_L respectively. In this simple illustration the sample with the lower carrier concentration gives a bigger response. In real experiments the SCM output is not always a monotonically increasing signal with decreasing dopant density [76]. There is a relative shift between the dC/dV curves for different doping levels which can cause a contrast reversal.

An alternative technique, scanning capacitance spectroscopy (SCS), has been demonstrated by Edwards *et al* [77]. In SCS C-V curves are measured at every position in the scan area. The shape of the curve can then be used to distinguish between different types of doping and carrier concentration.

The SCM response also depends upon the experimental parameters, such as, the DC bias, the properties of the oxide layer, and the sample geometry. Preparation of the surface including formation of a good dielectric oxide, is critical to the reproducibility of SCM measurements and is a major challenge [78].

At the moment contact SCM is widely used in qualitative analysis of samples and is limited by the lack of a general quantification method.

3.4.4 Non-contact SCM

Non-contact SCM has been proposed as an alternative mode of operation [74], as it avoids tip wear and changes in the contact area between tip and the surface. The oscillation of the probe modulates the tip-sample capacitance, the size of this modulation depends upon the oscillation amplitude and the local part of the tip-sample capacitance.

Contact mode SCM uses an AC bias to modulate the tip-sample capacitance, and therefore as a prerequisite samples must exhibit a voltage dependent capacitance. Non-contact mode SCM does not have this restriction and studies have been carried out on dielectric films on metallic substrates [74], buried metal wires [79] and conductive samples (see Chapter 6). The lateral resolutions reported are comparable to contact SCM.

Most AFM systems use an optical detection system to measure the deflection of the cantilever. However, leakage of laser light can cause undesirable photoconductivity effects [80]. In a recent development, contemporary with this project, SCM has been implemented in non-contact mode with a piezoelectric quartz tuning fork force sensor [81].

3.5 Summary

This chapter has given a very brief overview of scanning probe techniques, more detailed accounts can be found in a number of books and review articles [45, 49, 82]. In the next chapter the development of a low-temperature AFM/SCM is discussed. Chapter 5 then discusses the details of the capacitance detection system.

Chapter 4

Experimental Set-up

4.1 Overview

A combined AFM/SCM has been developed that operates at low temperature and high magnetic field. The system is based on a commercial ^{4}He cryostat with a variable-temperature insert (VTI) and superconducting magnet. The microscope is mounted on a probe which is loaded into the VTI. AFM, SCM and transport measurements can be performed simultaneously. AFM is carried out in dynamic mode with a quartz tuning fork (TF) force sensor. Capacitance measurements are made with an RF technique which has a resolution of 0.1 aF and bandwidth of 200 Hz as discussed in Chapter 5. Transport measurements are made using direct connections to the sample. A schematic showing the main parts of the system is shown in Fig. 4.1. The following sections of this chapter discuss the set-up in detail before outlining an analysis of the tip-sample interactions.

4.2 Cryostat and vibration isolation

A commercial ^{4}He cryostat with a VTI is used to cool the experiment, and a superconducting magnet is used to apply a magnetic field. The VTI has a 50 mm diameter sample space that is isolated from the main bath by an inner vacuum can (IVC). The

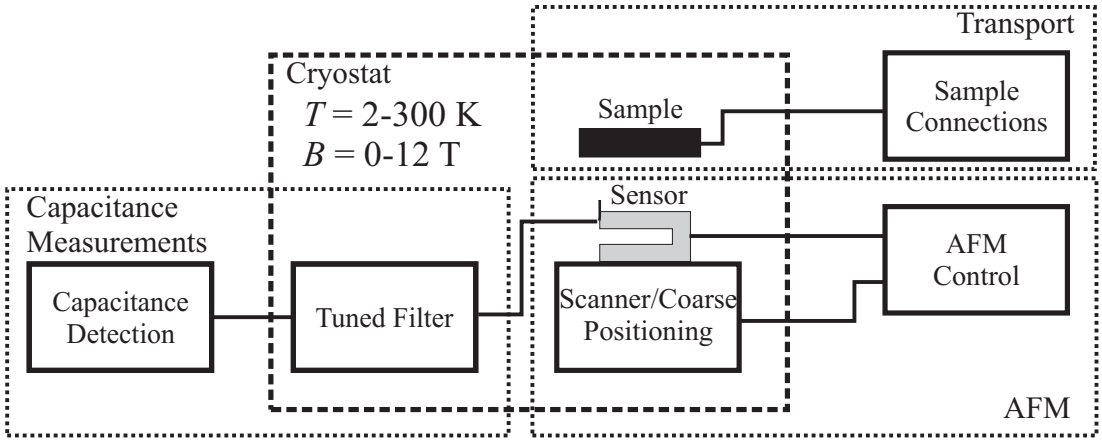

Figure 4.1: Schematic showing the main parts of the system.

magnet and VTI are positioned in the main bath of the cryostat with the bottom of the VTI centred in the bore of the magnet.

A capillary with a needle valve connects the main bath to the sample space and allows a flow of liquid to be admitted to the sample space. The temperature is controlled by adjusting the He flow and applying heat. On entering the sample space the liquid evaporates and is warmed to the required temperature by a heater, which is controlled by a temperature controller. A reduction gearbox was fitted to the needle valve control to make fine adjustment of the He flow possible. This method has a base temperature of 1.5 K and a hold time of up to a week. An alternative is a single-shot technique, in this case the sample space is flooded so that the sensor and sample are in liquid He-II, cooling below 4.2 K is achieved by reducing the vapour pressure by pumping [83]. The base temperature of this method is 1.4 K and has a hold time of eight hours. Most experiments are carried out in the gas flow mode because of the long hold time.

The tip-sample separations required for AFM are of the order of nanometres and, as such, a prerequisite for high resolution imaging is isolation of the microscope from mechanical vibration. The cryostat was supported on air legs to decouple it from ground based vibration. Acoustic coupling was reduced by passing the pumping lines through sand boxes and building a sound proof box around the top plate. Vibrations originate inside the cryostat from the boiling of He in the main bath. To minimize

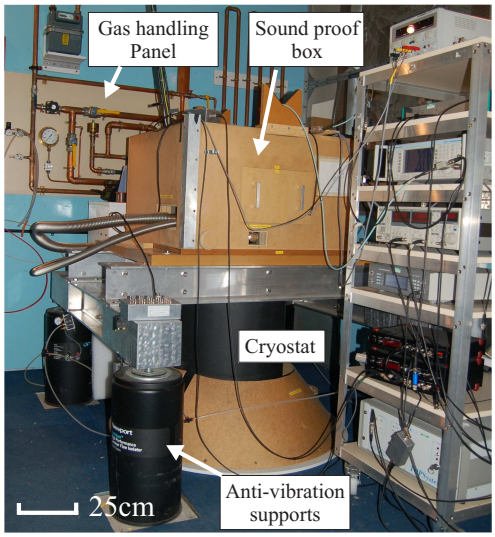

Figure 4.2: Photograph of the laboratory showing the cryostat mount.

coupling to the microscope great care was taken to avoid the probe touching the walls of the sample space. A photograph of the laboratory is shown in Fig. 4.2.

4.3 Scanning and coarse positioning

The tip and sample are positioned with a piezoelectric scanner and a set of piezoelectric slip-stick motors.

In a piezoelectric material an applied electric field will cause a change in the shape or size of the material. The piezoelectric effect is very small, large applied voltages cause very small changes in the dimensions, for this reason they are used extensively in SPM applications. As an example the calibration of the scanner in the z-direction is approximately 10 nm/V at room temperature.

Figure 4.3 shows a series of photographs of the microscope head.

4.3.1 Scanner

Scanning is performed by a five-electrode piezoelectric-tube (length 50.8 mm, outer diameter 12.7 mm, wall thickness 0.5 mm, material lead zirconate titanate (PZT) ceramic,

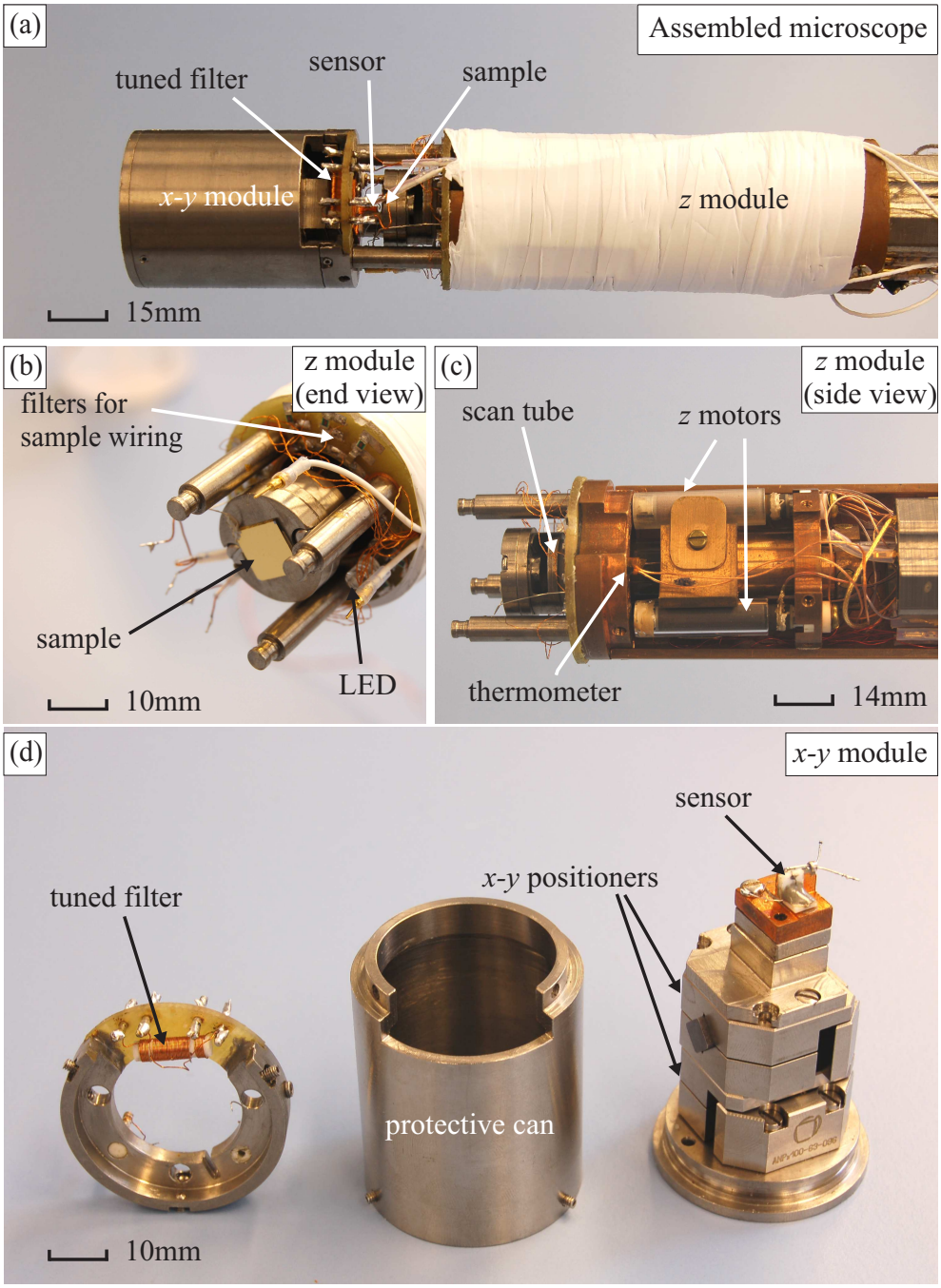

Figure 4.3: (a) The assembled microscope consisting of the z and x-y modules. (b) The end of the z module showing the sample mounted on the scan tube and the filtered sample wiring. (c) Internal view of the z module showing the scan tube mounted on piezoelectric slip-stick motors. (d) x-y module used for lateral positioning of the sensor.

EBL#2[1]). The tube has a single inner electrode and a quadranted outer electrode; this allows motion in all three directions. The maximum x-y scan range is 46 μm at 300 K, 15 μm at 80 K and 8.4 μm at 2 K. The range in the z-direction is 4.5 μm at 300 K, 1.5 μm at 80 K and 0.8 μm at 2 K. When operating in a low pressure of He gas the scan range is kept below 70 % of the maximum to avoid arcing between the outer electrodes.

The scan tube is fixed at the top to a carriage, which is part of the z-positioner, and is shown in Fig. 4.3(c). A platform for mounting the sample is glued into the bottom end of the scan tube.

4.3.2 Coarse positioning

The range of the scan tube limited to a few μm in each direction, and so in order to bring the tip within the range of the scan tube coarse positioning systems are required. The positioners used by this microscope are described in the following sections.

z-positioner

The z-positioner is a piezoelectric slip-stick design which is used to transport the scan tube and sample mount in the z-direction. This positioner is used during the approach of the surface before imaging. The scan tube is mounted in a copper carriage which is supported on three piezoelectric motors using CuBe leaf springs, see Fig. 4.3(c). The motors consist of a piezoelectric actuator and a quartz sliding surface. A sawtooth waveform is applied to the piezoelectric motors to move the carriage with a 'slip-stick' action. In order for the scanner carriage to follow the motion of the motors then the frictional forces between the springs and the motors must equal the rate of change of momentum of the carriage. During the ramp phase of the waveform the springs stick to the motor surface and the carriage is moved forwards. When the voltage is suddenly reduced the frictional forces are not adequate and the springs slip against the motors. The motors return to their rest position whilst the carriage remains advanced. An arbitrary distance can be moved by repeating this cycle a number of times. The step

[1]EBL Products Inc.

Temperature (K)	Drive voltage (V)	Step size (nm)
300	30	500
80	80	400
2	150	100

Table 4.1: Typical parameters for the z-positioner.

size depends on the amplitude of the waveform and the dimensions and piezoelectric constant of the drive tubes. Table 4.1 gives some typical values for the drive voltage and associated step size at different temperatures.

x-y positioner

The x-y positioner changes the relative lateral position of the tip and sample in order to locate an area of interest, for example the edge of a Hall bar.

Two schemes have been used for x-y positioning. In the first implementation the sensor platform was fixed and the sample was mounted on a puck on the end of the scan tube. The sample puck could be moved with a slip-stick action by exciting the scan tube.

More recently an x-y module has been developed based on commercial positioners. The sample mount is now fixed and the sensor platform is moved by two linear positioners[2] mounted orthogonally. Figure 4.3(d) shows an exploded view of the x-y module. Tests were performed with a new 'robust and ultra-stable' design of positioner[3], however this was very sensitive to acoustic excitation and not fit for purpose.

The x-y motion is reliable, reproducible to within 5 % and gives step sizes of between 5 nm and 1 μm at low temperature. Table 4.2 gives some typical values for the drive voltage and associated step size at different temperatures.

[2] ANP100 series attocube systems

[3] ANP100Flex series attocube systems

Temperature (K)	Drive voltage (V)	Step size (nm)
300	15	1000
80	40	800
2	60	500

Table 4.2: Typical parameters for the x-y positioner.

4.4 AFM/SCM sensor

The home-made sensors use a piezoelectric quartz tuning fork (TF) as the oscillating element and an etched tungsten wire as the tip.

4.4.1 Quartz tuning forks

A number of properties of TFs make them widely used as force sensors in low temperature SPM. They have a very low power consumption ($< 1\,\mathrm{nW}$). There is no optical detection system which avoids the persistent photoeffect in semiconductor studies. Their relatively large size makes it easy to fabricate more complicated probes for different applications. A review of experiments performed with TF sensors is given in Ref. [45].

The TF contacts are patterned to excite the antisymmetric eigenmode of oscillation, this gives very high quality factors as the dynamic forces to keep the tines oscillating cancel each other out. Attaching a mass such as a tip to one tine breaks the symmetry of the system and might lead to excitation of the symmetric mode. This problem can be avoided by immobilizing one tine, reducing the TF to a simple cantilever beam, which can be approximated as a single harmonic oscillator [84].

Harmonic Oscillator Model

The cantilever can be described as a weakly disturbed harmonic oscillator, effective mass m_c^* and spring constant k_0 [45]. Figure 4.4 illustrates the deflection of the tip $q'(t)$. It oscillates with an amplitude a at a tip-sample distance $q(t) = q'(t) + z + a$ from the sample where $q = z$ is the closest point to the sample. The equation of motion is:

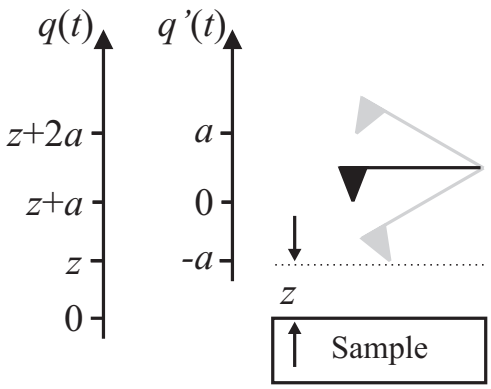

Figure 4.4: Schematic showing the coordinate system used to describe the tip motion. The minimum tip-sample separation is z and the oscillation amplitude is a.

$$m_c^* \ddot{q}(t) + \gamma \dot{q}(t) + k_0 q(t) = F_{ts} + F_0 \tag{4.1}$$

where γ is the damping coefficient, F_{ts} is the tip-sample force and F_0 is the drive force. This can be solved for the unperturbed motion, $q'(t) = a\cos(2\pi f_0 t)$, with $f_0 = \frac{1}{2\pi}\sqrt{\frac{k_0}{m_c^*}}$. If the tip-sample force gradient is constant then it can be described by an effective spring constant $k_{ts} = \frac{\partial F_{ts}}{\partial z}$ and the frequency shift is given by [45]:

$$\Delta f = f_0 \frac{k_{ts}}{2k_0} \tag{4.2}$$

The length scale of the tip-sample interaction is typically less than one nanometre whilst the oscillation amplitude is tens of nanometres. The tip-sample force will vary by orders of magnitude over one cycle and for this reason this simple analysis is not adequate.

The frequency shift for an arbitrary force F_{ts} can be derived by assuming the cantilever motion is periodic and expressing it as a Fourier series [45]. Equation 4.1 can then be solved to give the magnitude of the harmonics. To first order the frequency shift is then given by [45]:

$$\Delta f \approx -\frac{f_0}{k_0 a^2} \langle F_{ts} z \rangle \tag{4.3}$$

where $\langle ... \rangle$ denotes the average over one cycle. This approximation only includes the first harmonic which is a good assumption for $\langle F_{ts} z \rangle \ll k_0 a^2/2$ which is correct for stiff

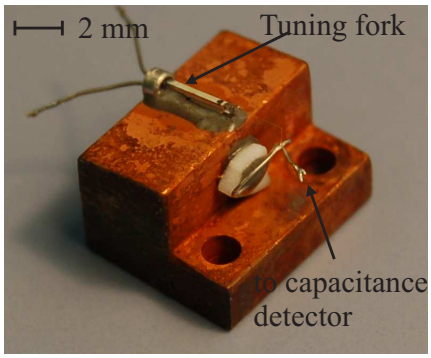

(a)

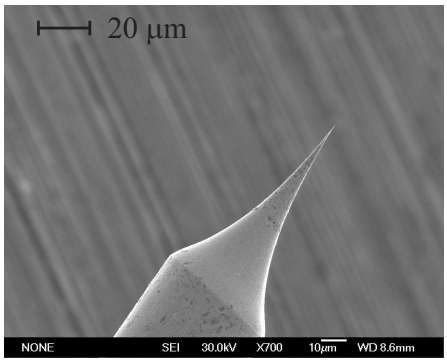

(c)

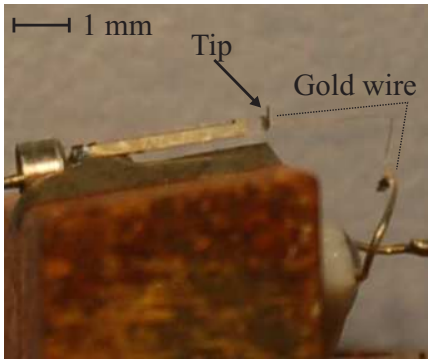

(b)

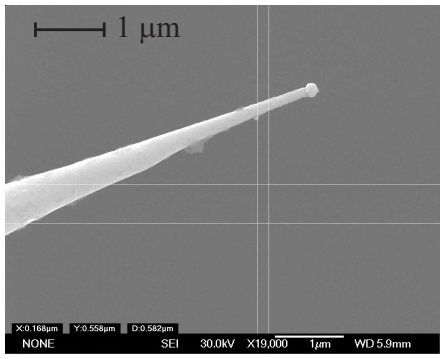

(d)

Figure 4.5: (a)-(b) Photographs showing home-made TF SCM sensor. (c)-(d) SEM images of etched tungsten tip.

cantilevers or small amplitudes. It is not simple to extract a force-distance curve from frequency-distance information as at each point the frequency shift is an average over a whole cycle. This problem will be considered in detail in Chapter 6.

4.4.2 Sensor construction

Figure 4.5 shows the sensor and an SEM image of the tip.

A photograph of the sensor design is shown in Fig. 4.5(a)-(b). The outer case of the tuning fork[4] was removed using a lathe to leave the metal ring surrounding the leads at the base of the fork. The fork was glued to a copper base with non-conductive

[4]Fox electronics watch crystal NC26 - RS part number 472-1161

epoxy[5], care was taken not to restrict the movement of the free tine with any glue. A piece of 50 μm tungsten wire[6] was bent into a right angle and trimmed to leave one end approximately 5 mm and the other approximately 0.5 mm long. The longer half would be etched to become the tip whilst the short length would allow connection of a fine gold wire. The tungsten wire was glued using non-conductive epoxy to the front face of the tine. A 15 μm gold wire was a glued to the short end of the tungsten wire with conductive silver epoxy[7]. A short length of copper wire (0.5 mm diameter) was glued to the base to provide a link between the gold and the capacitance detector. A right angle bend was placed in the gold wire close to the tine, this created a natural hinge and relieved strain in the wire, the free end was then glued with conductive epoxy to the copper wire. Finally the tungsten wire was electrochemically etched to give a sharp tip.

4.4.3 Tip etching

Tungsten is chemically inert and very hard making it a suitable material from which to fabricate SPM tips. In order to create a sharp tip the tungsten wire is immersed in a beaker of 2.5 M NaOH and a DC voltage ($\approx$ 2.5 V) is applied between the wire and an electrode in the solution. The reagents formed in the reaction sink through the solution and whilst doing so protect the wire beneath the surface. Preferential etching at the surface creates a neck in the wire and at some point this can no longer support the weight of the tungsten under the surface. The stretching and eventual snapping of the wire has the desired effect of creating a very sharp tip. After etching the tip is immediately washed in high purity water and blown dry with nitrogen.

Previous experiments have shown that the time taken to remove the bias after the wire has snapped is the most significant factor in determining the tip radius [85]. A design from the literature is used to control the etch current [86]. This has a differentiator to detect sudden changes in the etch current and removes the applied voltage in

[5] JB Weld

[6] Advent Research Materials W5574

[7] Epotek E2101

a few microseconds.

The length of wire under the surface determines at what point and how suddenly the wire breaks, too little wire under the surface and the wire may not break, too much wire and the energy released can melt the end of the tip. Typical tip radii of 30 nm are obtained with 0.5 mm of wire below the surface.

4.4.4 Calibration of the Oscillation Amplitude

The TF current I_{tf} is directly related to the velocity and is proportional to the mechanical amplitude. The mechanical amplitude a can be expressed in terms of the current:

$$a = \frac{I_{tf}}{4\pi\alpha f_0} \tag{4.4}$$

where α is the piezoelectric coupling constant.

Methods for calibrating the oscillation amplitude of TFs include optical interferometry [87], thermal noise measurements [88], and using the AFM control apparatus. Optical interferometry is very accurate but impractical for low temperature calibration. Calibration from the thermal noise spectrum requires an estimate of the spring constant from the geometry of the fork. In the AFM method the z-position of the scan tube is recorded as a function of the oscillation amplitude. As the drive voltage to the TF is reduced then the oscillation amplitude is decreased the the scan tube will extend to bring the tip back into contact with the surface. The amount that the scan tube has to extend is related to the change in the oscillation amplitude. As long as the calibration of the scan tube is known then the oscillation amplitude can be calibrated in terms of the drive voltage or current. This method allows quick calibration at any temperature and magnetic field for which scan tube calibration is known.

Although the closest point of approach between the tip and the sample is amplitude dependent, this effect is very small compared to the amplitude and does not introduce a significant error to the calibration.

Figure 4.6(a) shows a low-temperature calibration giving a value of $\alpha = 12 \pm 1\,\mu$C/m. A value of $\alpha = 4.26\,\mu$C/m was obtained by Rychen *et al.* [87]. In their experiments

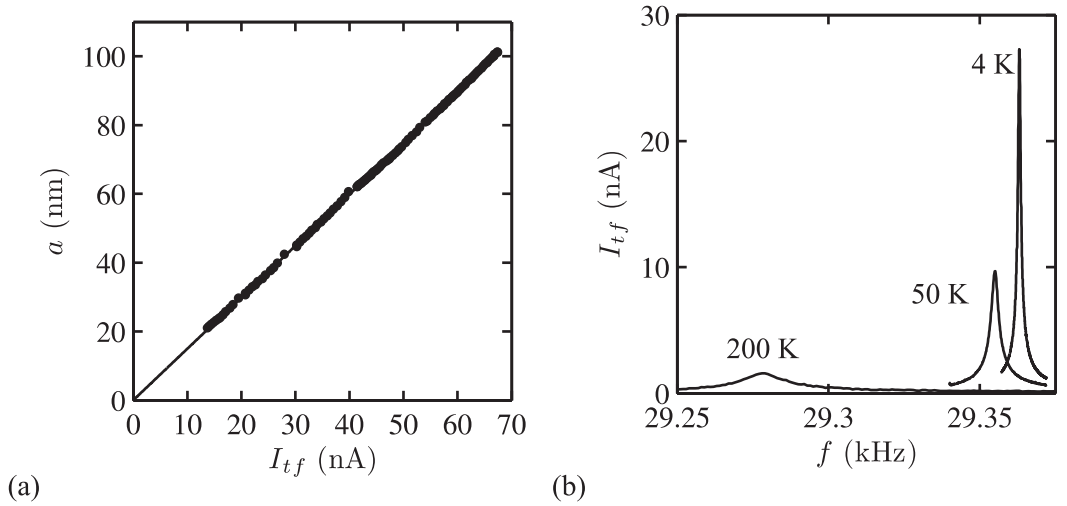

Figure 4.6: (a) Tuning fork amplitude as a function of current. The straight line is a linear fit of the data. (b) TF response as a function of temperature.

both tines were free and the fork had slightly different dimensions.

4.4.5 Temperature and Field dependence

The quality factor and resonant frequency of the TF increase with decreasing temperature. Between 300 K and 2 K the frequency increases approximately 100 Hz and the quality factor by an order of magnitude. The increase in quality factor at lower temperatures is probably due to a reduction in losses as the adhesive used to mount the fork becomes stiffer. Figure 4.6(b) shows the response of a typical sensor at different temperatures.

With increasing magnetic field the general trend is an increase in resonant frequency and a decrease in quality factor. Sensors typically show a linear increase in frequency of between 0.1 and 0.5 Hz/T at high field. The low field behaviour varies between sensors and can show increasing and decreasing frequency as a function of field. The quality factor falls by approximately an order of magnitude between 0 and 10 T. Again, the low field behaviour can be more unpredictable. It might be that ferrous material in the contacts or tuning fork leads is responsible for the behaviour at low field. Figure 4.7

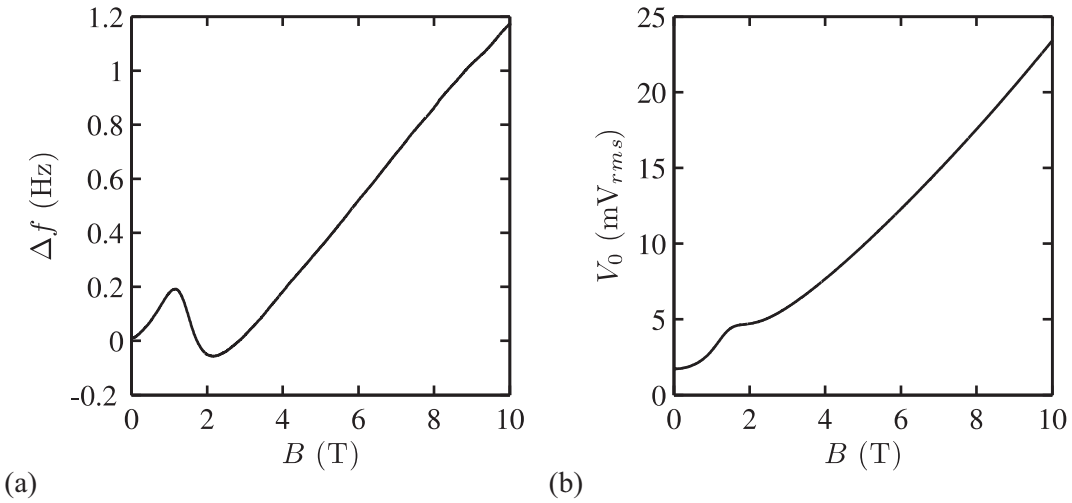

Figure 4.7: (a) Frequency shift versus field. (b) Drive voltage to maintain constant amplitude versus field.

shows the frequency shift and drive voltage in constant amplitude mode as a function of magnetic field.

4.4.6 Future improvements

The current sensor design is sensitive to acoustic excitation which appears to be linked to the attachment of the gold wire. A design has been developed where the free length of the gold wire is reduced by supporting it close to the tine by a rigid post. Room temperature experiments suggest this has resolved the problem but low temperature measurements are needed to confirm this.

An oxide layer forms on the surface of tungsten which can vary the work function difference between the tip and the sample. Changing the tip material to a platinum-iridium alloy would avoid these problems. However, it is more difficult to etch.

4.5 AFM Detection and Control

An FM detection scheme is used for the AFM control where the shift in resonant frequency from the unmodified value is used to determine and control the tip-sample

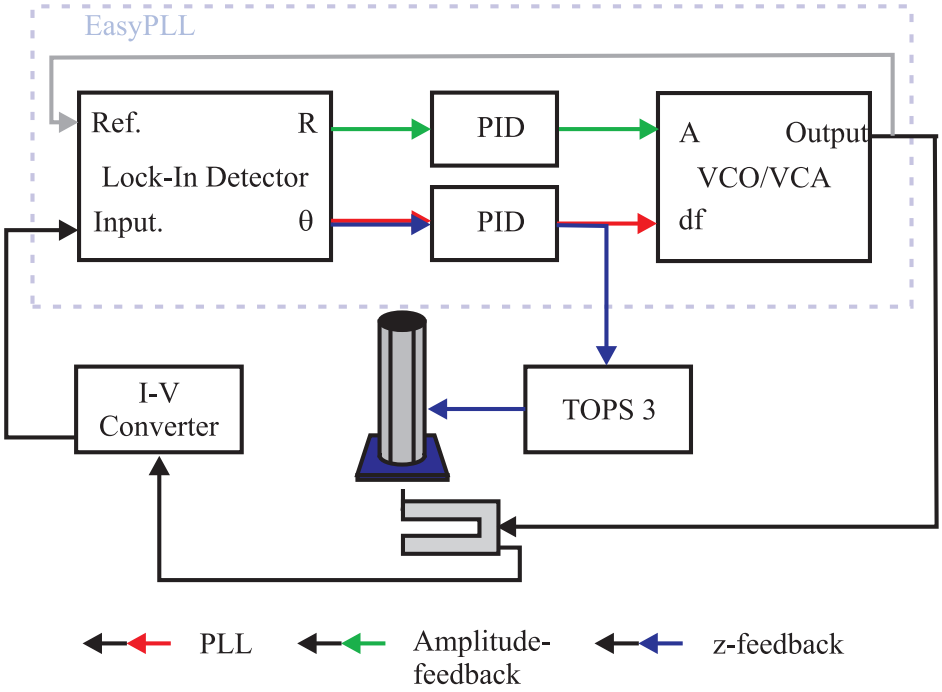

Figure 4.8: Schematic showing AFM detection and control loops.

separation. The oscillation amplitude is kept constant by adjusting the drive voltage. This technique was chosen because as well as performance advantages the frequency shift and drive signals can be directly related to the 'conservative' and 'dissipative' components of the force per cycle respectively [89]. The AFM control system has three feedback loops and is illustrated in the schematic in Fig. 4.8. The first feedback loop is a phase-locked-loop and keeps the phase of the tuning fork current at a set point by adjusting the frequency of the drive signal. The phase set point is chosen so that the tuning fork is always driven at its resonant frequency. The second feedback loop controls the mechanical amplitude of the tuning fork by adjusting the drive amplitude to keep the current amplitude constant. The third feedback loop tracks the surface with the scan tube by maintaining a set frequency shift at the output of the PLL.

A commercial PLL operates the first two feedback loops and a commercial SPM controller[8] runs the z-feedback. The SPM controller is also responsible for scanning

[8]TOPS3 Oxford Instruments

and data acquisition.

4.5.1 PLL

To save development time a commercial product [9] was used for the tuning fork PLL and amplitude control. This has constant excitation, constant amplitude and self excitation modes of operation. The PLL is operated in constant amplitude mode with a lock range of ±183 Hz and an output bandwidth of 120 Hz giving a frequency noise of $< 20\,\mathrm{mHz}/\sqrt{\mathrm{Hz}}$.

4.5.2 *I-V* amplifier

Figure 4.9 shows schematic diagrams of the *I-V* amplifier and the equivalent circuit of a quartz tuning fork. The quartz tuning fork equivalent circuit consists of a series LCR in parallel with some stray package capacitance [87]. The series LCR reproduces the harmonic oscillator behaviour of the tuning fork. The inductance L_{TF}, resistance R_{TF} and capacitance C_{TF} reflect the mechanical properties of mass, dissipation and spring constant respectively. In parallel with the series LCR there is some stray package capacitance C_p between the leads and contacts. The amplifier design, as shown in Fig. 4.9(a), is a current-to-voltage (*I-V*) converter with a simple bridge at the input to negate the package capacitance, C_p, of the tuning fork. To set the compensation, the drive frequency was set well above the resonant frequency, 80 kHz for example, and R_c was then adjusted to minimize the output. Figure 4.10 shows typical TF response curves with and without compensation of the package capacitance. Without compensation there are closely spaced resonant frequencies that produce the same phase and would cause the PLL to be unstable. The gain of the amplifier G is given by:

$$G = \frac{R_g}{1 + 2\pi f R_g C_g} \tag{4.5}$$

where R_g is the feedback resistor, C_g the associated stray capacitance and f is the frequency. A lock-in-amplifier and current source were used to calibrate the gain at 30 kHz

[9] EasyPll Plus - NanoSurf

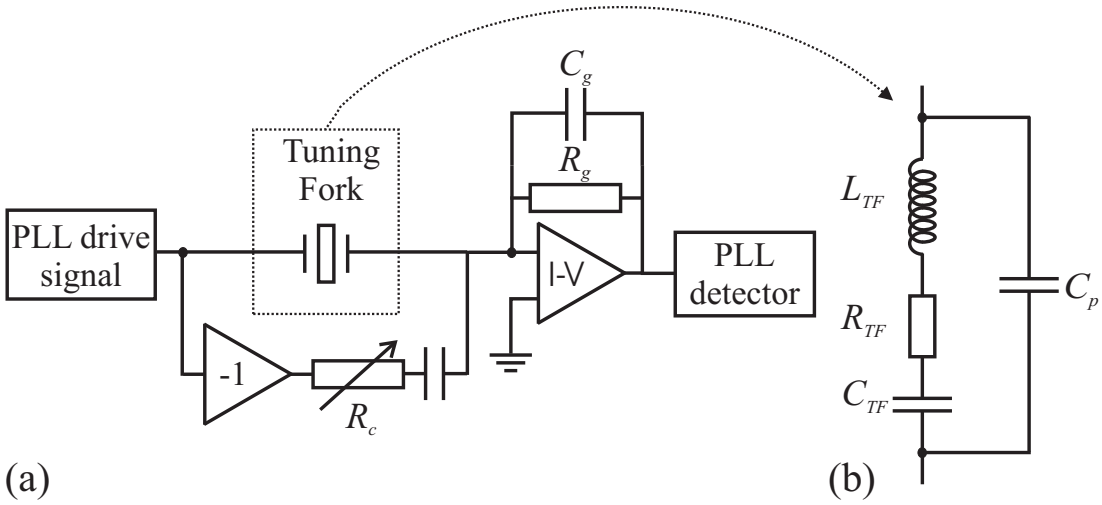

Figure 4.9: (a) Schematic of tuning fork *I-V* amp. (b) Equivalent circuit of a quartz tuning fork.

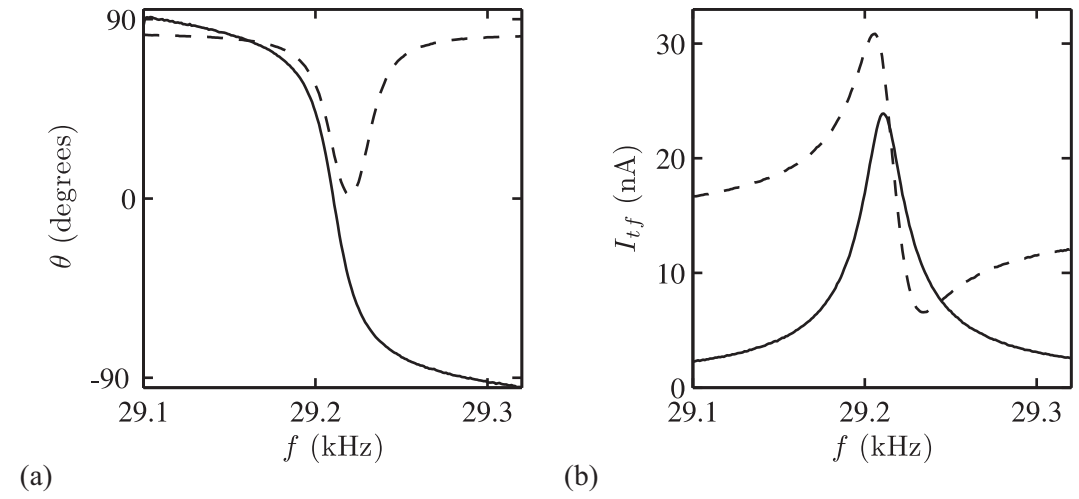

Figure 4.10: (a) Phase and (b) magnitude of the TF current with (solid line) and without (dashed line) compensation of the package capacitance.

which was found to be $2.2 \times 10^6\,\mathrm{V/A}$. The equivalent current noise of the amplifier was measured as $2\,\mathrm{pA}/\sqrt{\mathrm{Hz}}$.

4.6 Sample wiring

Direct connections to the sample are made via low-pass filters on the end of the z-module. The low pass filters were included to protect the sample from capacitive pick up of the coarse motor drive signal. They have a cut-off frequency of 1 kHz. Fig. 4.3(b) is an end view of the z module showing the filters.

4.7 Summary

This chapter has described the development of a low temperature AFM/SCM. Measurements can be made at temperatures as low as 1.5 K and magnetic fields up to 12 T. The AFM/SCM sensor is based on a piezoelectric quartz tuning fork with an etched tungsten tip. The piezoelectric QTF is implemented in a self exciting/detecting configuration avoiding alignment problems and stray light associated with optical deflection measurements. AFM measurements are made in a dynamic mode, a PLL tracks the resonant frequency of the tuning fork and the frequency shift is used as the feedback signal for the height control. A separate feedback loop maintains a constant oscillation amplitude. Capacitance measurements are made using an RF tuned filter design which is discussed in detail in the next chapter.

Chapter 5

Capacitance detection

Several techniques can be used to measure capacitance, for example bridge methods [90], charge measurement [91] or RF techniques [65]. The bridge and charge measurement techniques are more suited to slow and absolute capacitance measurements because the background has to be compensated for each measurement individually. An RF technique based on a tuned filter design allowed changes in capacitance to be measured accurately and with a bandwidth adequate for scanning [65].

The RF-response of a tuned filter circuit was measured with the central resonator connected to the metallic tip of an AFM in tapping mode. Changes in the tip-sample interaction modify the frequency and quality factor of the tuned filter which in turn changes the transmission of the signal. In order to discriminate the local capacitance ($\approx 10^{-17}\,\mathrm{F}$) from the background, stray capacitance ($\approx 10^{-12}\,\mathrm{F}$), we employ the following technique: the tip oscillation modulates the tip-sample capacitance $C_{ts}(t)$. By using lock-in techniques we measure the resulting modulation of the RF signal. With highly conductive samples the system response is dominated by changes in the tip-sample capacitance. However, for large resistances, for example in the QHE regime, this is no longer true.

After calibration it is possible to determine the tip-sample capacitance with sub-attofarad resolution with a spatial resolution of less than 100 nm.

Figure 5.1 shows a schematic of the detection set-up. An RF source provides the

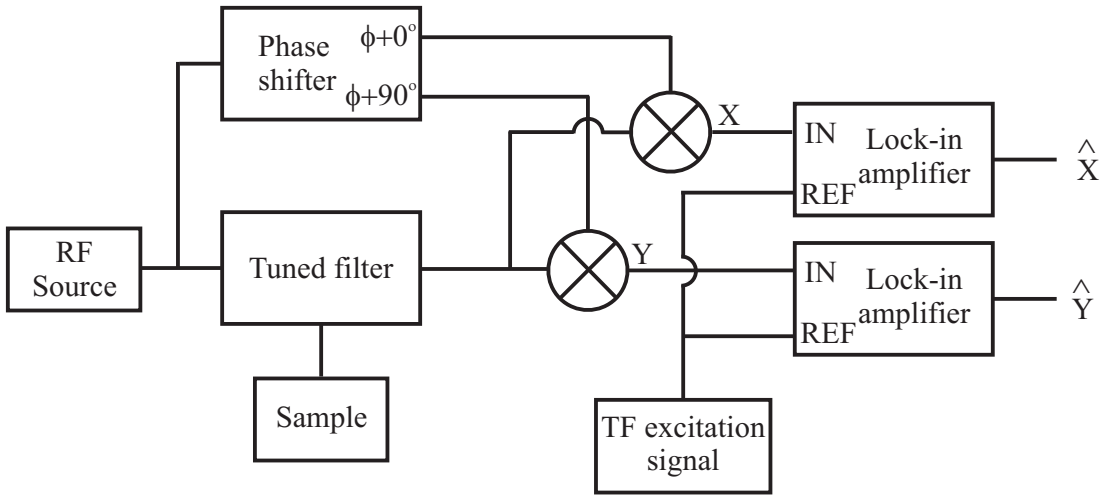

Figure 5.1: Schematic of capacitance detection set-up. An RF tuned filter is used to detect changes in the tip-sample interaction. The in-phase X and quadrature Y components of the RF signal are recovered using mixers and the modulation at the TF oscillation frequency is measured using lock-in detection.

input signal for the tuned filter and a reference signal for the detection electronics. The in-phase, X, and out-of-phase, Y, components of the output signal are recovered by mixing with reference signals at the appropriate phase. The modulation of X and Y at the tuning fork (TF) oscillation frequency, $\hat{X}$ and $\hat{Y}$ respectively, are measured using lock-in detection.

5.1 Tuned filter

The home-made tuned filter consists of three coils wound on a ceramic former. A photograph and schematic of the design are shown in Fig. 5.2. The excitation coil is used to couple power into the sense coil, the pick-up coil is used to measure the current in the sense coil inductively. The sense coil forms the central resonator and is connected to the tip. The transmission of the signal through the tuned filter depends on the impedance of the sense coil which is in turn influenced by the tip-sample interaction.

The design of the coil was constrained by the available space on the microscope

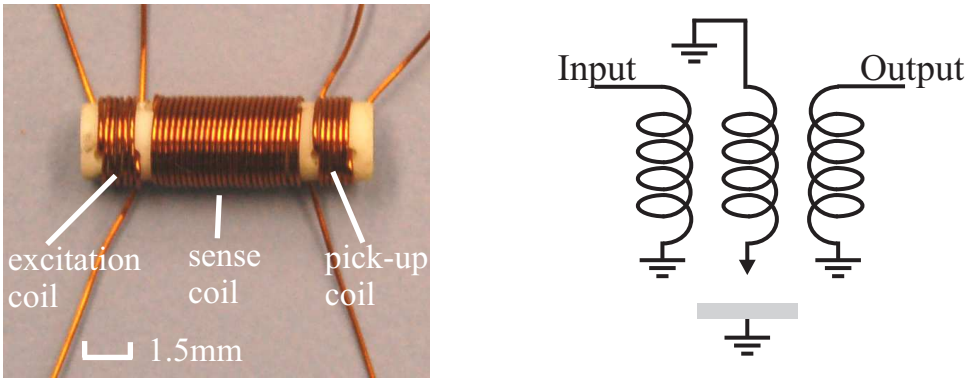

(a) (b)

Figure 5.2: (a) Photograph of the tuned filter showing three coils wound on to a ceramic former. (b) Schematic of the tuned filter.

head and the requirement of a resonant frequency of approximately 100 MHz. The frequency is determined by the inductance of the sense coil, the tip-sample capacitance and stray capacitances. The position and inductance of the excitation and pick-up coils control the coupling to the sense coil. The coupling needs be strong enough to generate a measurable signal, however, as the coupling is increased the quality factor of the resonance is reduced and susceptibility to noise in the external circuits is increased. The parameters of the tuned filter were optimized by experimentation.

5.1.1 Equivalent circuit model

An equivalent lumped element circuit model of the tuned filter has been developed and is shown in Figure 5.3. The components have been characterized individually, as discussed below, and the values are summarized in Table 5.1.

5.1.2 Calibration of the coil inductance

The inductance of the coils was determined by measuring the voltage change in response to an abrupt change in current using a method described in Ref. [92]. A triangular waveform was applied to the coil under test, L_i, whilst monitoring the voltage, V_i,

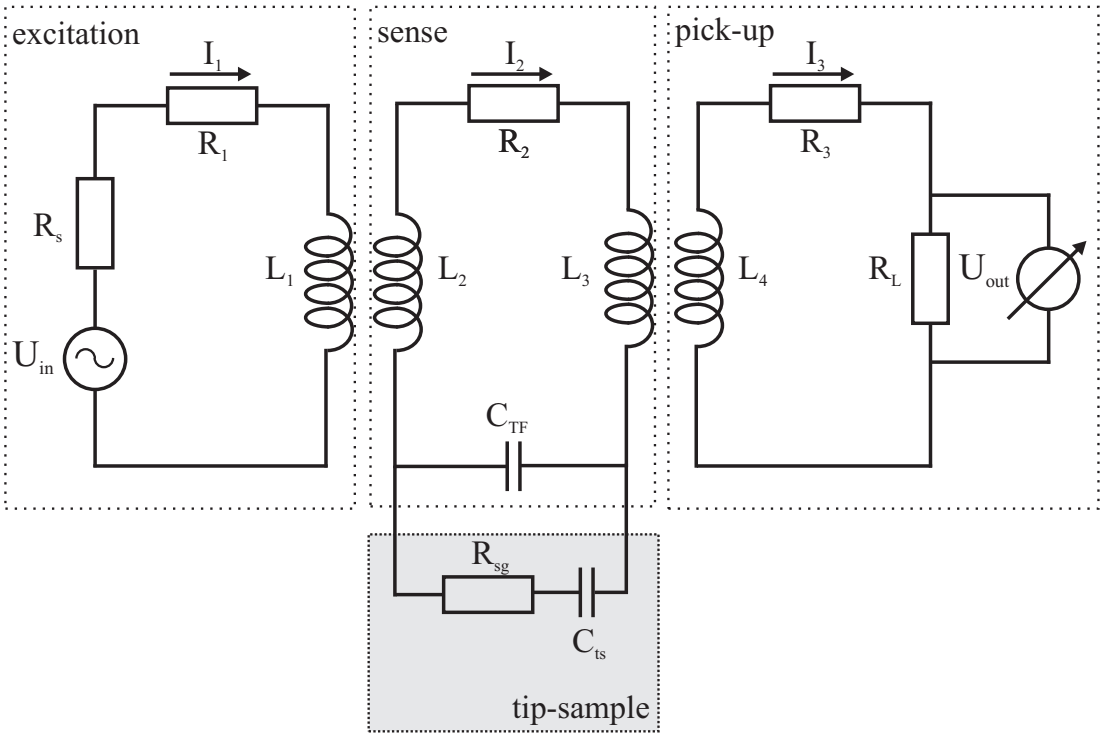

Figure 5.3: Equivalent circuit model of the tuned filter, drive and detection circuits.

Parameter	Description	Value
$R1, R3$	wire resistances	$0.5\,\Omega$
$R2$	resistance of the sense coil	$0.17\,\Omega$
$L1, L4$	excitation, pick-up coil inductance	$0.16\,\mu$H
$L = L2 = L3$	sense coil inductance	$0.88\,\mu$H
R_s	output impedance of the RF source	$50\,\Omega$
R_L	input impedance of the detector	$50\,\Omega$
C_{TF}	stray capacitance	2 pF
C_{ts}	tip-sample capacitance	sample dependent
R_{sg}	resistance between sample and ground	”

Table 5.1: Description and values of the components in the equivalent circuit model measured at room temperature.

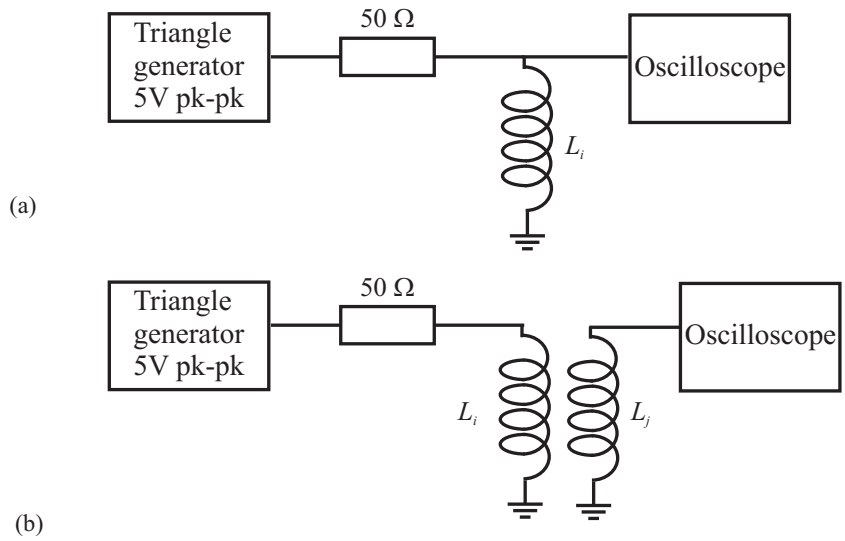

Figure 5.4: Circuits used to calibrate the coils of the tuned filter. (a) Inductance and resistance of a single coil. (b) Mutual inductance between two coils.

across the coil with an oscilloscope. A circuit diagram is shown in Figure 5.4(a). The frequency was adjusted such that the voltage appearing across the coil was less than 1 % of the function generator output. This ensured the current had a triangular form. Figure 5.5(a) shows the applied current and the voltage across the coil.

At the apex of the triangular wave the current changes slope abruptly and an inductive jump V_L is seen in V_i. The inductance L_i is given by:

$$L_i = \frac{V_L}{2dI/dt} \tag{5.1}$$

where dI/dt is the current slope and the factor of two appears because the slope changes from positive to negative and the voltage is measured peak-to-peak. The second component of the V_i trace is a linear slope due to the voltage drop, V_R, across the resistive part of the coil. The coil resistance, R_i, is given by:

$$R_i = \frac{V_R}{\Delta I} \tag{5.2}$$

The inductances of the individual coils were measured with the other windings removed to exclude any mutual inductance contribution. The mutual inductance between the coils was measured by applying a triangular waveform to one coil and measuring the

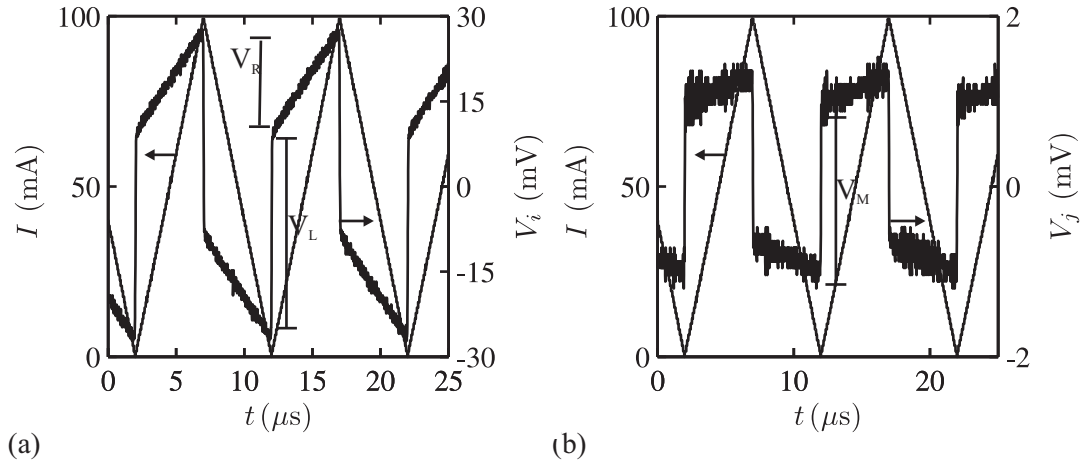

Figure 5.5: (a) Calibration of the sense coil at 100kHz. Graph shows applied current and voltage developed across the coil. Parameters of the sense coil are calculated as $L = 0.88\,\mu$H, $R = 0.17\,\Omega$. (b) Measurement of mutual inductance between excitation coil and central coil showing the applied current and induced voltage. $M_{12} = 0.05\,\mu$H.

voltage, V_M, induced in the second coil. A circuit diagram is shown in Figure 5.4(b). The mutual inductance is given by:

$$M_{12} = \frac{V_M}{2dI/dt} \tag{5.3}$$

Figure 5.5(b) shows the induced voltage on the sense coil for a current applied to the excitation coil.

Through measurement of the individual inductances and their mutual inductances it is possible to calculate the coupling coefficients of the coils using:

$$k_{ij} = \frac{M_{ij}}{\sqrt{(L_i L_j)}} \tag{5.4}$$

The coupling between the excitation coil and the sense coil is $k = 0.13$. The tuned filter design is symmetric and therefore the coupling between the sense coil and the pick-up coil is the same.

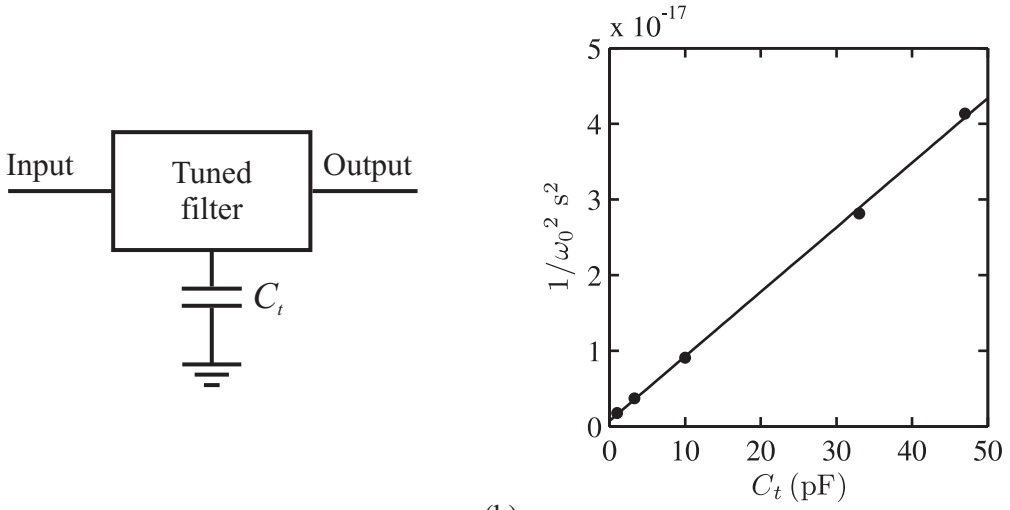

Figure 5.6: Calibration measurement to establish relationship between the stray capacitance C_{TF} and the resonant frequency of the tuned filter.

5.1.3 Calibration of the stray capacitance

The majority of the stray capacitance C_{TF} originates from coupling between the tip and the electrodes of the tuning fork. The size of the stray capacitance C_{TF} makes direct measurement difficult. The resonant frequency of the tuned filter was used to calculate the stray capacitance, Figure 5.6 shows the resonant frequency for a number of test capacitances, C_t, placed in parallel with the sense coil. The behaviour can be described accurately by an LCR circuit where the resonant frequency ω_0 is given by:

$$\omega_0{}^2 = \frac{1}{LC} \tag{5.5}$$

The inductance can be calculated from the gradient and has value of $0.86\,\mu$H, this is in agreement with the direct measurement of L. With the sensor attached to the resonator we find a stray capacitance of $C_{TF} \approx 2.1\,$pF.

5.1.4 Transfer function

The equivalent circuit model is used to approximate the transfer function of the tuned filter. The output voltage U_{out} with no tip-sample interaction is given by [65]:

$$U_{out} = -\frac{\omega^2 M_{12} M_{34} R_L}{Z_1(\omega) Z_3(\omega)} \frac{1}{R_2 + i\omega L + \frac{1}{i\omega C_{TF}} + Z_c} U_{in} \tag{5.6}$$

where M_{ij} is the mutual inductance between the coils L_i and L_j, $Z_1 = R_1 + iwL_1$ and $Z_3 = R_3 + iwL_4$.

The effect of the coupling appears in the term Z_c, the impedance seen by the sense coil due to the coupling to the excitation and pick-up circuits and is given by:

$$Z_c = \frac{\omega^2 {M_{12}}^2}{Z_1} + \frac{\omega^2 {M_{34}}^2}{Z_3} \tag{5.7}$$

The response of the tuned filter can be approximated by an LCR or harmonic oscillator model with effective component values calculated at the resonant frequency:

$$U_{out} = \frac{A}{R_{eff} + i\omega L_{eff} + \frac{1}{i\omega C_{TF}}} U_{in} \tag{5.8}$$

where $L_{eff} = L - \mathrm{Imag}(Z_c)/w = 0.85\,\mu\mathrm{H}$ and $R_{eff} = R_2 + \mathrm{Real}(Z_c) = 8.1\,\Omega$ and $A = -\frac{\omega^2 M_{12} M_{34} R_L}{Z_1 Z_3} = 4$.

Figure 5.7 shows the measured response of the tuned filter, the predicted response from the full equivalent circuit model and the harmonic oscillator approximation without fitting. The two models are in excellent agreement with each other and in good agreement with the experimentally measured curve. The deviations probably result from additional stray inductances and capacitances not included in the models.

5.2 Detection system

Passive mixers are used to extract the in-phase, X, and quadrature, Y, components of the signal. Appropriate reference signals are generated from the drive signal using a variable phase shifter and a $0/90^\circ$ power splitter. With the tip withdrawn the variable phase shifter is adjusted so that X is a maximum at the resonance frequency.

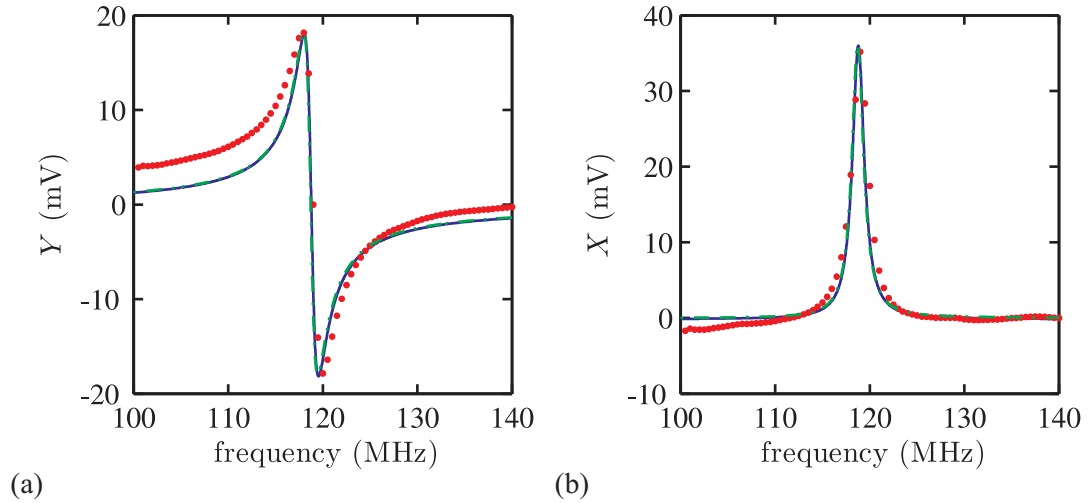

Figure 5.7: Frequency response of the tuned filter, measured response(red markers), full equivalent circuit model (blue line), harmonic oscillator model (green dashed line). (a) Y response. (b) X response.

The RF signal is modulated by the sensor oscillation, which allows the local contribution to be separated from the large background signal. $\hat{X}$ and $\hat{Y}$ are the components of X and Y at the TF oscillation frequency and are measured using lock-in-amplifiers.

5.2.1 Tip-sample voltage

In our experiment the tip voltage U_{tip} should be small in order not to disturb the sample too strongly. Assuming the impedance of the tip-sample interaction is much larger than that of C_{TF} then from the equivalent circuit model we find:

$$U_{tip} = \frac{M_{12}}{C_{TF} Z_1 [R_2 + i\omega L + \frac{1}{i\omega C_{Tf}} + Z_c]} U_{in} \tag{5.9}$$

Using the measured component values then $U_{tip} = 8.7 \times U_{in} \approx 0.5\,\mathrm{mV}$.

5.3 Sample simulation

We approximate the effect of the electrical tip-sample interaction on the tuned filter by a simple RC model. The coupling between the tip and sample is represented as

purely capacitive, C_{ts}, whereas the sample is represented by a resistance to ground, R_s. The response of the tuned filter to different tip-sample parameters is not simple. For each sample values for R and C will be estimated and the equivalent circuit model will be used to determine to which parameter or parameters the measurement is sensitive. The aim for each sample is to be able to identify regimes where it is possible to make a straight forward interpretation of the measurement. This will be discussed in full in the chapters describing the measurements made on particular samples.

5.4 Summary

This chapter has described a capacitance detection scheme based on an RF tuned filter design. An equivalent circuit description of the detector has been developed and careful calibrations of the individual components have been carried out. The response calculated with the model is in good agreement with the experimentally measured response. Chapter 6 describes some measurements made above a gold film and deconvolution of the $C(z)$ curve from the measured quantities. Chapter 7 discusses measurements made over a 2DEG at zero field and in the quantum Hall regime.

Chapter 6

SCM measurements above a gold film

In this chapter point spectra and scanning measurements of a thin gold film at room temperature are discussed. The motivation for these measurements was to investigate force and capacitance as a function of tip-sample separation. These measurements were made on a gold film as it is a simple well-defined metallic surface.

The tapping mode AFM technique means that the measured quantities are an average of the tip-sample interaction over an oscillation cycle of the tuning fork. A generalized deconvolution scheme will be discussed and used to extract force and capacitance as a function of the tip-sample separation, from point spectra measurements, of the frequency shift and $\hat{Y}$ signals.

6.1 Sample

The sample consists of a 100 nm thick gold film evaporated on to a 4 mm^2 piece of undoped silicon wafer (100) 0.1 mm thick. The film is connected to ground by metallic bond wires.

Parameter	Value	Impedance $\|Z\|$ at 120 MHz
C_{ts}	0.2 pF	6 kΩ
R_{sg}	0.5 Ω	0.5 Ω

Table 6.1: Model parameters for gold sample.

6.1.1 Lumped circuit model

Values for the lumped circuit elements of the sample model discussed in Section 5.3 have been estimated for the gold sample and are given in Table 6.1. The tip-sample capacitance, C_{ts}, was estimated from the frequency shift of the tuned filter during the approach of the tip to the surface. The sample resistance, R_{sg} was estimated using a simple model shown in Figure 6.1(a). Assuming the RF signal couples into a small region in the centre of the film $r < r_1$ (potential U_1) the resistance R_{sg} to the boundary $r = r_2$ (Potential U_2) is given by:

$$R_{sg} = \frac{U_2 - U_1}{I} = \frac{\ln(r_2/r_1)}{2\pi\sigma_{xx}^{2D}} \tag{6.1}$$

where $\sigma_{xx}^{2D} = T/\rho_{xx}$ is the 2D longitudinal conductivity of gold, T is the film thickness and ρ_{xx} is the resistivity of gold. Figure 6.1(b) shows the calculated film resistance R_{sg} for a range of r_1 between 10 nm and 10 μm. Over this range R_{sg} does not exceed 0.5 Ω.

Comparing the impedances of the lumped circuit elements (Table 6.1) the model of the gold sample can be reduced to the tip-sample capacitance C_{ts}.

The transfer function of the unperturbed tuned filter was discussed in Section 5.1.4. For the gold sample the tip-sample interaction can be simplified to an additional capacitance C_{ts} in parallel with C_{TF}, the stray capacitance to ground through the tuning fork. The transfer function is then given by:

$$U_{out} = \frac{A}{R_{eff} + i\omega L_{eff} + \frac{1}{i\omega(C_{tot})}}.U_{in} \tag{6.2}$$

where $C_{tot} = C_{TF} + C_{ts}^{(0)} + \Delta C_{ts}$, $C_{ts}^{(0)}$ is the tip-sample capacitance with the tip withdrawn and ΔC_{ts} is the change in the tip-sample capacitance.

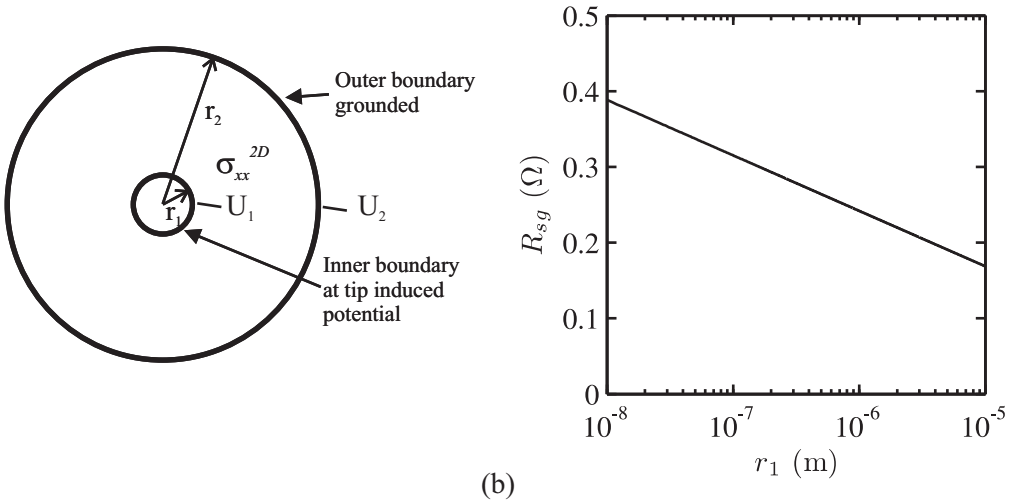

(a) (b)

Figure 6.1: (a) Model used to estimate the resistance of the gold film R_{sg}. The signal couples into a small region $r < r_1$ and the gold film is grounded at the boundary $r = r_2 = 2\,\mathrm{mm}$. (b) Calculated R_{sg} versus r_1 with $r_2 = 2\,\mathrm{mm}$.

Response of Y to changes in C_{ts}

The quadrature component of the RF signal, Y, is given by:

$$Y = -\frac{A\left(\omega L_{eff} - \frac{1}{\omega C_{tot}}\right)}{{R_{eff}}^2 + \left(\omega L_{eff} - \frac{1}{\omega C_{tot}}\right)^2} U_{in} \tag{6.3}$$

A Taylor expansion of $Y(\Delta C_{ts})$ about $\Delta C_{ts} = 0$ gives:

$$Y \approx -\frac{AU_{in}}{\omega_0 C_{tot} {R_{eff}}^2}\left(-\frac{\Delta C_{ts}}{C_{tot}} + \left(\frac{\Delta C_{ts}}{C_{tot}}\right)^2 + ...\right) \tag{6.4}$$

for $\Delta C_{ts} \ll C_{tot}$ the first order term is a good approximation. Over the range which this approximation is valid, Y is proportional to ΔC_{ts} and a constant of proportionality $K_g = dY/dC = -A/{C_{tot}}^2 {R_{eff}}^2 . U_{in}$ can be defined. For the gold sample dominated by the geometric capacitance between the tip and sample surface $K_g \approx 0.16\,\mu\mathrm{V/\,aF}$.

Response of X to changes in C_{ts}

The in-phase component of the RF signal X is given by:

$$X = \frac{AR_{eff}}{{R_{eff}}^2 + \left(\omega L_{eff} - \frac{1}{\omega C_0}\right)^2} U_{in} \tag{6.5}$$

Performing a Taylor expansion of $X(\Delta C_{ts})$ about $\Delta C_{ts} = 0$ gives:

$$X \approx \frac{AU_{in}}{R_{eff}} - \frac{AL_{eff}U_{in}}{{C_{tot}}^3 {R_{eff}}^2} {\Delta C_{ts}}^2 + ... \tag{6.6}$$

Note that there is no first order term in ΔC_{ts}. This approximation can be reduced to the zero order term for $\Delta C_{ts} \ll \sqrt{{C_{tot}}^3 {R_{eff}}^2 / L_{eff}} \approx 0.1\,\mathrm{fF}$ for the setup. The parameters A and R_{eff} are constant and therefore the in-phase signal is expected to be a constant for measurements made on metallic samples.

6.2 Point Spectra

AFM and SCM measurements were made as a function of the tip-sample separation over a single point. The motivation for these experiments was to investigate the form and length scale of the tip-sample force and capacitance and make comparisons to simple models and measurements in the literature.

The dynamic AFM technique used in the experiments introduces significant complexity into the interpretation of these measurements as the length scale of the interactions is comparable to the oscillation amplitude. A deconvolution scheme usually used for force-distance curves is generalized and used to extract $C_{ts}(z)$ from the $\hat{Y}(z)$ measurement.

The point spectra measurements were made at room temperature and under vacuum. The AFM control was used locate the surface, the tip was then left controlling over a single point for a number of minutes. This was to minimize creep of the scan piezo influencing the measurement. Point spectra measurements were made by switching off the height feedback loop before varying the tip-sample separation. Data were acquired whilst retracting and then approaching the surface. The PLL was used to

track the resonant frequency and maintain a constant oscillation amplitude of the tuning fork sensor (see Section 4.5). Capacitance measurements were made as described in Chapter 5. The frequency shift Δf, drive voltage, $\hat{Y}$ and $\hat{X}$ were acquired simultaneously. Each point spectrum took approximately 30 s. Measurements were made as a function of oscillation amplitude and are discussed in the next section.

6.2.1 Description of the data

Frequency shift and dissipation versus z

Figure 6.2(a) shows the frequency shift and drive force as a function of tip-sample separation z. The z scale is relative to the the point $z = 0$ which is where the height feedback loop was controlling before making the measurement. All of these curves were measured in both directions and no significant hysteresis was observed. At large z all the curves show a slow decrease of Δf with decreasing z until a minimum is reached. At closer separations Δf increases sharply with a gradient of up to 1 Hz/nm at an oscillation amplitude of 10 nm. At larger oscillation amplitudes the size of the frequency shifts are reduced. This is in agreement with theoretical predictions [45] and other experimental observations [87]. The minimum in the frequency shift is shifted to increased z with increasing oscillation amplitude. This shift is because the tip has to come closer to the sample to maintain the same frequency set point with a larger oscillation amplitude. The change in the Δf versus z curves indicates that the oscillation amplitude is large compared to the length scale of the tip-sample force F_{ts}.

As discussed earlier the frequency shift of the tuning fork can be approximated by [45]:

$$\Delta f \approx -\frac{f_0}{k_0 a^2} \langle F_{ts} z \rangle \tag{6.7}$$

where $\langle ... \rangle$ denotes the average over one cycle. If the oscillation amplitude, a,is greater than the length scale of the tip-sample force then further increases in amplitude will reduce the portion of the cycle over which F_{ts} is experienced and thereby will reduce the resulting frequency shift.

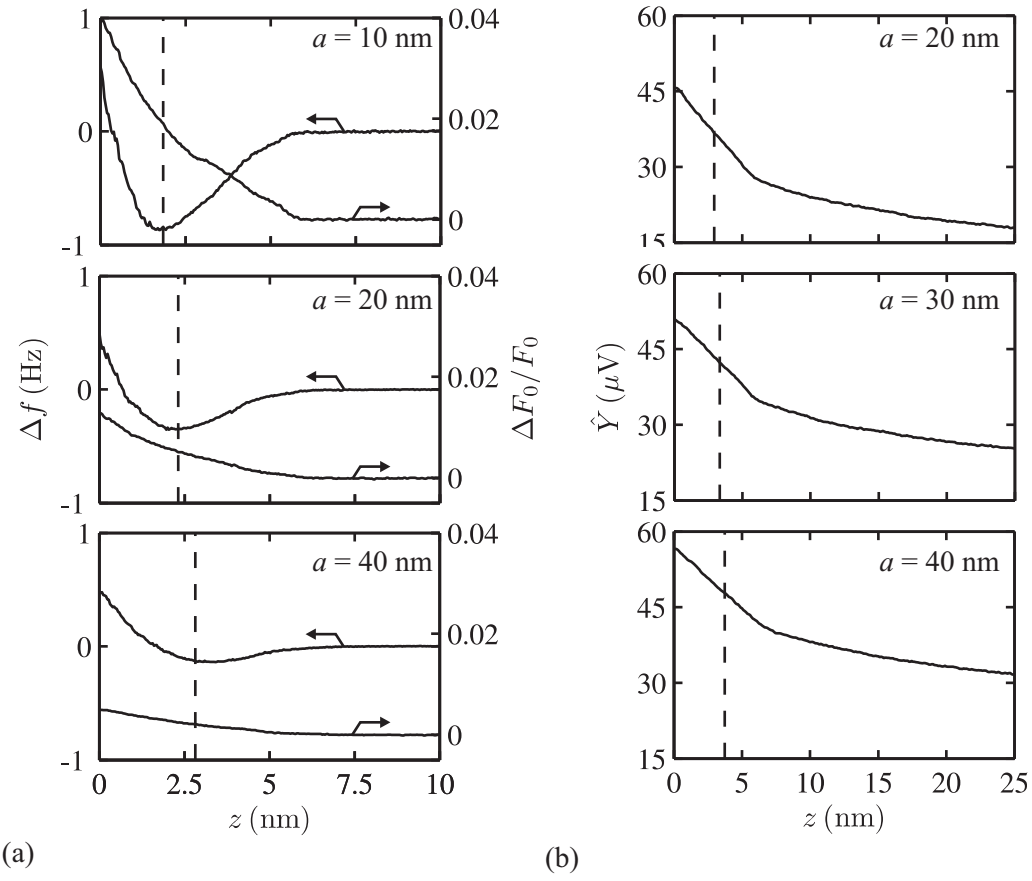

Figure 6.2: (a) Frequency shift and drive force versus tip-sample separation for different oscillation amplitudes. (b) $\hat{Y}$ is a function of tip-sample separation for different oscillation amplitudes. Note that the data in Figures (a) and (b) are from different experiments.

The change in the drive force is a small percentage of drive force away from the surface. An increase in the drive force indicates that the PLL is providing more energy to the tuning fork to maintain a constant oscillation amplitude. This additional energy is compensating dissipation in the tip-sample interaction. The onset of dissipation occurs at tip-sample separations where the frequency shift is negative and increases with decreasing z. The change in drive force or dissipation is smaller for larger oscillation amplitudes. This is because at larger oscillation amplitudes the tip spends less time close to the surface and the energy of the tuning fork is greater.

The dissipated power can be calculated from $P = U_{exc} I_{tf}$ where U_{exc} is the excitation voltage applied to the tuning fork and I_{tf} is the resulting current. With an oscillation amplitude of 10 nm then the electrical power supplied away from the surface is 50 pW. At the closest tip-sample separation this rises to 52 pW. The additional dissipation could be due to the induced kelvin current, phonon emission into the tip and sample or a water layer on the sample in the non-UHV situation.

$\hat{Y}$ versus z

Figure 6.2(b) shows the $\hat{Y}$ signal versus tip-sample separation z for different oscillation amplitudes. No curves of $\hat{X}$ have been included as the signal was very small and did not depend on z within the measurement resolution. Note that the z scale is now 25 nm and not 10 nm as in Figure 6.2(a). The dashed line indicates the position of the minimum in the simultaneously measured Δf curve (not shown) for orientation. All three curves have the same form, a gradual increase in $\hat{Y}$ with decreasing z between $z = 25$ nm and $z \approx 7$ nm before a sudden change in gradient and a steep increase in $\hat{Y}$ for decreasing z. Increasing the oscillation amplitude increases the size of the signal and reduces the gradient of the curve. The increase in size is because a larger oscillation amplitude gives a larger change in capacitance over a cycle. The change in shape is because the measurement is averaged over a complete cycle and a larger oscillation tends to average out the detail. The point at which the curve changes shape indicates some change of regime in the electrostatics and is probably related to the size of the tip.

6.3 Deconvolution of point spectra into tip-sample force and capacitance

In the case where the oscillation amplitude is greater than the length scale of the tip-sample interaction then the measured quantities depend on the oscillation amplitude as seen in the data discussed in the previous section.

A number of numerical [93, 94] and analytical deconvolution methods [95] have been used for extracting forces from measured frequency shifts. These methods often apply under specific conditions, for example a certain range of oscillation amplitudes, or are difficult to implement. Recent work by Sader *et al* [89] presented analytical formulae to calculate the forces from measured frequency shifts valid for any oscillation amplitude. In this chapter the same mathematical formalism is used to deconvolve any quantity measured by a harmonically oscillating AFM tip. This is demonstrated for the capacitance measurements.

In the following sections the method proposed by Sader is discussed before calculating the tip-sample forces, and tip-sample capacitance from the frequency shift and $\hat{Y}$ measurements respectively.

6.3.1 Mathematical background

The following mathematics is a summary of the approach described by Sader [89].

Consider the function $\Theta(z)$ which is given as the integral of a functional $B(z)$ over an oscillation cycle:

$$\Theta(z) = -\frac{1}{ab}\frac{1}{T}\int_0^T B(z + a + q'(t)))\cos\omega t \,\mathrm{d}t \tag{6.8}$$

where T is the period of the oscillation, a is the oscillation amplitude, b is a constant, ω is the angular frequency, z is the tip-sample separation and $q'(t)$ is the displacement of the tip about z. Figure. 6.3 shows a schematic of the coordinate system used to describe the tip motion. The integral can be transformed to a function of u:

$$\Theta(z) = -\frac{1}{\pi ab}\int_{-1}^{1} B(z + a(1 + u))\frac{u}{\sqrt{1 - u^2}}\,\mathrm{d}u \tag{6.9}$$

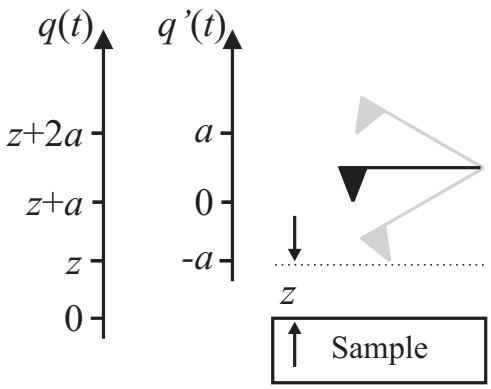

Figure 6.3: Schematic showing the coordinate system used to describe the tip motion. The minimum tip-sample separation is z and the oscillation amplitude is a. Note that $q'(t)$ is the displacement of the tip about its centre position.

The goal is to extract $B(z)$. Such problems can formally be solved by a Laplace transformation. It is not possible to perform the Laplace transform analytically. Instead the kernel was approximated by fitting an expression to the numerical solution. This leads to the following solution of the problem:

$$\begin{aligned} B(z) &= 2b\int_z^\infty \left(1+\frac{a^{\frac{1}{2}}}{8\sqrt{\pi(t-z)}}\right)\Theta(t) \\ &- \frac{a^{\frac{3}{2}}}{\sqrt{2(t-z)}}\frac{\mathrm{d}\Theta(t)}{\mathrm{d}t}\mathrm{d}t \end{aligned} \tag{6.10}$$

6.3.2 Tip-sample force

In general the tip-sample interaction force F_{ts} is a non-linear function of the separation and can differ between the approach and retract parts of the oscillation cycle. F_{ts} can be expressed as the sum of an 'even' force F_{even} and an 'odd' force F_{odd}:

$$F_{ts} = F_{even} + F_{odd} \tag{6.11}$$

The 'even' force is given by the average of the approach and retract curves and represents the contribution to F_{ts} which is given uniquely by the separation. The 'odd' force is given by the difference between the approach and retract curves and represents the contribution to F_{ts} which depends on the tip velocity and the separation. The physical

significance of these two components can be inferred by considering the work done W over a complete tuning fork cycle:

$$W = \oint \vec{F_{ts}}(\vec{s}).\vec{ds} = \int_{min}^{max} F_{ts} ds_1 - \int_{min}^{max} F_{ts} ds_2 = \int_{min}^{max} F_{odd} ds = \oint F_{odd}.ds \quad (6.12)$$

where $\vec{F_{ts}}(\vec{s})$ is the force and $\vec{ds}$ is the position vector in the direction of the tip motion. For F_{even} the work done on approach and on retraction is equal and opposite so the net work per cycle is zero. F_{even} therefore represents the conservative contribution to the work per cycle. For F_{odd} the work done in approach and retraction is identical and in general is not zero. F_{odd} represents the dissipative contribution to the work per cycle (if $W < 0$) [89].

Recovering F_{even}

Δf measures the Fourier component of F_{even}, see Eqn. 4.3. Performing a Fourier analysis gives the following expression relating the frequency shift Δf to the 'even' force [93]:

$$\frac{\Delta f}{f_0} = -\left(\frac{1}{ak_0}\right)\frac{1}{T}\int_0^T F_{even}(z + a + q'(t)) \cos 2\pi f_0 t \, \mathrm{d}t \quad (6.13)$$

By substituting $u = \frac{q'(t)}{a}$ and rearranging terms one can identify $\Theta(z) \equiv \frac{\Delta f(z)}{f_0}$, $B(z) \equiv F_{even}(z)$ and $b \equiv k_0$. Substituting these coefficients into Eqn. 6.10 leads to:

$$\begin{aligned} F_{even}(z) &= 2k_0 \int_z^\infty \left(1 + \frac{a^{\frac{1}{2}}}{8\sqrt{\pi(z'-z)}}\right)\frac{\Delta f(z')}{f_0} \\ &\quad - \frac{a^{\frac{3}{2}}}{\sqrt{2(z'-z)}}\frac{\mathrm{d}}{\mathrm{d}z'}\left(\frac{\Delta f(z')}{f_0}\right)\mathrm{d}z' \end{aligned} \quad (6.14)$$

For small amplitudes and small Δf gradients Eqn. 6.14 reduces to:

$$F_{even}(z) = 2k_0 \int_z^\infty \frac{\Delta f(z')}{f_0}\,\mathrm{d}z' \quad (6.15)$$

or, after $\frac{\mathrm{d}}{\mathrm{d}z}$:

$$\Delta f(t) = \frac{f_0}{2k_0}\frac{\mathrm{d}F_{even}(z)}{\mathrm{d}z} \quad (6.16)$$

which coincides with Eqn. 4.2. Figure 6.4(a) shows a series of experimental frequency shift Δf versus distance z curves for different mechanical oscillation amplitudes. These

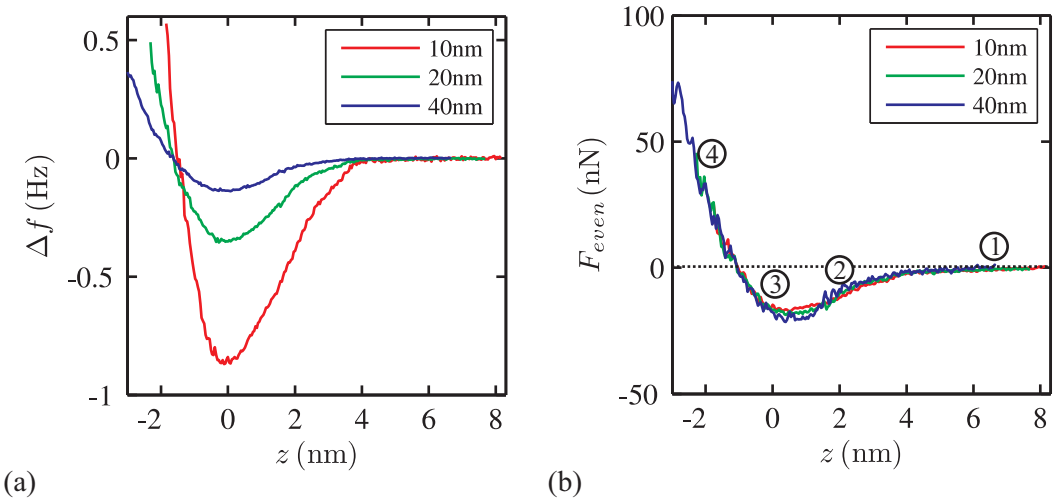

Figure 6.4: (a) Measured frequency shift versus tip-sample separation for different oscillation amplitudes. (b) Recovered F_{even}.

are discussed in detail in Section 6.2.1. The reconstructed $F_{even}(z)$ curves are plotted in Fig. 6.4(b). The curves are identical curves for all amplitudes which supports the validity of the deconvolution method.

The $F_{even}(z)$ curves shows four different regimes indicated by the labels in Figure 6.4(b). Far from the surface $z > 7\,\text{nm}$ the tip-sample force is very small and the tuning fork is unperturbed (Label 1). Closer to the surface $0.5 < z < 7\,\text{nm}$ there is a gradually increasing attractive force (Label 2). There is a minimum in the force at $z \approx 0.5\,\text{nm}$. For separations $-1 < z < 0.5\,\text{nm}$ the force gradient is reversed and the force is changing from attractive to repulsive (Label 3). At the closest separations $z < -2$ the force is repulsive and inversely proportional to z.

The form of the curve is very similar to the simple theoretical model shown in Figure 3.1. The forces are about an order of magnitude larger than the simple model. The length scale of the experimentally measured curve is about a factor of 20 larger than the model. The work function difference was not compensated in these measurements and it is probably these long range electrostatic forces that increase the size of the attractive part of F_{ts}. In the repulsive regime the theoretical curve only describes the

interaction between the most prominent tip and sample atoms. In the experiment, as the tip comes closer to the surface, the tip and the sample are deformed and can be better described by Hertzian contact theory. In the range $z < -1\,\mathrm{nm}$ the curve is linear and represents a contact stiffness of $\approx 50\,\mathrm{N/m}$. This is comparable to measurements on such a material system reported in the literature [96]. The length scale of the interaction is probably modified because of additional electrostatic forces and deformation of the tip and sample. Experimental measurements by Rychen *et al* show similar behaviour [87].

Recovering the damping coefficient

An expression for the drive force F_0 in terms of the 'odd' component of F_{ts} can be found in the same way as Eqn. 6.13 [93]:

$$F_0 + 2\pi abf_0 = \frac{2}{T}\int_0^T F_{odd}(q(t)) \sin 2\pi f_0 t \, \mathrm{d}t \tag{6.17}$$

F_{odd} depends on the tip-sample separation and the tip velocity and therefore cannot be recovered directly using the mathematical method discussed in Section 6.3.1. This problem can be overcome by expressing F_{odd} as the product of the tip velocity $\dot{q'}(t)$ and a 'generalized damping coefficient' $\Gamma(a, f_0, q'(t)) = \gamma + \Delta\Gamma$ which is a unique function of tip-sample position, where γ is the damping coefficient a long way from the surface. This can be calculated from the quality factor Q, mass m and resonant frequency f_0 of the tuning fork and is given by [97]:

$$\gamma = \frac{2\pi f_0 m}{Q} \tag{6.18}$$

F_{odd} is then given by [89]:

$$F_{odd} = \Gamma(z, a, f_0, q'(t))\dot{q'}(t) \tag{6.19}$$

With F_{odd} substituted for the definition above, Eqn. 6.17 can be transformed into the same form as Eqn. 6.9 by partial integration and substitution. Comparing coefficients then $\Theta(z) \equiv \frac{\Delta F_0(z)}{F_0} - \frac{\Delta f(z)}{f_0}$, $B(z) = 2\int_z^\infty \Delta\Gamma(z')\,dz'$ and $b = \gamma$. Substituting these coefficients into Eqn. 6.10 gives:

$$\Delta\Gamma(z) \qquad = -\gamma\frac{\partial}{\partial z}\int_z^\infty \left(1 + \frac{a^{\frac{1}{2}}}{8\sqrt{\pi(z'-z)}}\right)\Theta(z')$$

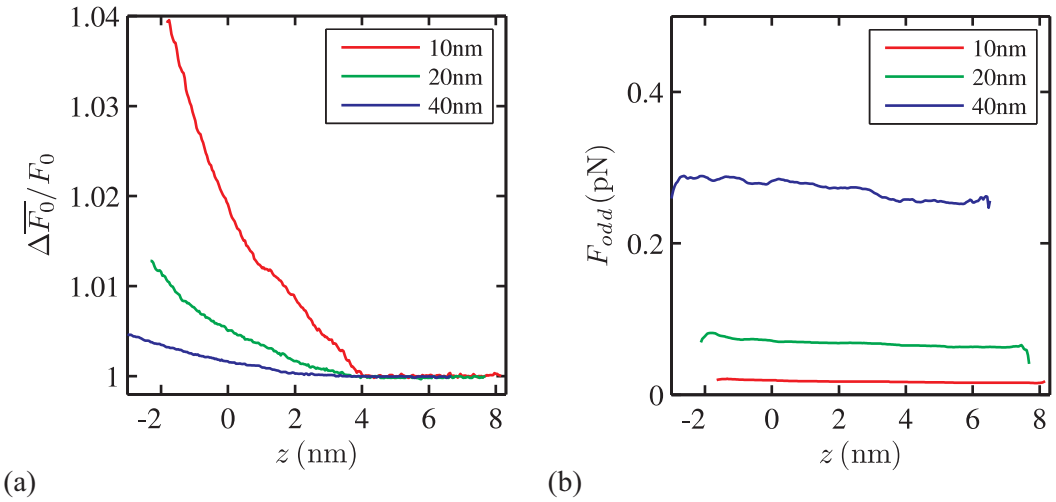

Figure 6.5: (a) Drive required to maintain constant amplitude versus tip-sample separation for different amplitudes. (b) Recovered F_{odd}.

$$-\frac{a^{\frac{3}{2}}}{\sqrt{2(z'-z)}}\frac{\mathrm{d}\Theta(z')}{\mathrm{d}z'}\,\mathrm{d}z' \tag{6.20}$$

Figure 6.5(a) shows the change in the drive force as a function of oscillation amplitude, these measurements are discussed in detail in Section 6.2.1. Using the analysis outlined above the odd force F_{odd} has been reconstructed from the experimental data shown in Fig. 6.5(a) and is plotted in Fig. 6.5(b).

The odd force curves have a large background which increases with oscillation amplitude. The change in F_{odd} with tip-sample separation is much smaller. F_{odd} increases linearly with decreasing z with a gradient less than 5 fN/nm. The odd forces are very small compared to F_{even} with, $F_{even} \approx 10^5.F_{odd}$.

The odd force consists of a contribution from internal damping of the probe and from the tip-sample interaction. The internal damping of the probe is much larger. The increase in F_{odd} with oscillation amplitude is expected from Eqn. 6.19.

6.3.3 Tip-sample capacitance

The capacitance measurement technique has been outlined in Chapter 5. In the case of the gold sample then it has been shown that the quadrature signal, Y, is governed by

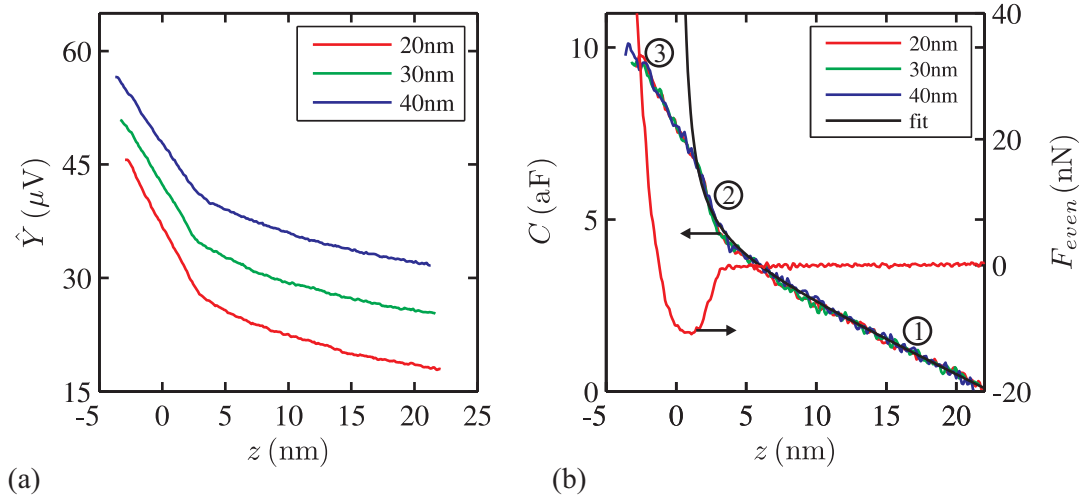

Figure 6.6: (a) $\hat{Y}$ versus tip-sample separation for different oscillation amplitudes. (b) Recovered C versus tip-sample separation z for different oscillation amplitudes and fit of analytical expression.

changes in the tip-sample capacitance. The component at the TF oscillation frequency, $\hat{Y}$, is given by the Fourier component of Y measured by the lock-in amplifier:

$$\hat{Y} = K_g \frac{1}{T} \int_0^T \Delta C_{ts}(z + a + q'(t)) \cos 2\pi f_0 t \, dt \tag{6.21}$$

By substituting $u = \frac{q'(t)}{a}$ and rearranging this can expressed in the same form as Eqn. 6.9 with $\Theta(z) \equiv \hat{Y}(z)$, $B(z) \equiv \Delta C_{ts}(z)$ and $b \equiv \frac{1}{K_g a}$.

Figure 6.6(a) shows $\hat{Y}(z)$ obtained in the experiment. The reconstructed $C(z)$ curves are shown in Figure 6.6(b). The $F_{even}(z)$ curve has been plotted on the same axes for orientation. The capacitance curve shows three regimes: a linear slope for separations $z > 5\,\text{nm}$ (Label 1); for $5 > z > 2\,\text{nm}$ the gradient increases quickly (Label 2); and at about 2 nm there is a distinct change in the gradient and the capacitance increases linearly with decreasing separation. The distinct change at 2 nm corresponds to the onset of the repulsive regime in the force curves and probably indicates the point at which the tip begins to interact with the surface.

The capacitance curve has been fitted to the first terms of a McLaurin/Taylor

expansion:

$$C = \frac{A}{z - z_0} + B(z - z_0) + C_0 \tag{6.22}$$

The first parameter can be interpreted as the local part of the tip-sample capacitance, which changes with $1/z$ for small separations. This is the same as for a parallel plate capacitor. The second term represents the main contribution from the macroscopic part of the tip. The third term accounts for the constant stray capacitance which does not change with tip-sample separation. This expression has been fitted to $z > 2\,\text{nm}$ of the recovered capacitance curves and is shown by the black line in Figure 6.6(b).

The effect of the surface contact force was modelled as a distortion of the motion of the tip. This might be a distortion of the motion of the tuning fork but more likely is some deformation of the tip at the surface. The deconvolution routine assumes harmonic motion for the tip and distortion of this motion will create artefacts in the recovered force and capacitance curves. The effect of distortion has been modelled by generating data from the analytical expression for C (Eqn. 6.22) with a distorted tip-motion. Three types of distortion were modelled:

- A linear reduction in the displacement below a certain threshold.
- A threshold at which the displacement is clipped.
- A combination where below the first threshold the displacement is reduced linearly and at the second threshold the displacement is clipped.

Figure 6.7(a) shows the displacement of the tip with and without distortion and Figure 6.7(b) shows the recovered capacitance curves in each case.

This simple distortion model is reasonably successful in reproducing the anomalous behaviour seen in the $C(z)$ curve at small separations. There is good reason to support the assumption that the tip/sample is being distorted from the linear slope seen in the recovered $F_{even}(z)$. An alternative explanation that was explored is that the tip motion is harmonic and the change in behaviour at small separations is due to the tip-sample capacitance shorting out when the tip is in contact with the surface. Simple modelling

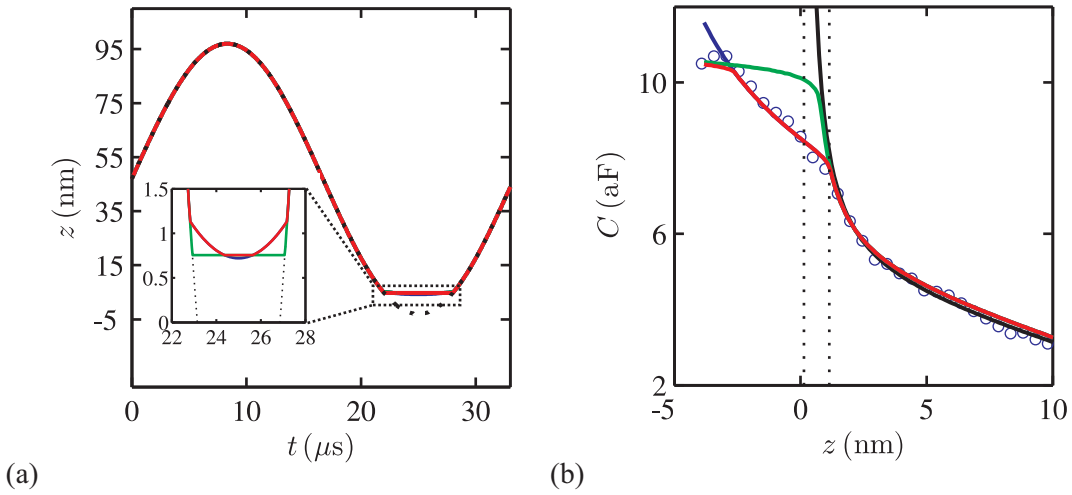

Figure 6.7: (a) Displacement of the tip over one cycle close to the surface. Black curve shows harmonic motion, inset shows different distortion models applied to tip motion. Blue - linear reduction in displacement. Green - hard cut off in displacement. Red - combination of a linear reduction and a cut off. (b) Recovered capacitance curves from deconvolution scheme using data simulated with analytical capacitance curve (Black) and distortion models. Colour of the lines has same meaning as (a).

with the equivalent circuit of the tuned filter was not able to reproduce the features seen in the data. It might be that the oxide layer on the tip prevents the tip shorting to the film.

6.4 Scanning measurements

Figure 6.8 shows a series of images from a scan of the evaporated gold film showing the topography z, frequency shift Δf, tuning fork drive voltage U_{exc} and $\hat{Y}$ signals. An image showing $\hat{X}$ has not been included because no structure in the signal could be observed. The $\hat{Y}$ image was scaled in terms of capacitance by multiplying by the constant K_g as discussed in Section 6.1.1.

The topographic image, Figure 6.8(a), shows gold clusters on the surface with a lateral size of 50-100 nm and a height of 5-10 nm. The frequency set point was 0.5 Hz, deviations of ± 0.5 Hz can be seen in the error signal image, Figure 6.8(b). These deviations are a large proportion of the set point and indicate that the AFM control was not performing well during these images. The frequency error signal has pronounced dips at positions corresponding with the right edge of topographic features. This indicates where the AFM control system is briefly losing contact with the surface. The variation in the drive voltage is approximately 5 %, regions of reduced drive voltage correspond to raised features in the topography. The capacitance signal doesn't show any significant structure, the small features that can be seen are about the right size and shape to indicate a correlation with topographic features. The variation in the capacitance signal is a large proportion of the signal, this might be due to the poor AFM control. These data are quite difficult to analyze because of the poor AFM control. Future suggestions for scanning measurments include: a flat conducting sample such as highly orientated pyrolytic graphite (HOPG) to assess the stability of the $\hat{Y}$ signal during scanning. A sample with well defined topographic features could be used to analyse the geometric effect of the topography on the capacitance signal.

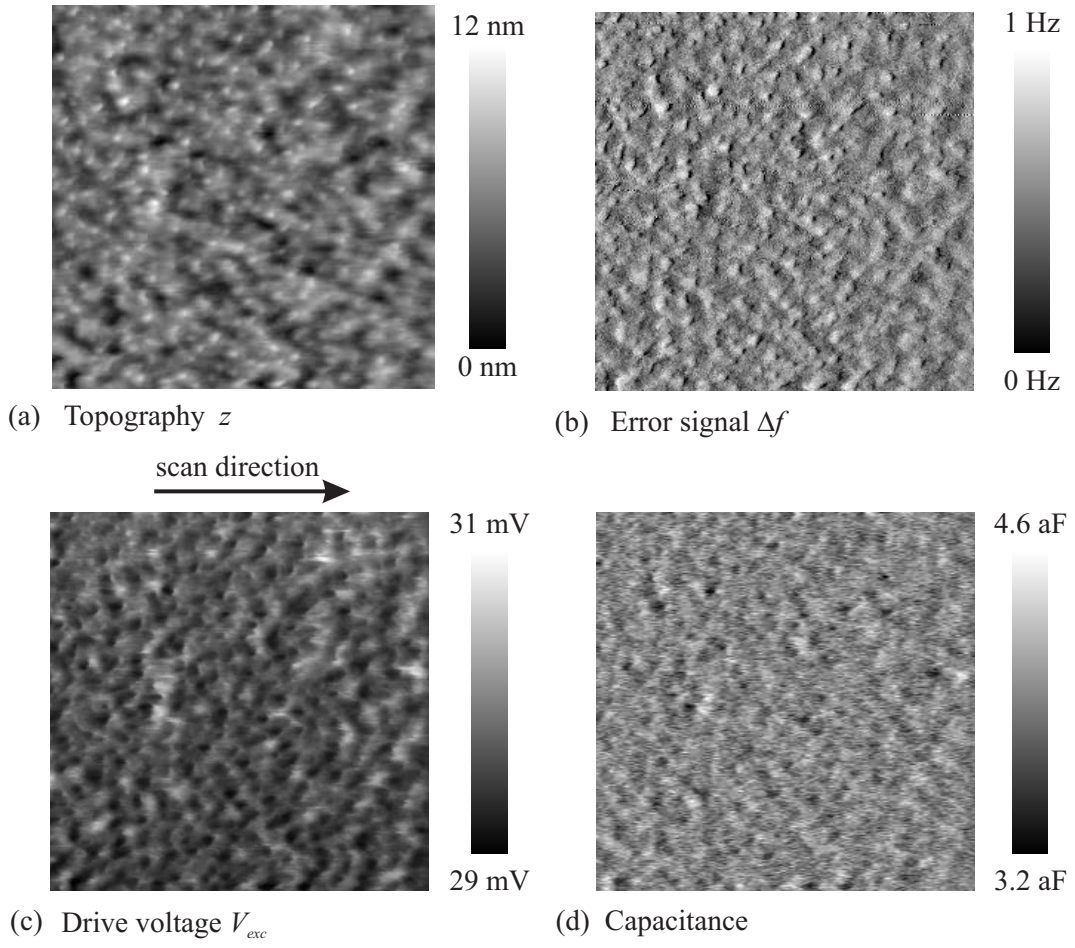

Figure 6.8: $1.5 \times 1.5\,\mu$m scan of a thin gold film at room temperature in vacuum. (a) Topography z. (b) Error signal Δf. (c) Tuning fork drive voltage U_{exc}. (d) Capacitance signal $\hat{Y}$. Scan rate 0.25 Hz, frequency setpoint 0.5 Hz.

6.5 Summary

Measurements have been made over an evaporated gold film. The tip-sample interaction was modelled by a capacitance and the sample by a resistive plate. Using the equivalent circuit model of the tuned filter it was shown that the response of $\hat{Y}$ was proportional to the tip-sample capacitance.

A deconvolution scheme was used to recover the tip-sample force and tip-sample capacitance from the measured quantities. The tip-sample force was larger and over a longer length scale than theoretical predictions. The increased length scale was attributed to additional electrostatic forces and a deformation of the tip and sample at the closest separations.

In the next chapter measurements of a 2DEG sample are discussed.

Chapter 7

Measurements of a 2DEG

7.1 Introduction

This chapter begins with a discussion of SPM measurements of 2DEGs in the literature and the key results. Point spectra measurements over the bulk region of a 2DEG are presented and used in conjunction with a simple model to try to understand how the capacitance measurements relate to the local properties of the 2DEG. Scanning measurements at an edge are presented and show that the technique is sensitive to the presence of a 2DEG. In conjunction with finite element simulations the geometric effect of the edge on the signal is considered. The final sections present scanning measurements at the edge of the 2DEG as a function of magnetic field and current.

7.2 SPM measurements of 2DEGs

Scanning probe techniques are typically used for microscopic studies of surface phenomena. The electrons in a 2DEG are buried tens of nanometres below the surface and as such present a challenge for SPM studies. Studies of the quantum Hall effect require temperatures below a few kelvin and magnetic fields of a few tesla. This environment introduces many technical challenges to the design of the microscope. These difficulties mean that only a handful of groups have been successful in demonstrating

SPM measurements of the quantum Hall effect.

The SPM techniques which have applied to this area vary in their approach but all rely on measuring or modifying the electric field between the 2DEG and a metallic tip. Scanning single electron transistor (SSET) [58] and Kelvin probe measurements [98] have measured the local potential above the 2DEG. Scanning gate measurements use a voltage applied to the metallic tip to locally perturb a region of the 2DEG [99]. Scanning charge accumulation microscopy [100] uses a sensitive charge detector to measure how easily charge can flow in and out of a region of a 2DEG, this depends upon the local compressibility and conductivity of the 2DEG. In the following sections these techniques and the key results from studies of the quantum Hall effect will be discussed.

Later in this chapter scanning capacitance microscopy is presented as a new technique for local studies of a 2DEG in the quantum Hall regime.

7.2.1 Scanning SET measurements

In scanning single electron transistor (SSET) experiments the static electric field above the 2DEG is measured with a single electron transistor (SET) fabricated on the end of a fine glass probe.

An SET is a sub-micrometre tunnelling device where the current passing between source and drain electrodes is governed by the Coulomb blockade effect of a small metal island. The island is connected to the source and drain by two tunnel junctions where the tunnelling rate is determined by the electrostatic potential of the island with respect to the source and drain. By measuring the current flow through the transistor it is possible to detect changes in the electric potential.

A scanning SET was first demonstrated by M.J.Yoo *et al* by fabricating an SET on the end of a sharp glass fibre [58]. This design has been used for an investigation of a GaAs/AlGaAs heterostructure with a 2DEG 100 nm below the surface. The scanning SET was operated as part of a feedback loop keeping the current through the SET constant by adjusting the potential between the sensor and the 2DEG with a bias

voltage applied to the 2DEG. Two main types of measurement of the 2DEG are made with this type of instrument. These are the 'transparency' of the 2DEG to an electric field from a back gate, which probes the compressibility of the electron gas, and the Hall voltage induced by transport current. There are large stray background potentials at the surface originating from fluctuating surface dopant charges and metal gates used to define the spatial extent of the 2DEG. In order to separate the small transparency or transport signals from the background, low frequency lock-in amplifier techniques were used.

In the transparency measurements the voltage between the SET and the backgate was modulated. The modulated voltage is screened by the 2DEG and the strength of this screening depends upon the local filling factor. Figure 7.1 shows SET images of a 2DEG in the vicinity of metal gates fabricated on the sample surface. The 2DEG underneath the gates is depleted by the work function difference between the gates and the GaAs. Figure 7.1(a) shows the local potential between the gates. The transparency image, Fig. 7.1(b), shows compressible and incompressible phases of the 2DEG. The regions of high signal are incompressible areas of 2DEG surrounded by compressible regions. The bright stripe between the gates is identified as the incompressible stripe that lies along the $\nu = 1$ edge states. The bright regions at the edge of the gate are artefacts of the imaging technique.

Measurements of the Hall voltage have also been made by passing a low frequency AC current through the 2DEG. At low magnetic fields the Hall voltage was found to drop linearly across the sample in agreement with the classical prediction. In the quantum Hall regime the voltage drop is concentrated at the edges suggesting this is where most of the current flows. It was not possible to measure the voltage drop right up to the edge because of the screening effect of the metallic top gates.

The advantage of this technique is that it is able to measure the local potential or local screening properties with a very high resolution. The probes are very difficult to fabricate and compensating the background potential close to an edge makes imaging real devices difficult.

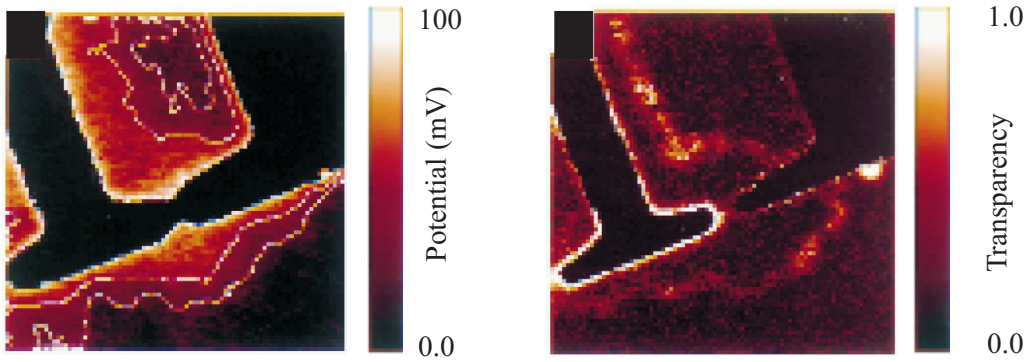

Figure 7.1: $15 \times 15\,\mu$m SET images taken close to metallic gates fabricated on the sample surface at filling factor $\nu = 1$. (a) The local potential between the gates. (b) Transparency to a back gate showing an edge state following the local potential. Images taken from Ref. [101].

7.2.2 Kelvin Probe microscopy

Measurements have been made on a 2DEG in the quantum Hall regime by McCormick *et al* [98]. A particular aim of the experiments has been to image the Hall potential as a function of distance from the edge of a Hall bar. The 2DEG was located in a GaAs/AlGaAs heterostructure 77 nm below the surface. A gold coated piezo resistive cantilever was used as the sensor and had a resonant frequency of ≈ 120 kHz. The Hall potential was measured as a function of magnetic field by applying a small AC current to the sample and measuring the force on the probe at this frequency. The tip-sample capacitance and induced charge influence the spatial dependence of the measured force. To compensate, reference measurements were taken before applying a current and were used to normalize the measurements with an applied current.

Figure 7.2 shows a line scan of the potential across a Hall bar as a function of magnetic field taken from Ref. [102]. Away from integer filling the Hall potential profile shows a linear drop across the sample. Close to integer filling the potential drops arbitrarily in the bulk of the sample, just above integer filling factors the potential becomes flat in the bulk and all the potential drop occurs at the edges [103]. This behaviour is periodic with filling factor and can be related to the model of compressible

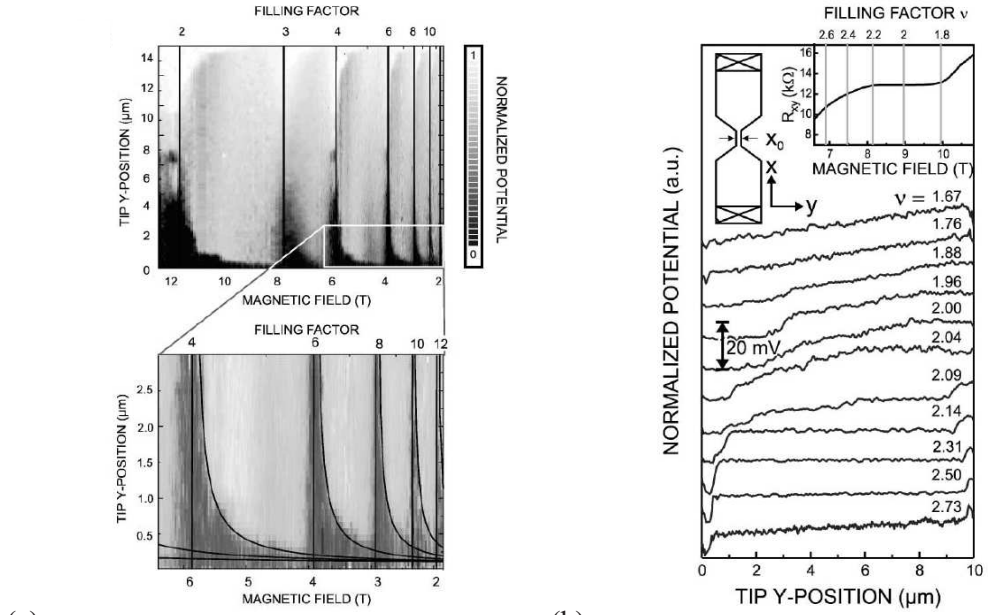

Figure 7.2: (a) Normalized Hall potential profile versus magnetic field. Lines on lower graph indicate the position of the innermost incompressible stripe from the model of Chklovskii *et al* [27]. (b) Normalized Hall potential profile for different magnetic fields around filling factor $\nu = 2$. Sample geometry and transport data are shown in the inset. Images taken from Ref. [102].

and incompressible regions [27]. The potential drop has been successfully fitted to the position of the innermost compressible stripe [102]. The Hall potential distribution has also been investigated near a contact and it was concluded that the bulk is strongly decoupled from the edges and ohmic contacts slightly above integer filling factors [104]. The relatively high frequencies used by this technique may reduce the sensitivity in regions where the conductivity is low, such as the bulk of the sample at integer filling factors. In the measurements made in this thesis it is quite common to see areas of the image which behave differently from the rest of the image. It is difficult to judge how representative of the sample the line scans presented in Fig. 7.2 are as there are no whole scans published in the literature.

The advantages of this technique are that it can be performed with a standard AFM

and the measurement is easy to interpret. The disadvantage is that measurements are very slow. This is evident in the literature where only line scans have been presented.

7.2.3 Sub-surface charge accumulation

Sub-surface charge accumulation (SCA) measures the local charge accumulation of a 2DEG in response to small AC excitation. This technique has been used to image nanometre-scale structures in the quantum Hall regime [100, 105–108].

A sharp metallic tip is scanned a short distance from the sample surface ($\approx 5\,\mathrm{nm}$) and is connected to a sensitive charge detector. An AC voltage with a frequency of about 100 kHz and an amplitude of a few mV is applied directly to the 2DEG via an ohmic contact. The applied voltage causes charge flow in and out of the 2DEG, capacitive coupling in turn induces charge on to the tip. The charge is measured with a high electron mobility transistor. A simple bridge circuit compensates the huge background signal, originating from stray capacitances [109]. A sensitivity of 0.01 electrons $/\sqrt{Hz}$ has been demonstrated [109]. Lock-in detection at the excitation frequency is used to recover the in-phase and quadrature components of the charging signal.

Contrast in the images arises from spatial variation in the compressibility or conductivity of the 2DEG. In the quantum Hall regime, structure on a length scale of 100 nm has been observed. Some of this can be explained using the ideas of compressible and incompressible stripes [100, 105, 107]. A number of models for these experiments have been discussed in Ref. [110]. The lateral resolution has been estimated to be $\approx 90\,\mathrm{nm}$ using numerical simulations of the tip-sample capacitance for a 2DEG buried 100 nm below the surface [111].

Figure 7.3 shows an SCA image close to a gate fabricated on the surface of a sample. An AC signal was applied to the gate and the 2DEG, the charge accumulation on the tip was then measured. Although no DC bias was applied to the gate, the work function difference is enough to deplete the 2DEG by $\approx 15\,\%$ under the gate. In the absence of a magnetic field the conductivity of the 2DEG is high and uniform. The tip charges

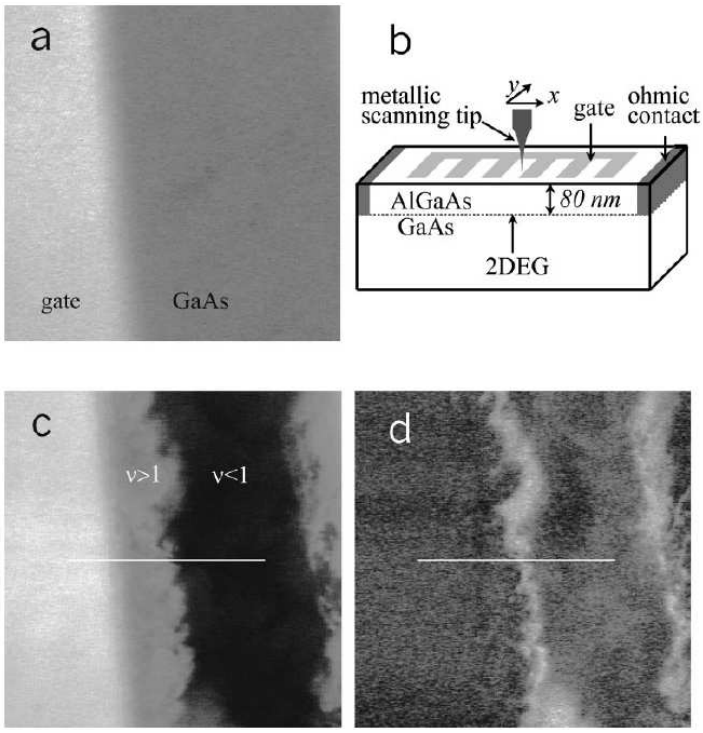

Figure 7.3: $12 \times 12\,\mu$m SCA images. (a) 0 T in-phase signal. (c) 6.4 T in-phase signal. (d) 6.4 T quadrature signal. (b) Sample schematic. Incompressible stripes at $\nu = 1$ form close to the edge of the gate and separate regions of $\nu < 1$ from regions of $\nu > 1$. Figure taken from Ref. [108].

uniformly in-phase with the excitation signal and this is seen in Fig. 7.3(a). The bright region to the left is the gate where the capacitance is higher as it is on the surface compared to the 2DEG which is buried beneath the surface. In the vicinity of integer filling factors the charge flowing from the gates only partially penetrates the 2DEG, Fig. 7.3(c). At the boundary between the edge state and the bulk region there is a peak in the out-of-phase charging signal. From these measurements Glicofridis *et al* were able to estimate the resisitivity of an incompressible stripe as $\approx 10\,\mathrm{M}\Omega/\mu\mathrm{m}$.

This technique has been applied in a different way to map out the local potential in the quantum Hall regime. By applying a positive voltage to the tip and at suitable filling factors, a 'bubble' of electrons is accumulated underneath the tip. This contains a small number of electrons and is isolated from the rest of the 2DEG by a circular incompressible stripe. By measuring the charge entering or leaving this 'bubble' as the tip is scanned over the surface it is possible to map out the local potential in the Hall liquid [106]. These experiments found that random potential fluctuations had a length scale of $\approx 0.5\,\mu\mathrm{m}$ and that this potential remained fairly unchanged between different quantum Hall plateaus.

There are a number of limitations of this technique. For instance, there are no examples in the literature where images have been taken close to an edge of a real device and no measurements where a current is passed through the sample. It might be that the potential variations close to the edge or due to the Hall voltage would make it difficult to make measurements without saturating the charge measurement device.

7.2.4 Scanning Gate

In scanning gate experiments macroscopic measurements of a system, typically conductance, are made whilst scanning a conductive AFM tip across the surface. By applying a bias between the tip and the sample it is possible to modify the local potential of the system. Scanning gate images are formed from the measured quantity as a function of the tip position.

Scanning gate experiments have been used to image coherent electron flow around

a quantum point contact (QPC) [112–116]. The tip creates a small depleted region in the 2DEG that can backscatter electron waves. When the tip is over an area of high electron flow the conductance through the QPC is decreased whereas when the tip is over an area of low electron flow the conductance is unmodified.

Close to the QPC it has been possible to image the angular pattern associated with individual modes of the QPC [114]. Further away the electron flow forms narrow branching strands that follow channels in the local background potential [113]. A review of these coherent flow experiments can be found in Ref. [116].

Three scanning gate experiments have been reported in the quantum Hall regime. In the first, the scattering between edge channels was investigated on a Hall bar [99]. Metal gates fabricated on the top of the Hall bar were used to establish and detect the edge state populations. The scanning gate measurements showed regions of the sample close to the edge where the tip was able to enhance the longitudinal resistance and these were interpreted as local scattering centres. A similar experiment investigated scattering between edge channels using a more complicated sample geometry, the scanning gate images show fringes which suggest that phase coherence may be important in edge state coupling [117]. In the most recent experiment the Hall resistance of a Hall bar was measured as a function of tip position and magnetic field [118]. Local features of the resistance images resembled $1/B$ periodicity of the transport data. Features in the images corresponded to formation of extended edge states and localized bulk states.

Figure 7.4 shows some examples of scanning gate images of a Hall bar in the quantum Hall regime. The images show the Hall resistance as a function of the tip position. The black contours indicate the edges of the Hall bar. The work function difference of the tip and sample means that the tip was at a voltage of 0.3 V with respect to the 2DEG. The patterns of the tip-induced resistance changes are strongly dependent on filling factor. At integer filling factors the Hall resistance is not influenced by the position of the tip. Away from integer filling factors tip-induced changes are very localized, mainly close to the edges and $1/B$ periodic. These features are interpreted as 'hot spots' in the local potential where a small change in the local potential can change

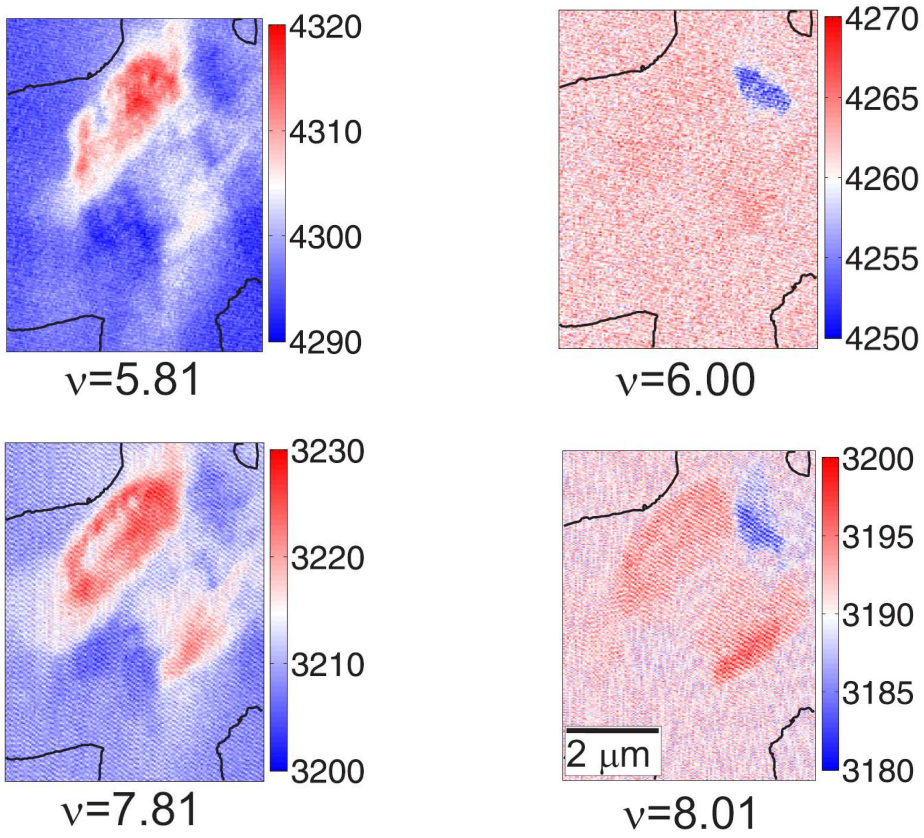

Figure 7.4: Scanning gate images showing the Hall resistance as a function of the tip position for different filling factors. Images taken from Ref. [119].

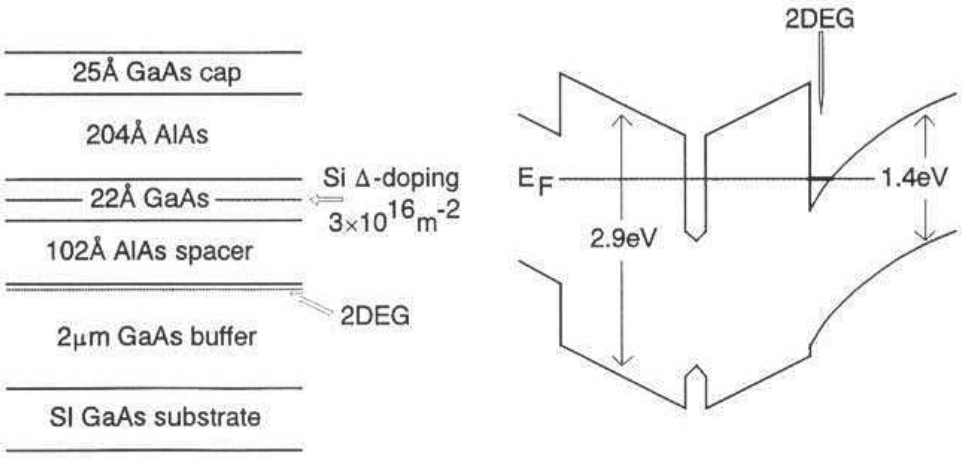

Figure 7.5: Cross section of the heterostructure and the band diagram of wafer NU1793. Figure taken from Ref. [120].

dramatically the percolation of extended states between the two edges. These images can be used to extract real space information about the local potential landscape in real devices.

The disadvantage of these measurements is that they are difficult to interpret. They do not measure a local property of the system but the response of some macroscopic quantity to a local perturbation.

7.3 Sample description

Experiments were performed on a GaAs/GaAlAs heterostructure sample [1] with a 2DEG located 50 nm below the surface. A cross section of the heterostructure and the band diagram are shown in Fig. 7.5. Remote doping was achieved by a δ-doping layer placed in a quantum well. This unusual design helps to avoid parallel conduction channels and reduces the distance between the 2DEG and the surface [120].

Large Hall devices, ($L, W >>$ mean free path), were fabricated by photolithography and wet chemical etching. The active area has a length $L = 2.4\,\mathrm{mm}$ and a width

[1] wafer number NU1793

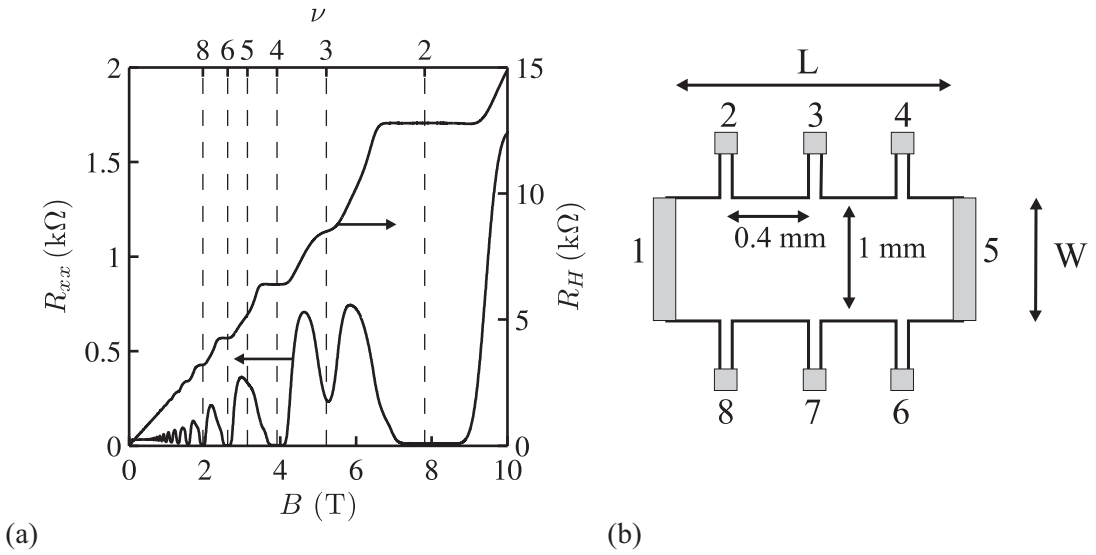

Figure 7.6: (a) Magnetoresistance data measured at 1.8 K. (b) Schematic of the sample geometry.

$W = 1\,\text{mm}$, see Fig. 7.6(b). Figure 7.6(a) shows magnetoresistance data of this sample measured at 1.7 K. Minima in R_{xx} and plateaus in R_H are seen at even integer filling factors and at filling factor $\nu = 3$. Filling factor $\nu = 1$ at $B \approx 16\,\text{T}$ is above the maximum field of the magnet. The electron sheet density was determined from the classical Hall slope as $n_s = 3.8 \times 10^{15}\,\text{m}^{-2}$, and the Shubnikov-de Haas oscillations as $n_s = 3.7 \times 10^{15}\,\text{m}^{-2}$. A mobility of $\mu = 45\,\text{m}^2\text{V}^{-1}\text{s}^{-1}$ was calculated from the zero-field longitudinal conductivity which gives a zero-field mean free path of $4.5\,\mu\text{m}$.

7.4 Point spectroscopy

The aim of this section is to use point spectroscopy measurements in the bulk of the 2DEG and some simple modelling to construct an argument which allows straightforward interpretation of the data. This section starts with a discussion of the experimental data before introducing a simple model of the tip-sample interaction. This model is used to simulate the point spectroscopy measurements and these simulations are compared with the data. With the model it is possible to demonstrate that changes in the

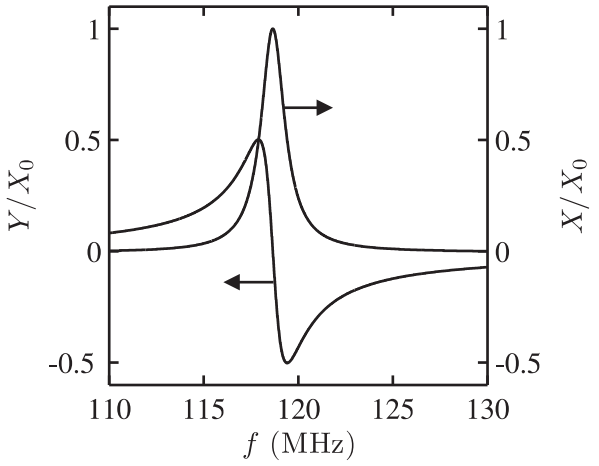

Figure 7.7: Response of the tuned filter as a function of frequency f.

measured quantities are dominated by the local conductivity, σ_{xx}, of the sample.

7.4.1 Point spectra experiments

Capacitance measurements were made as a function of magnetic field over the bulk region of the sample, with a distance to the nearest edge larger than 200 μm. Before presenting the data there is a brief summary of the technical details of the capacitance measurements.

The capacitance measurements are based on the transmission of the RF signal through the tuned filter. Figure 7.7 shows the transmission of the tuned filter as a function of frequency. Measurements are made at a fixed frequency close to the resonance of the tuned filter. Changes in the sample properties modify the resonance frequency and amplitude of the tuned filter response. At a fixed frequency, close to resonance, and for small changes in the filter response, the in-phase component X of the transmission is proportional to the amplitude of the filter response. The quadrature component Y is proportional to the shift in resonance frequency. Changes in the resonance frequency are brought about by a change in the imaginary or reactive part of the sample impedance and changes in the amplitude by a change in the real or resistive part of the sample impedance. Figure 5.1 is a schematic showing an overview of the

capacitance detection. The instrumentation design means that the measured quantities scale linearly with the amplitude of the signal from the tuned filter. In this chapter the majority of the measurements have been normalized to the amplitude of the tuned filter on resonance at zero-field X_0. This normalization makes it possible to compare different measurements with slightly different drive voltages. The X and Y quantities are typically of the order mV and the $\hat{X}$ and $\hat{Y}$ quantities a few tens of μV.

X and Y point spectra

The RF lock-in amplifier was used to measure the in-phase, X, and quadrature components of the signal, Y, as a function of magnetic field. Before making the measurement, the AFM control was used to locate the surface of the sample. The control loop and tip oscillation were switched off to leave the tip 50 nm above the surface. The measurement time was limited by the ramp rate of the magnet taking approximately 20 minutes to record a sweep of 0-10 T.

The reason for making point spectra measurements with no tip oscillation is that they are easier to simulate with the model discussed in the next section.

Fig. 7.8(a) shows the quadrature component, Y, of the RF signal as a function of filling factor. There are peaks at even integer filling factors which can be resolved up until $\nu = 30$. A peak can be seen at $\nu = 3$ and a small feature at filling factor $\nu = 5$. The even integer peaks increase in magnitude with decreasing filling factor, $\nu = 4$ is an exception which is smaller and has a split top. There is a background which decreases sharply at low filling factors before flattening out. The total change in Y is approximately 20 % of the magnitude of the RF signal. The low field peaks were used to estimate the sheet density giving $n_s = 3.7 \times 10^{15}\,\mathrm{m}^{-2}$ which is in agreement with the transport value. Fig. 7.8(b) shows the in-phase component, X, of the RF signal as a function of filling factor. There are strong features corresponding to even integer filling factors. At the highest filling factors (low magnetic fields) there are minima at even filling factors. At low filling factors there are peaks just below even filling factors. The transition between minima and maxima can be seen between $\nu = 16$ and $\nu = 12$.

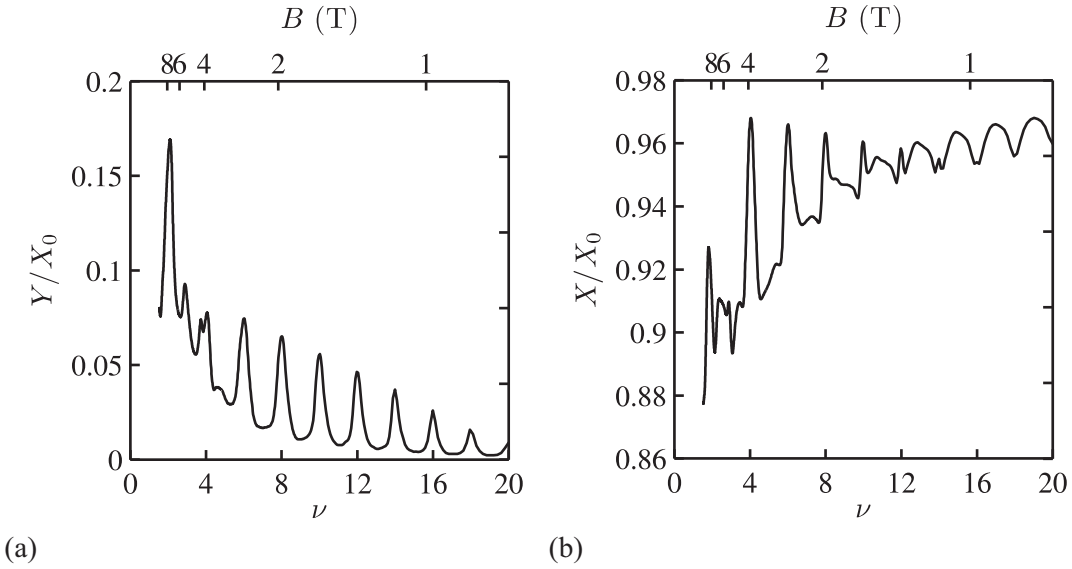

Figure 7.8: (a) Quadrature, Y, and (b) in-phase, X, components of the RF signal over the bulk of the 2DEG as a function of filling factor.

The features increase in size with decreasing filling factor, the dip around $\nu = 18$ is approximately 1.5 % of the signal magnitude whilst the peak at $\nu = 2$ is about three times larger.

$\hat{X}$ and $\hat{Y}$ point spectra

When imaging, the tip-sample distance z is modulated by the tuning fork oscillation of a few tens of nanometres. This modulates the tip-sample capacitance resulting in modulations of the quadrature and in-phase RF signals, $\hat{Y}$ and $\hat{X}$ respectively. Figure 7.9 shows the measured $\hat{Y}$ versus magnetic field with an oscillation amplitude of 50 nm. A constant background of 15 μV (approximately 20 % of the maximum signal level or 1×10^{-3} in the normalised units) has been subtracted. This is the signal level seen over an etched region of the structure (no 2DEG) and is due to the finite dielectric constant of GaAs. Strong minima are seen in the signal at integer filling factors, the minima become deeper and wider with decreasing filling factor. Away from integer filling factors there is a decreasing background with increasing field, which is due to

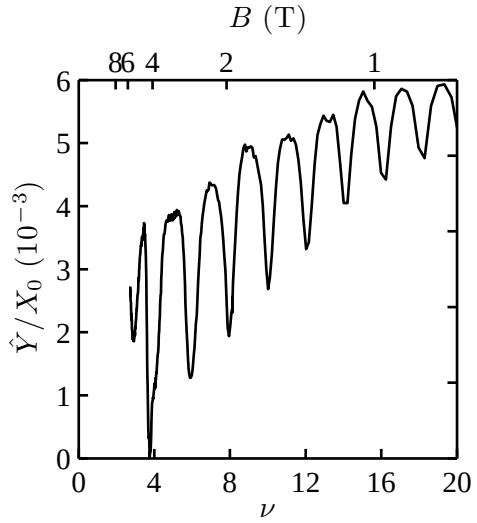

Figure 7.9: $\hat{Y}$ versus filling factor with an oscillation amplitude of 50 nm.

the falling longitudinal conductivity of the sample.

Problems with the set-up meant that the phase of the reference used to recover the in-phase part of the signal was set incorrectly which means the recorded $\hat{X}$ was a mixture of $\hat{X}$ and $\hat{Y}$. These problems with the set-up have now been resolved but most of the $\hat{X}$ measurements need to be repeated in the future.

7.4.2 Modelling

A simple model of the tip and sample is used in conjunction with the equivalent circuit description of the tuned filter to investigate the response of the RF resonator. The assumptions made in this model are:

- The tip-sample interaction can be described by a series RC equivalent circuit
- The tip couples capacitively into a small area of the 2DEG and that this capacitance consists of geometric contributions and contributions from the finite compressibility of the 2DEG.
- The 2DEG is homogeneous and can be represented by a resistive plate.

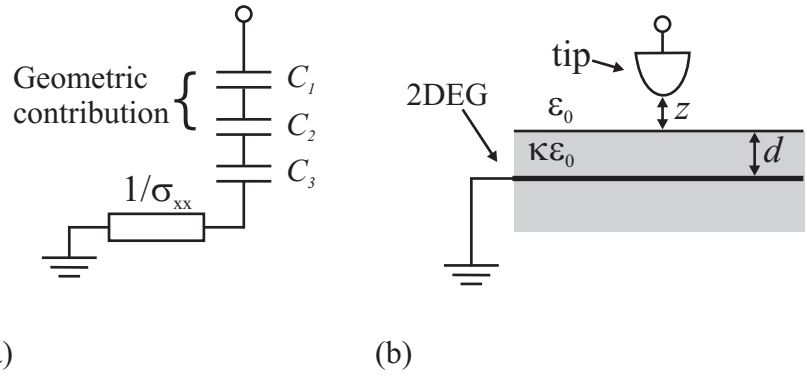

Figure 7.10: (a) Lumped element model used to describe tip-sample system. (b) Schematic of tip and sample.

The tip-sample system is approximated by a series RC lumped element circuit. Figure 7.10(b) shows a schematic of the tip a distance z above the sample and the 2DEG a distance d below the surface. Figure 7.10(a) shows the lumped element model consisting of tip-sample capacitance and a resistance to ground through the sample. The 2DEG is modelled as a resistive plate as in ref. [121] rather than a distributed RC network as in ref. [110] as this is able to reproduce the main features of the data. The tip-sample capacitance, $C_{ts}(D,z)$ (where D is the density of states and z is the tip-sample separation), has geometric contributions and a contribution from the finite compressibility of the 2DEG. This is approximated by three parallel plate capacitors in series each with an effective area $A_e = \pi r_e^2$ and is given by [110]:

$$C_{ts}(D,z) = \left(\frac{1}{C_1} + \frac{1}{C_2} + \frac{1}{C_3}\right)^{-1} \tag{7.1}$$

$$C_{ts}(D,z) = A_e \left(\overbrace{\frac{z}{\epsilon_0} + \frac{d}{\kappa\epsilon_0}}^{\text{geometric}} + \frac{1}{e^2 D}\right)^{-1} \tag{7.2}$$

where C_1 is the capacitance between the tip and the sample surface, C_2 is the capacitance between the sample surface and the 2DEG, C_3 is the capacitance due to the finite compressibility of the 2DEG and κ is the dielectric constant of the semiconductor.

Assuming the tip couples into a small area of the sample radius, r_e, and that the sample can be described by a local conductivity tensor, the resistance $R \propto 1/\sigma_{xx}$ can be calculated in the same way as for the gold measurements using Eqn. 6.1.

Using the model described it can be demonstrated that for variations of R and C_{ts} in the same regime as the experiment then changes in X and Y are dominated by changes in R.

The two properties of the 2DEG which appear in the lumped element model are the density of states D which makes a contribution to the tip-sample capacitance and the conductivity which determines the sample resistance. Ideally these two parameters would be measured experimentally for this particular sample and entered directly into the model. The conductivity can be inferred by transport experiments, whereas this is a formidable task for D. For this reason the theoretical model outlined in Appendix A was used to generate values of σ_{xx} and D of the same order of magnitude as the experiment.

Values for the lumped element components R and C_{ts} were calculated as a function of magnetic field using Eqn. 6.1, and Eqn. 7.2, the tip-sample separation $z = 50\,\text{nm}$ and 2DEG depth $d = 50\,\text{nm}$ were taken from the experiment and the effective radius $r_e = 1\,\mu\text{m}$ was adjusted to reproduce the features of data. The geometric contribution to the capacitance calculated with these parameters is 5 fF which is reasonable. The equivalent circuit model of the tuned filter (Section 5.1.1) was used to calculate the response of the RF signal.

Figure 7.11 shows the calculated quadrature Y and in-phase X components of the RF signal as a function of magnetic field. The green curves are for the full model, where C_{ts} includes the density of states contribution, and the blue curves are a simpler model, where C_{ts} only has the geometric terms and is not a function of magnetic field. The quadrature Y component is dominated by R but not C_{ts}. There is a small deviation between the two curves at non-integer filling factors but this only a few percent. The in-phase curves show X is also dominated by changes in R, however the deviation between the curves is much larger than in Y, particularly in the vicinity of integer

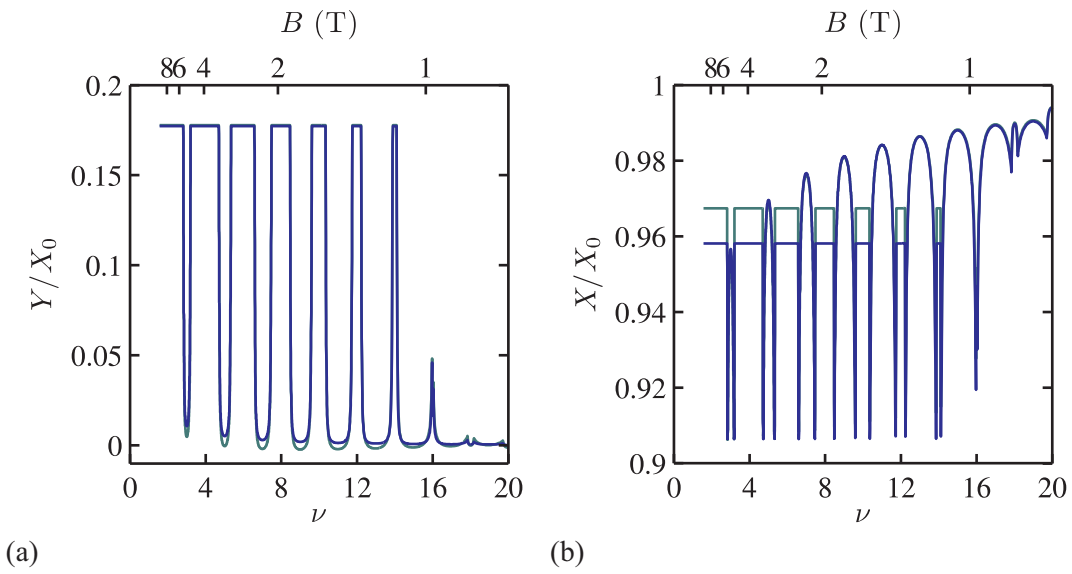

Figure 7.11: (a) Quadrature, Y, and (b) in-phase, X, components of RF signal calculated as a function of magnetic field for the analytical model of the 2DEG sample. Blue curves are for a constant tip-sample capacitance and green curves include a field dependent density of states contribution to the tip-sample capacitance.

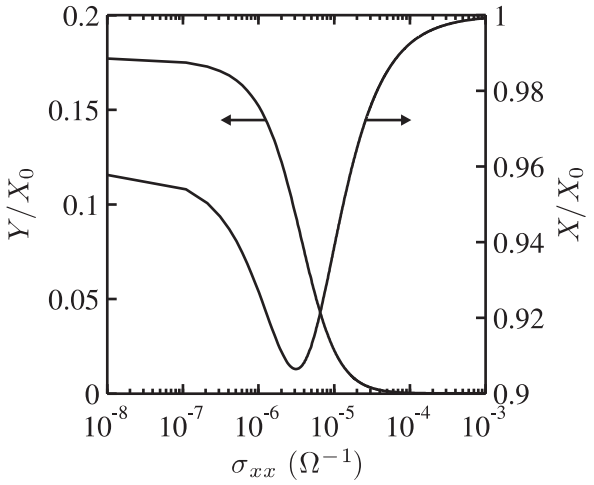

Figure 7.12: Simulated X and Y as a function of sample conductivity σ_{xx}. $C_{ts} = 5\,\mathrm{fF}$.

filling factors.

In summary an RC description of the tip-sample interaction and an analytical model of the 2DEG as a function of magnetic field have been used to demonstrate that, in this simple model, the measured quantities, i.e. the transmission of the tuned filter, are dominated by changes in the local conductivity. Therefore the effect of the density of states on the capacitance sensor will be ignored when comparing the model to the experimental data.

7.4.3 Modelling X and Y point spectra

Figure 7.12 shows the calculated response of X and Y as a function of the sample conductivity σ_{xx}. At high conductivities the tip-sample capacitance is dominant and changes in conductivity have very little influence. At the lowest conductivities the sample has very little influence on the resonator and X and Y are not sensitive to changes in σ_{xx}. In the intermediate regime the sample is changing from a regime where the capacitance is the dominant contribution to the impedance, to a regime where the conductivity is the dominant contribution. This is reflected by a minimum in X which indicates the point at which the dissipation is a maximum and a steep slope in Y

indicating a phase shift in the signal.

If the conclusion of the modelling is correct it should be possible to take the conductivity from magnetotransport data and reproduce the X and Y spectra described in Section 7.4.1

The simulated RF response, with $C_{ts} = 5\,\mathrm{fF}$ and R calculated from transport data (see Fig. 7.10), is shown in Fig. 7.13 alongside the experimental measurements. The only fitting parameter was the effective radius where $r_e = 1\,\mu\mathrm{m}$ was found to reproduce the main features of the data. Values for R vary from $\approx 10\,\mathrm{M\Omega}$ around integer filling factors to $\approx 50\,\mathrm{k\Omega}$ around non-integer filling factors. The quadrature curves (Fig. 7.13(a)) show good agreement, both show peaks at integer filling factors and scaling of the two curves is comparable. The measured curve has an increasing background not reproduced in the simulation. A possible reason could be a contribution from surface charges or donors not included in the simple model, or a variation in the tip-sample separation z with magnetic field.

The in-phase curves also have similar behaviour, at low fields there are minima at integer filling factors whilst at high fields there are maxima at integer filling factors. The relative size and shape of the features and the background is different between the simulation and experiment. The simulations with the analytical model showed that the in-phase component depends on changes in R and C_{ts} so artefacts in the simulated data are expected as no density of states, D, contribution to C_{ts} is included.

7.4.4 Modelling $\hat{Y}$ and $\hat{X}$ measurements

During imaging the tip-sample distance is oscillated by the tuning fork and this modulates the tip-sample capacitance. The components of the in-phase and quadrature signals at this oscillation frequency, $\hat{X}$ and $\hat{Y}$ respectively, are measured with lock-in amplifiers.

The model has been extended to these measurements by making some simple assumptions:

- The only effect of the oscillation is to modulate C_{ts} by a small amount ΔC_{ts}.

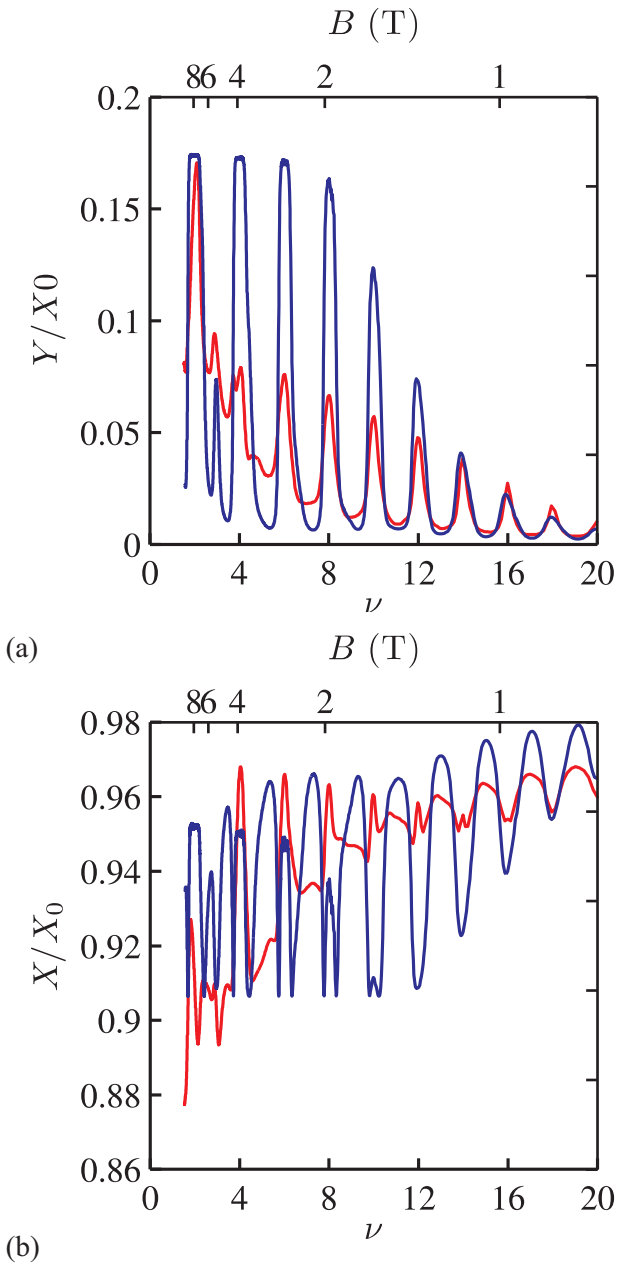

Figure 7.13: Simulated (blue) and experimentally measured (red) curves for the RF response as a function of filling factor ν. (a) Quadrature, Y, and (b) in-phase, X components.

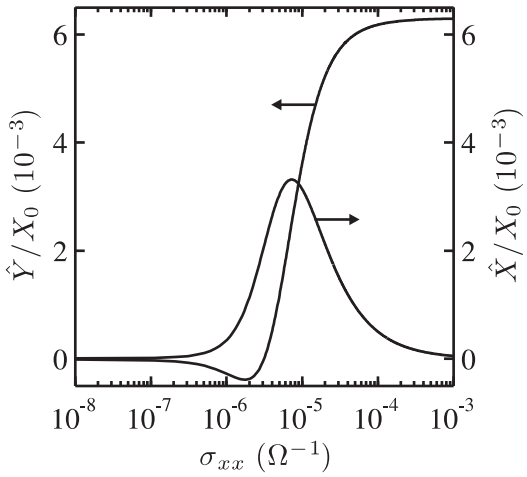

Figure 7.14: Simulated $\hat{X}$ and $\hat{Y}$ as a function of sample conductivity σ_{xx}. $C_{ts} = 5\,\mathrm{fF}$, $\Delta C_{ts} = 6\,\mathrm{aF}$.

- $\hat{Y}$ and $\hat{X}$ are proportional to the size of the capacitance variation ΔC_{ts}.

Figure 7.14 shows the simulated $\hat{X}$ and $\hat{Y}$ versus the sample conductivity. As in the previous section, the density of states contribution to the tip-sample capacitance has been ignored. The curves form is similar to X and Y as a function of conductivity. At the highest and lowest conductivities the measurement is least sensitive to changes in conductivity. In the transition between these two regimes the $\hat{Y}$ signal changes from high signal at high conductivity to low signal at low conductivity at the same time $\hat{X}$ goes through a maximum. There is a small minimum in $\hat{Y}$ around $\sigma_{xx} = 10^{-6}\,\Omega^{-1}$.

Figure 7.15(a) shows the simulated (blue) data for $\hat{Y}$ plotted against the experimental data. The only fitting parameter was the size of the capacitance modulation, where $\Delta C_{ts} = 6\,\mathrm{aF}$ was found to be the optimum value. This is reasonable when compared to the capacitance distance curve measured on the gold sample, Fig. 6.6(b). The simulated data reproduces the main features of the data, deep minima on integer filling factors and a decreasing background for non-integer filling factors. The only field dependent term in this model is the sample resistance which is inversely proportional to the longitudinal conductivity σ_{xx}. Figure 7.15(b) shows the simulated and measured $\hat{Y}$ plotted against the conductivity σ_{xx}. The data agrees reasonably well with the model

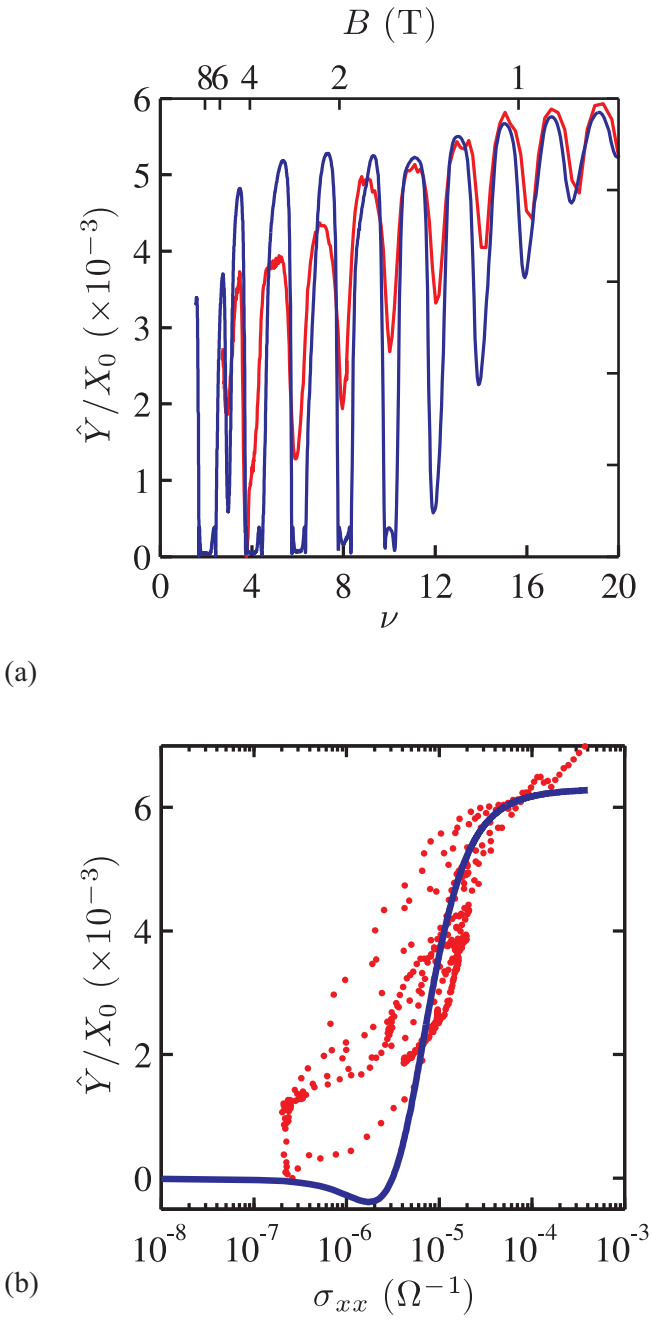

Figure 7.15: Measured (red) and simulated (blue) $\hat{Y}$ (a) versus filling factor ν (b) versus longitudinal conductivity σ_{xx}.

Parameter	Value
Scan size	$4.25\,\mu\text{m} \times 4.25\,\mu\text{m}$
Data points	128×64 pixels
Scan rate	750 nm/s, 12 min/scan
Frequency set point	1 Hz
DC tip bias	-0.3 V
RF signal amplitude	$0.5\,\text{mV}_{rms}$

Table 7.1: Scan parameters.

for $\sigma_{xx} < 1 \times 10^{-4}\,\Omega^{-1}$. At higher conductivities, which occur at the lowest magnetic fields, the difference could be due to the effect of surface charges or donors not included in this simple model. Variations between the data and the model are to be expected as the transport data, which provides the conductivity values, is a bulk measurement whereas the $\hat{Y}$ is a local measurement. Overall, the agreement between the model and the measurement is good enough to support the interpretation of the $\hat{Y}$ measurement in terms of local conductivity.

7.5 Scanning measurements at zero-field

Images of the edge of the 2DEG were taken at zero-field; by understanding the features in these scans it is then possible to identify changes due to an applied magnetic field. AFM and SCM measurements are made simultaneously and the imaging parameters for all the scans in this chapter are given in Table 7.1. The scan size was deliberately limited to about 70 % of the maximum available range to minimise the possibility of arcing between the quadrants of the scan tube in the low pressure helium gas. The number of data points is a compromise between resolution and the time taken to acquire an image. The design of the cryostat means that regular intervention from the operator is required to maintain stability at the lowest temperatures and therefore measurement series requiring continuity must be completed in a day.

Careful consideration was given to the voltages applied to the tip in order to mini-

mize disturbance of the system.

A contact potential difference exists between the tungsten tip and GaAs sample due to a difference in their work functions. Kelvin probe measurements were used to estimate this difference. With the tip over a point in the bulk of the sample and the z-feedback loop switched off, the DC bias applied to the sample was varied between $-1\,\mathrm{V}$ and $0\,\mathrm{V}$ whilst recording the frequency shift of the tuning fork. The minimum in the frequency shift curve corresponded to the DC bias needed to compensate the contact potential difference. The measured contact potential difference was not consistent and varied with the tip position by as much as $0.2\,\mathrm{V}$. This variation could be due to surface contamination, or an unstable oxide layer on the tip or on the surface of the GaAs. In future experiments a sample heater will be installed to reduce material condensing on the surface during loading and unloading the microscope. The tip material will be changed to a platinum-iridium alloy as this does not develop an oxide layer.

The RF signal applied to the tip by the capacitance detector was reduced as far as possible whilst maintaining enough signal to make measurements with a bandwidth fast enough for scanning. The RF voltage at the tip was estimated as $0.5\,\mathrm{mV}_{rms}$ using the equivalent circuit model of the tuned filter (see Section 5.2.1). This is comparable to the excitation applied to top gates in early bulk magnetocapacitance measurements of 2DEGs [121].

Figure 7.16(a) is a $\hat{Y}$ image taken at the edge of the 2DEG between contacts 7 and 8 (see Fig. 7.6(b)) at $2.2\,\mathrm{K}$. Contours from the topographic data have been superimposed: the white contour follows the sample edge with the Hall bar to the left, the black contours indicate significant features on the surface. Figure 7.16(b) shows simultaneously acquired line scans of the topography and the $\hat{Y}$ signal.

There are four main observations:

- $\hat{Y}$ signal is high on the Hall bar where there is a 2DEG and five times smaller over the etched region.
- On the Hall bar there is a correlation between high regions of the topography and lower $\hat{Y}$ signal.

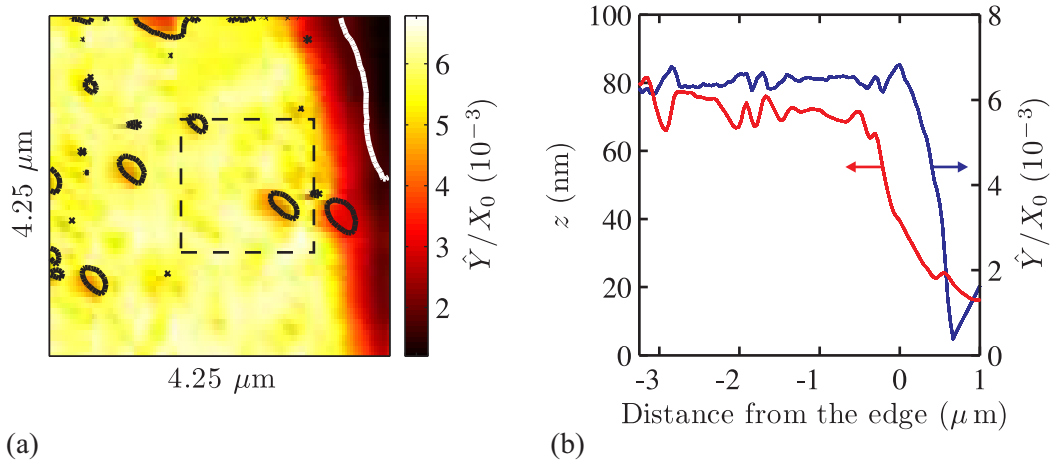

Figure 7.16: (a) $\hat{Y}$ image of edge of a 2DEG at zero-field and 2.2 K. White contour indicates the edge of the sample with the Hall bar to the left, black contours indicate topographic detail. (b) Simultaneously measured topography and $\hat{Y}$ line scans of the same sample.

- There is a small inflection in the $\hat{Y}$ signal just as the signal begins to rise as the tip approaches the sample edge.
- There is a region on the Hall bar parallel to the edge approximately 0.5 μm wide where the $\hat{Y}$ signal is reduced.

The first observation is very significant as it shows that the $\hat{Y}$ measurement is sensitive to the presence of a 2DEG buried tens of nanometres below the surface. Without the 2DEG one would expect a decrease in signal over the Hall bar as the probe assembly is pulled back further and the stray capacitance is reduced. This effect probably explains the anti-correlation between between topographic features and the $\hat{Y}$ signal and is discussed in more detail in Section 7.5.3. The region parallel to the edge with decreased signal could be a measurement artefact due to the geometry or it may relate to the depletion region expected at the edge of a 2DEG. This is discussed in Section 7.5.2. The inflection in the $\hat{Y}$ signal on the approach to the edge is an artefact caused by a change in the tip-sample capacitance due to the sample geometry. This was investigated with a finite element simulation and is described in Section 7.5.1.

7.5.1 Finite element simulations

A simple finite element simulation was carried out to try to understand qualitatively the effect of the step at the edge of the Hall bar on the $\hat{Y}$ signal. In constructing this model the following assumptions were made

- The conductivity of the 2DEG is high and it can be represented by a metal.
- At zero-field, changes in $\hat{Y}$ are only due to changes in the size of the tip-sample capacitance.
- $\hat{Y}$ is proportional to the difference in capacitance between the closest and furthest points of the tip oscillation.

A full 3D simulation was performed using the electrostatics module of a commercial finite element package[2]. The tip was modelled with a hemisphere, radius 100 nm, as the tip apex and a cylinder as the extended body of the tip. The sample was represented by a metallic slab of 100 nm thickness. Figure 7.17(b) shows the output of the finite element model; the colour scale plot is one slice of the solution showing the calculated electric field. The tip-sample capacitance was calculated for various tip positions to simulate a line scan across the edge of the sample. Figure 7.17(a) shows the result of these simulations, the black line indicates the surface, the conductive slab is the raised portion to the left. The blue lines indicate the path of the tip over the edge and the red lines are the calculated tip-sample capacitance. The calculation was carried out for tip-sample separations of 10 nm (solid lines) and 110 nm (dashed lines). The green curve is the difference between 10 nm and 110 nm curves and should relate qualitatively to the measured $\hat{Y}$.

The simulation shows that within two tip radii of the edge the tip-sample capacitance over the 2DEG is very close to the bulk value. A small inflection in the capacitance is seen approximately one tip radius away from the edge on the etched side. A very similar feature can be seen in the experimental data (for example, in the line scans in

[2]COMSOL Multiphysics 3.1 - www.comsol.com

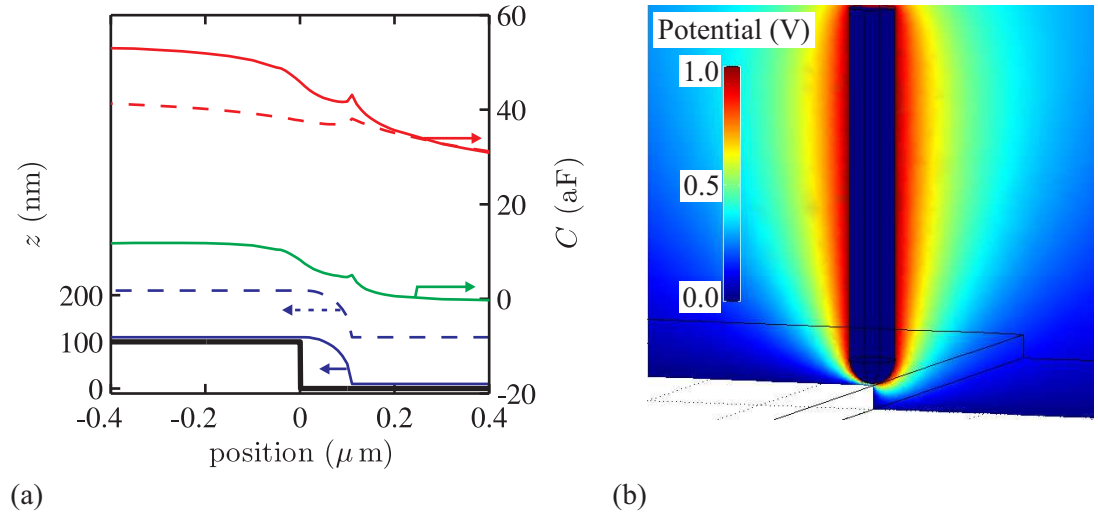

Figure 7.17: (a) Calculated capacitances from finite element simulation. Black line indicates the position of the surface, blue lines indicate tip apex position and red lines are the calculated tip-sample capacitance for the two tip-sample separations. The green line is the difference between the two capacitance curves. (b) Finite element simulation of the electric field between a tip and a metallic block. Colour plot shows a slice of the calculated electric field.

Fig. 7.16(b)). Future extensions to this work would be to incorporate a more realistic tip shape and to model the 2DEG as a thin metal sheet buried in a dielectric rather than a metallic slab.

7.5.2 Depletion length

The carrier density varies smoothly from the bulk value, n_s, to zero at the edge with a characteristic length scale, d_0 the depletion width. In ref. [28] this length was calculated assuming the edge was defined by a gate electrode in the plane of the 2DEG

$$d_0 = \frac{4\epsilon_0\epsilon_r}{\pi e^2}\frac{V_g}{n_s} \tag{7.3}$$

where V_g is the potential difference between the gate and the 2DEG. In an etched structure the surface charges pin the Fermi energy at the surface to the middle of the bandgap of GaAs so that $V_g = E_G/2e$ [27] where $E_G \approx 3\,\text{eV}$ is the bandgap of GaAs. Using this expression it is possible to calculate the depletion length $d_0 = 200\,\text{nm}$.

As discussed earlier there is a region parallel to the edge where the signal level is reduced, it is difficult to determine how much of this contribution is due to the geometric effect of the step and how much is the depletion of the 2DEG. A possible way to investigate this further would be to image a sample where the density could be controlled with a backgate. As the density is modified then the width of the depletion region should change.

7.5.3 Topographic artefacts

Figure 7.18 shows $\hat{Y}$ images from the forward and reverse scan direction of the region indicated by the dashed box in Fig. 7.16(a). The black contours mark raised features in the topography and it can be seen that these correlate with a reduced $\hat{Y}$ signal. The origin for this could be the effect of the probe assembly withdrawing from the surface as discussed earlier, or it could be that these topographic features are a contaminant with different electrostatic properties, for example metallic particles or an insulator with a different dielectric constant. Another observation is the lateral translation between the

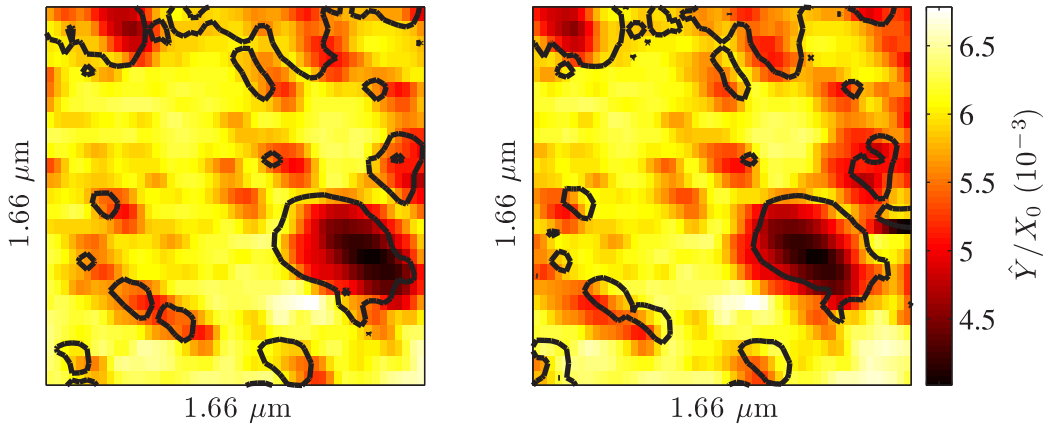

(a) (b)

Figure 7.18: Shift of topographic artefacts in the $\hat{Y}$ image due to AFM control problems. (a) Forward scan. (b) Reverse scan.

features in the $\hat{Y}$ data and the topographic data. The direction of the shift is reversed between the two scan directions which suggests this a control problem rather than a tip asperity. The shift is approximately 100 nm which is a couple of percent of the scan range. This is an order of magnitude less than the length scale of the magnetic structure observed later in the chapter.

7.6 Scanning measurements in applied magnetic field

The images presented in this section have been scaled in the raw measurement units normalized to the amplitude of the RF signal X_0 at zero-field rather than rescaling them as conductivity. The agreement between the experimental point spectra and the modelling is strong enough to support the conclusion that the measurement is dominated by the local conductivity. However, it is not yet good enough to justify rescaling the image data. The modelling of the point spectra assumes that the sample is homogeneous. Close to integer filling factors this is not the case. Overall, high signal (bright areas of the images) can be interpreted as high local conductivity and low signal (darks areas) as low local conductivity.

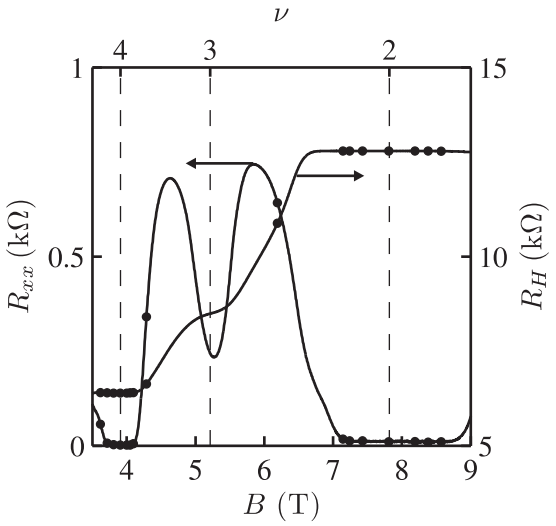

Figure 7.19: Magnetoresistance data with markers indicating the fields at which images were acquired.

A problem with the instrumentation during this run of experiments meant that the phase of the reference signal for the in-phase part of the RF signal was incorrect. The result of this is that the measured $\hat{X}$ was a mixture of $\hat{X}$ and $\hat{Y}$ components and for this reason these measurements have not been included.

The first part of this section presents a series of images as a function of magnetic field, in the following subsections significant features of the data are discussed in detail.

7.6.1 Description of the data

Measurements were made between filling factors $\nu = 1.8$ and $\nu = 4.5$ at the magnetic fields indicated by points on the magnetotransport curves in Fig. 7.19. The measurements are concentrated around filling factors $\nu = 2$ and $\nu = 4$. A selection of $\hat{Y}$ images from the magnetic series are shown in Fig. 7.20. For identification, the filling factor ν is given below each image along with the image number in brackets indicating the position in the image series. The images are arranged in two cycles, the first two columns are points taken around filling factor $\nu = 4$ and the last two are points around $\nu = 2$. Images on the same rows of columns one and three and columns two and four are at

corresponding points in the two cycles for example $\nu = 3.8$ and $\nu = 1.8$. The aim of this layout was to examine if the features in the images display $1/B$ periodicity.

Initially the filling factor was calculated from the transport data but this did not quite match the periodicity of the structure seen in the images. A single pixel in the image was plotted as a function of magnetic field and from the periodicity of this curve the local density was extracted. The location and field plot for this pixel is indicated by Label 1 in Fig. 7.6.4. The new density was found to be $n_m = 3.85 \times 10^{15}\,\mathrm{m}^{-2}$ compared to the transport measurement $n_s = 3.79 \times 10^{15}\,\mathrm{m}^{-2}$. This is within the error associated with the density calculation. The dashed lines in Fig. 7.19 indicate the position of integer filling factor and were calculated with the local density.

Filling factors $\nu = 4.3$ to $\nu = 3.65$

The transition through filling factor $\nu = 4$ is shown in the series of images in the first two columns starting at the top left of Fig. 7.20.

At $\nu = 3.65$ the structure of the image is similar to zero-field, the signal is high over the 2DEG except for the depleted region along the edge. The depleted region has the same magnitude and width as the zero-field case. The remainder of the signal on the 2DEG is homogeneous except for artefacts from topographic features. The signal level is lower than at zero-field but this is consistent with the point spectra results in the bulk where a decreasing background with increasing field is observed. This decrease is attributed to a fall in the conductivity.

At $\nu = 4.21$ the signal over the 2DEG is reduced and a bright feature is seen close to the centre of the image (Label (1)).

Reducing the filling factor to $\nu = 4.11$ the change in signal is no longer homogeneous across the 2DEG. The biggest reduction in signal is seen in regions to the left of the image, closer to the bulk of the 2DEG, a narrow stripe of high signal remains close to the edge. The bright spot in the centre of the image has remained constant in magnitude but has a greater lateral extent.

At integer filling factor $\nu = 4$ the only region of high signal is a stripe approximately

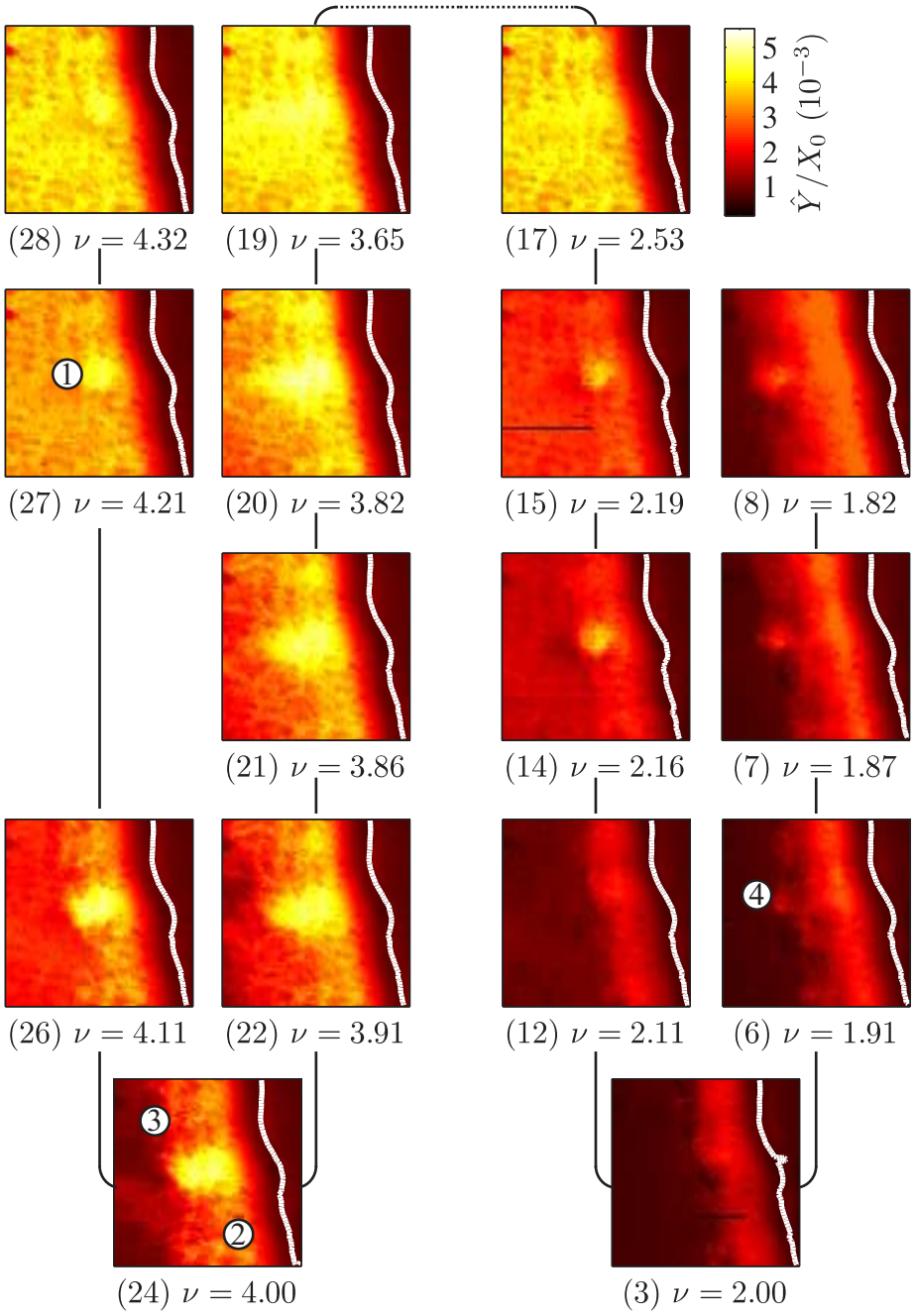

Figure 7.20: Selected $\hat{Y}$ images from the magnetic field series taken at 2.2 K. The lateral scale is $4.25 \times 4.25\,\mu$m and the colour scale is shown in the top right. The white contour indicates the position of the edge. The collage shows two periods, the first two columns are around filling factor $\nu = 4$ and the last two are centred on filling factor $\nu = 2$. Numbers in brackets show image number in the order taken. Filling factors have been corrected for local density variation (see text).

2 μm wide close to the sample edge. The signal over the remainder of the 2DEG is the same as the etched region away from the Hall bar. The stripe is not homogeneous and has a brighter region on the right side about 0.5 μm wide (Label 2). Close inspection reveals a narrow dark stripe along the left edge of the bright stripe where the signal is lower than the etched region (marker (3)) This is not very clear in this figure but can be seen in a line scan in Section 7.6.3. The bright spot in the centre of the image is slightly enlarged.

Between $\nu = 4$ and $\nu = 3.82$ the background signal begins to recover and the width of the stripe and the bright region within the stripe broadens. The bright spot remains constant but begins to be obscured by the increasing background.

At $\nu = 3.65$ the image looks similar to the zero-field case. The signal across the 2DEG (excluding the depleted band at the edge) is high and fairly homogeneous.

Filling factors $\nu = 2.53$ to $\nu = 1.82$

The transition through filling factor $\nu = 2$ is shown in the last two columns of Fig. 7.20. The evolution of a bright stripe at the edge follows the same pattern as around $\nu = 4$ which demonstrates the $1/B$ periodicity of this feature. The main differences are the average signal level which is lower and the width of the stripe which is narrower.

At $\nu = 2.53$ the image is comparable to the zero-field case and is almost indistinguishable from $\nu = 3.65$ and $\nu = 4.32$.

At $\nu = 2.19$ the signal over the 2DEG has decreased except for a bright region in the centre which corresponds to the feature seen in the previous set of images. There is no clear distinction between regions of the 2DEG close to the edge and close to the bulk. This lack of structure is also seen in the image at $\nu = 4.21$.

The stripe structure is well developed by $\nu = 2.11$ and the region of the 2DEG on the left has already fallen very close to the signal over the etched region. The signal on the stripe is about 30 % smaller than at $\nu = 4.11$. Another interesting observation is that the bright feature previously seen at the centre of the image has disappeared.

At integer filling factor $\nu = 2$ the bright stripe is separated from the rest of the

2DEG by a narrow black stripe. The signal level close to the bulk is the same as the etched region. The stripe at $\nu = 2$ is approximately 2/3 of the width at $\nu = 4$.

Between $\nu = 2$ and $\nu = 1.82$ the width of the stripe makes it possible to see the evolution more clearly than the $\nu = 4$ period. The growth of the stripe is much more gradual than its onset around $\nu = 2.16$. The stripe becomes brighter as it gets wider and a small feature develops just to the right of the centre of the image.

Unfortunately no images were taken at filling factors less than $\nu = 1.82$ so it is not possible to see if the signal becomes homogeneous again.

Summary

The signal over the etched region and the depleted region of the 2DEG remains constant and is the same as at zero-field. Away from integer Landau level filling factors the signal over the 2DEG is comparable to zero-field. At integer filling factors a narrow stripe of high signal is seen at the edge and the remainder of the 2DEG has the same signal level as the etched region. The width of the stripe depends on filling factor and is greater at $\nu = 4$ than at $\nu = 2$. There is a general decrease in signal level over the 2DEG with decreasing filling factor which is consistent with the point spectra measurements and the interpretation of a reduction in conductivity.

The relative signal level over the etched region, stripe and close to the bulk are discussed in the next section. The evolution of the stripe and comparison to theory is discussed in Section 7.6.5. Very close to integer filling factors a narrow dark stripe is seen at the left edge of the bright stripe this is discussed in Section 7.6.3. A couple of anomalous features are seen in the images which don't appear to be periodic with filling factor and are discussed in Section 7.6.2.

7.6.2 Anomalous features

In the magnetic field series a couple of bright point features were observed. These did not appear to change with magnetic field but were more or less pronounced depending on the background level. The evolution of these features is correlated with the order

in which the images were taken. The bright feature indicated by Label 1 in Fig. 7.20 appears in image number 12 and increases in size with increasing image number. After each image the SPM controller returns the tip to the centre of the image and controls over a point until the image acquisition is restarted. The tip typically spent a few minutes in this position between each scan and over the course of the 28 images this is a significant amount of time. If the work function difference was not compensated perfectly it might be that some surface states have been charged up in this region or that imaging this point more heavily has deposited some debris from the tip. To minimize this effect in the future the tip could be moved to a corner of the scan area immediately after each scan.

7.6.3 Dark stripe

Close to integer filling factors the $\hat{Y}$ images show a bright stripe at the edge separated from the rest of the sample by a very narrow dark stripe, an example of this can be seen in Fig. 7.22(a).

Figure 7.21(a) shows a line scan across the edge at filling factor $\nu = 2$ with the etched region to the left. The problem with the instrumentation was resolved before this set of measurements was made making it possible to measure $\hat{X}$ and $\hat{Y}$. The $\hat{Y}$ trace shows similar features to the images, there is a peak corresponding to the bright stripe approximately 700 nm inside the sample. Close to the bulk of the sample the signal level is the same as the etched region. Exactly at the edge a small peak is seen in the $\hat{Y}$ signal which can explained by the geometry of the step edge and was discussed in Section 7.5.1. There is a sharp minimum in the signal just after the peak at a distance of 1.7 μm from the edge corresponding to the narrow dark stripe. The $\hat{X}$ trace is zero everywhere except for a sharp peak which corresponds with the minimum in the $\hat{Y}$ signal.

Figure 7.21(b) is simulated response of $\hat{X}$ and $\hat{Y}$ as a function of the sample conductivity σ_{xx}. This figure is reproduced from earlier in the chapter and is discussed in Section 7.4.2. This model shows that in the transition from the low to high resistance

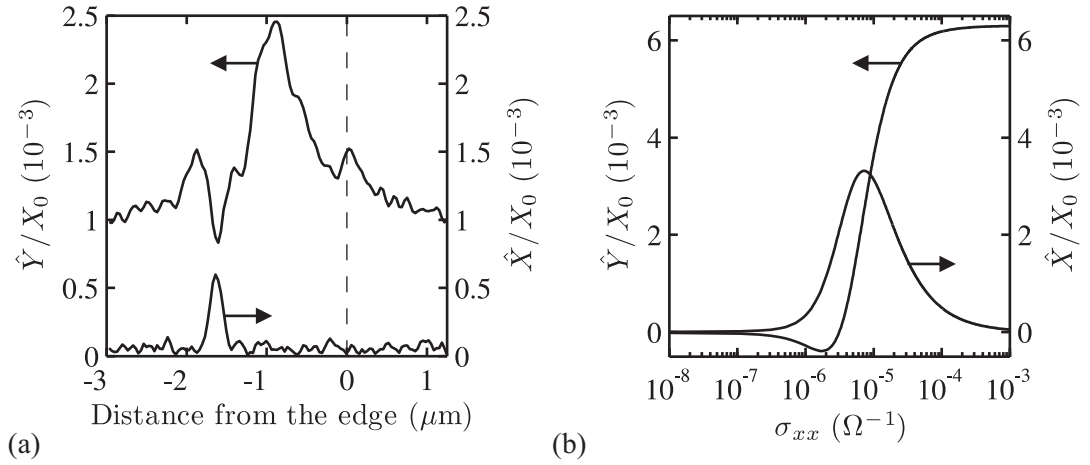

Figure 7.21: (a) Line graph showing $\hat{Y}$ and $\hat{X}$ over a single line across the edge of the sample at filling factor $\nu = 2$. The dashed line indicates the position of the edge. (b) $\hat{Y}$ and $\hat{X}$ as a function of the sample resistance R_s from the model.

regime $\hat{X}$ goes through a maximum and $\hat{Y}$ through a minimum. The maximum and minimum do not correspond to the same resistance but if the transition happens over a small spatial region they might appear to coincide. Using this model the dark stripe in the $\hat{Y}$ data can be interpreted as a measurement artefact which indicates the transition from a high conductivity region close to the edge to a low conductivity region closer to the bulk. The fact that $\hat{X}$ is zero everywhere else is another indication that the sample is divided into regions of very high and very low conductivity.

The model only includes coupling through the 2DEG and at the moment does not reproduce the background seen over the etched region. More work needs to be done in the future to include this.

7.6.4 Single points versus field

To examine the behaviour of the signal over different regions in the imaging area single points were selected and plotted as a function of magnetic field. Figure 7.22(a) is one of the images showing the location of the points plotted in Fig. 7.22(b). Points were positioned on the etched region (Label 1), on the far left of the image close to the bulk of

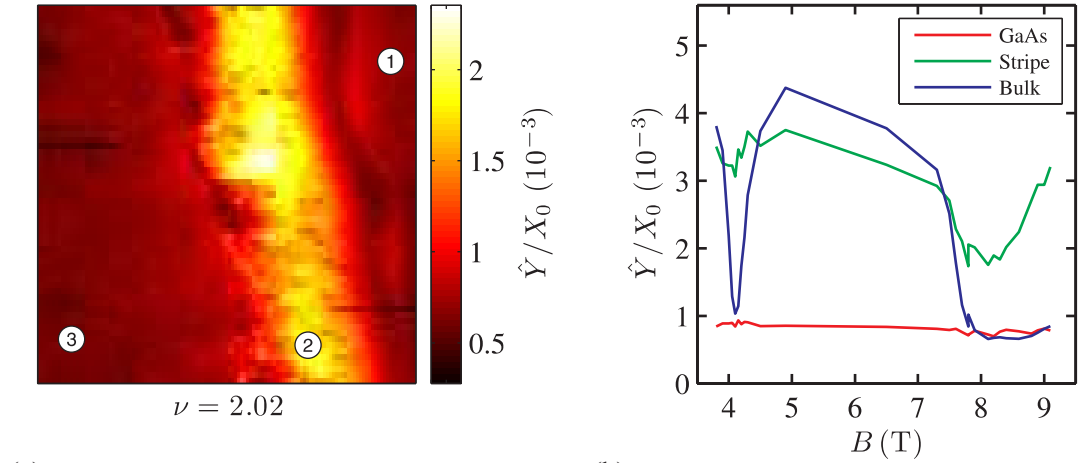

Figure 7.22: (a) $\hat{Y}$ image at 8 T. Labels indicate spatial location of points plotted as a function of magnetic field in Fig. 7.6.4(b). (b) $\hat{Y}$ as a function of magnetic field for three points in the image series. Point 1 is over the etched region, Point 2 is close to the edge where the stripe structure develops and Point 3 is close to the bulk.

the sample (Label 3) and close to the edge where the stripe of high signal develops (Label 2). Care was taken to avoid regions of the image where any of the anomalous bright features are seen. The signal over the etched region (Label 1) remains constant. The electrostatic properties of the GaAs are expected to remain unchanged in a magnetic field. This is an important result as it shows the measurement system is unaffected by the change in applied field and shows that the microscope is indeed able to make local measurements.

The signal close to the bulk (Label 3) varies strongly with magnetic field and resembles the point spectra measurements in the bulk with strong minima at integer filling factors and a background decrease with increasing field. This indicates that this region of the sample is behaving in a similar way to the bulk of the sample. The minima from this curve were used to estimate the local density as discussed in Section 7.6.1.

The signal over the stripe shows aspects of the bulk behaviour seen in the curve at Point 3, the background is a similar size and has corresponding minima with reduced magnitude.

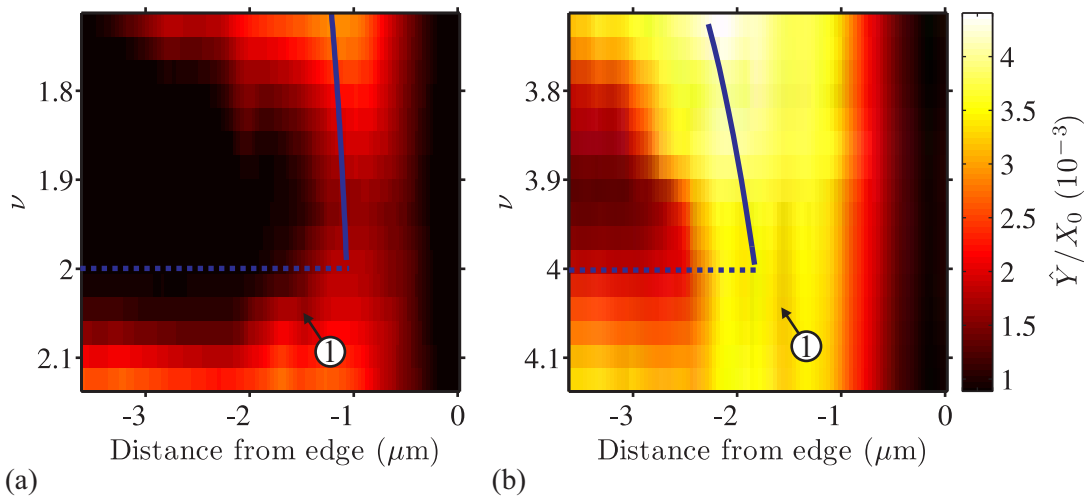

Figure 7.23: $\hat{Y}$ as a function of distance from the edge and filling factor. (a) Around filling factor $\nu = 2$ and (b) $\nu = 4$. These data were extracted from the magnetic field series; the data processing is discussed in detail in Section 7.6.5. The solid blue line indicates the position of the innermost compressible stripe from theory; the dashed blue line indicates the point at which the innermost incompressible stripe diverges into the bulk of the sample.

7.6.5 Evolution of the stripe versus filling factor

Figure 7.23 shows the $\hat{Y}$ signal versus distance from the edge and filling factor where Fig. 7.23(a) is around filling factor $\nu = 2$ and Fig. 7.23(b) is around filling factor $\nu = 4$. These two figures show the same range of filling factor and have the same colour scale to simplify comparison.

In each image in the field series a number of line sections were taken perpendicular to the edge of the sample and averaged. These averaged line sections at different filling factors were used to compile the two figures. There are gaps in the data at particular filling factors and 2D interpolation has been used to make a smooth plot.

In these images it is easy to compare the width of the depletion region as a function of filling factor and it is clear that it remains constant. In both images the evolution of the stripe is similar: the onset of the stripe approaching integer filling is more gradual than the expansion of the stripe above integer filling. The stripe structure is much brighter around $\nu = 4$, this could be because the conductivity is higher at lower fields.

Some of the structure seen in these images is due to topographic artefacts for example the dark feature seen in both images (Label 1).

The solid blue lines indicate the position of the innermost incompressible stripe from theory [27] (Eqn 2.22). The data is in reasonable agreement with the theoretical prediction close to integer filling but the stripe width increases faster in the data than predicted by the theory. This theoretical expression (Eqn 2.22) is only valid for $\nu - k << \nu$ [27] where ν is the bulk filling factor and k is the local filling factor at the edge. In the data shown in Fig. 7.23(a) the bulk filling factor varies between $\nu = 1.75$ and $\nu = 2.15$ and the innermost incompressible stripe is at the position of local filling factor $k = 1$. In the data shown in Fig. 7.23(b) the bulk filling factor varies between $\nu = 3.75$ and $\nu = 4.15$ and the innermost incompressible stripe is at the position of local filling factor $k = 3$. In both cases $\nu - k << \nu$ is only satisfied very close to integer filling. It might be that the disagreement between the theory and experiment is because the theory is not valid in these limits.

7.6.6 Edge state around a locally depleted region of the 2DEG

Figure 7.24 is a collage of 14 images taken over 3 hours of an area close to the edge of the 2DEG at filling factor $\nu = 2$. The lower collage shows the topography and the top collage the $\hat{Y}$ measurement. The individual topographic scans were plane fitted and the centre position of the scale was offset to align the images. No image processing was applied to the $\hat{Y}$ images. This image series is good test of the stability of the measurement technique, it is very difficult to see the boundaries where individual images overlap and there is no obvious drift in the signal level across the collage.

In the top right of the $\hat{Y}$ collage a narrow bright stripe is observed and is comparable to other images taken at $\nu = 2$. The stripe is positioned just inside the sample approximately 700 nm from the edge and has a width of 1 μm. Small dark features inside the stripe are artefacts which correspond to raised features in the topography. Separating the stripe from the bulk region is a narrow dark stripe where the signal level is lower than the etched region. The signal level over the bulk is the same as the

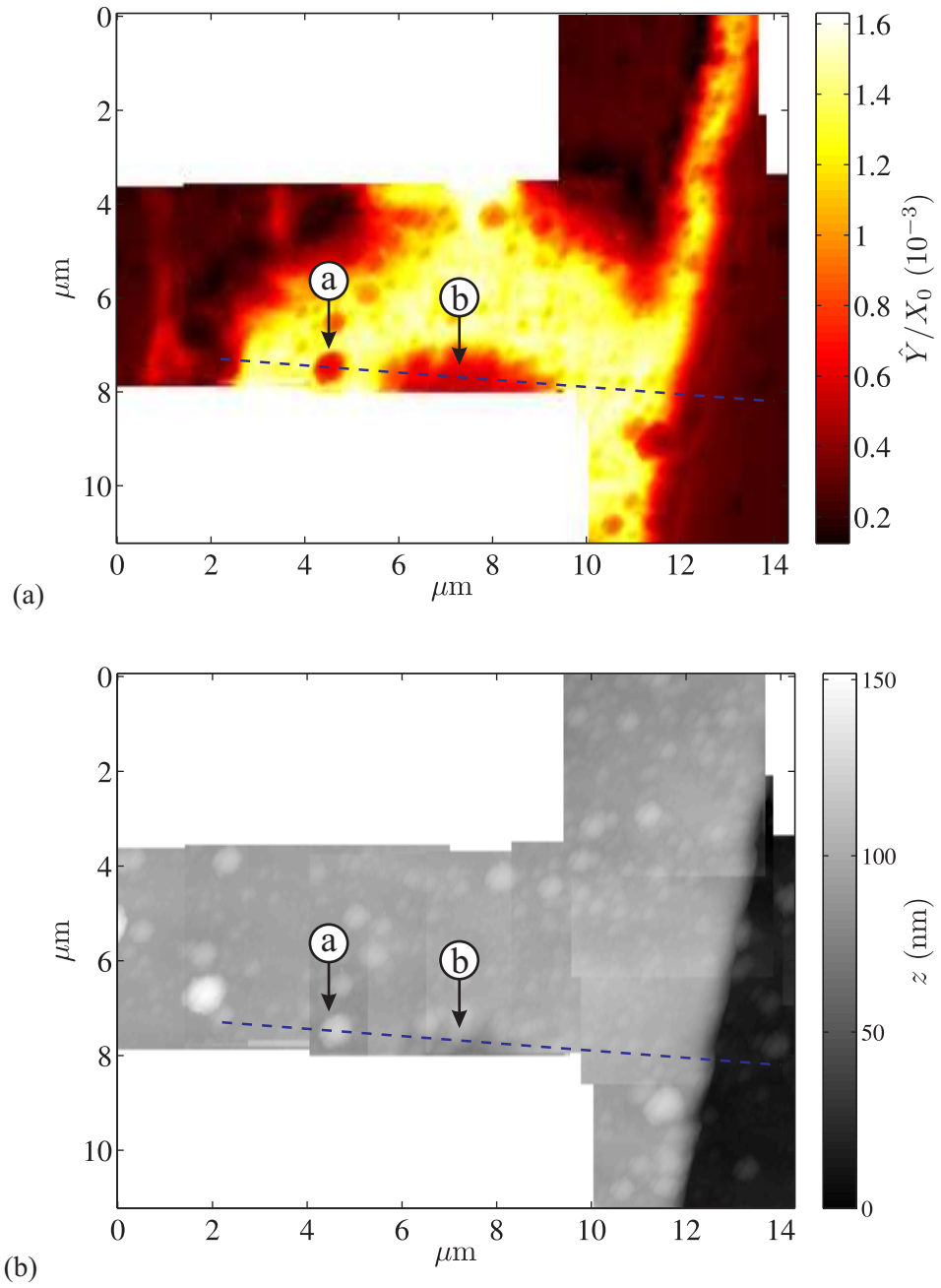

Figure 7.24: A collage of 14 images taken over 3 hours close to the edge of the Hall bar. Bottom collage is the topography, the constituent images have been plane fitted to compensate for thermal drift of the microscope during the scan. The upper collage shows the $\hat{Y}$ data, without any image processing. Blue line indicates a cross-section through the data shown in Fig. 7.25. (Label a) indicates a region of raised topography. The geometric effect of this feature causes a decrease in the $\hat{Y}$ signal. (label b) There is a strong decrease in $\hat{Y}$ but this does not correlate with a region of raised topography.

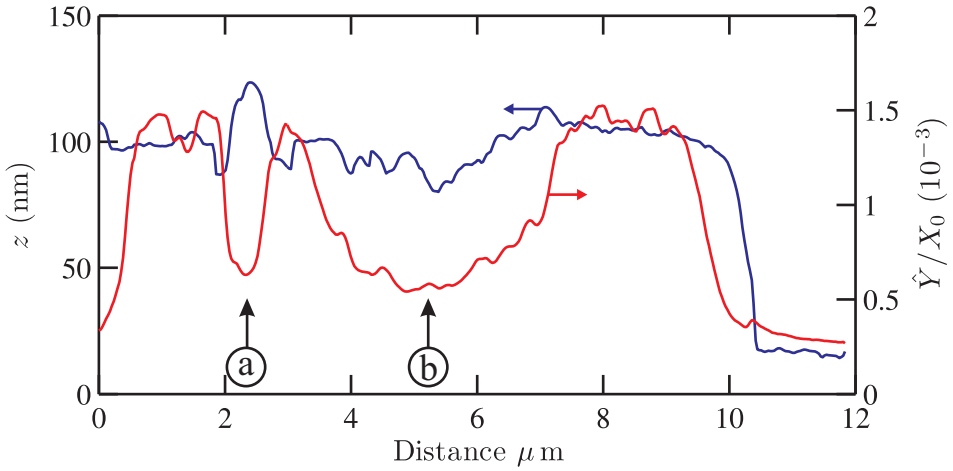

Figure 7.25: Cross-section through the collage shown in Fig. 7.24 where the position is indicated by a blue dashed line. Blue line is the topography and the red line is the $\hat{Y}$ signal. (Label a) indicates a high point in topography, the geometric effect on the tip-sample capacitance causes a corresponding dip in the $\hat{Y}$. (label b) a region of decreased $\hat{Y}$ signal which does not correspond to raised area in the topography. The decrease in this region is attributed to a local depletion of the 2DEG.

etched region.

A circular stripe of enhanced conductivity, located about 5 μm from the sample edge, appears further down the image. The width of the stripe is $\approx 3.8\,\mu$m, about 3 times larger than the one found at the physical edge of the sample. Figure 7.25 shows a cross-section of the topography and $\hat{Y}$ signal, as indicate by the dashed lines in Figs. 7.24(a) and (b). A topographic maximum leads to a minimum in $\hat{Y}$, as can be seen at position (a); at position (b), i.e. in the centre of the ring structure $\hat{Y}$ is reduced to about 1/3 of the stripe maximum. Unlike at position (a) this reduction is not due to a topographic feature. Position (b) coincides with the tip position of prior point spectroscopy experiments, which suggest that the ring shaped feature is caused by a permanent local depletion of the 2DEG. For reasonably smooth potentials, the width of a compressible stripe is determined by the electron density distribution at zero field [27]. It is expected that the potential and therefore the electron density around the

depleted region varies on a different length scale than at the physical edge. A shallower density gradient, as expected for charged surface states 50 nm above the 2DEG would result in an enhanced stripe width as seen in the data.

7.6.7 Sample bias

During imaging the tip is at DC ground and a voltage is applied to the 2DEG to compensate the work function difference between the tip and sample. Measurements to determine the work function difference are unreliable possibly due to spatial variations of this quantity across the sample or the oxide layer on the tip. Given the uncertainty in the work function difference a series of images was taken to look at the effect of the sample bias.

Figure 7.26 shows three of the images taken as a function of the sample bias at filling factor $\nu = 2$. The DC bias was applied to all the sample contacts so that there was no net current flowing through the sample. The work function difference between the tip and sample was compensated by applying a bias of approximately $-0.3\,\mathrm{V}$ to the sample, images were taken over a range of $\pm 0.2\,\mathrm{V}$ from this value. The graph in the bottom right shows the signal level at three different positions as a function of the sample bias.

The signal over the etched region remains constant which is expected as there is no electrical connection to the contacts. The bulk region of the 2DEG also remains constant, this is consistent with theory which predicts at integer filling factors the electrochemical potential of the contacts is carried by the edges and the bulk is isolated. The stripe gets brighter and appears to broaden slightly as the bias is increased. At the most negative bias a narrow dark stripe separates the bright stripe from the bulk, as the bias is increased this feature disappears. The apparent change in width and disappearance of the dark stripe might be related to the overall increase in signal over the stripe. At the edge of the stripe some of the signal is due to coupling to the stripe, as this contribution increases with bias then the bright stripe may appear wider and the dark stripe washed out.

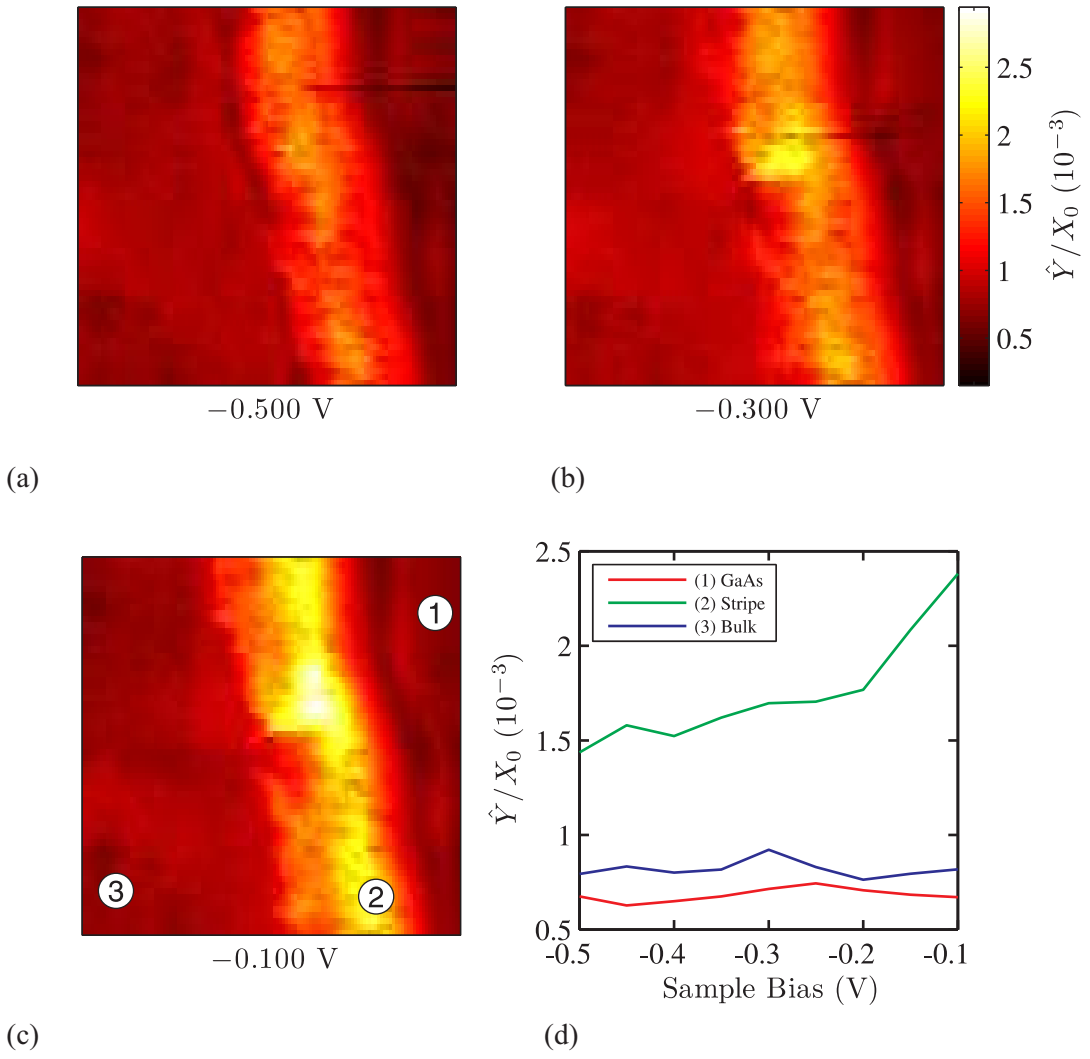

Figure 7.26: Images showing $\hat{Y}$ as a function of sample bias at 2.2 K and filling factor $\nu = 2$. (a)-(c) Selection of images from the bias series. (d) Graph showing the evolution of three points as a function of sample bias.

The main observation is that the stripe gets brighter as the sample becomes more positive. The two explanations for this are that the measurement set-up is sensitive to the DC potential or that the tip-sample potential difference is perturbing the sample. Analysis of the measurement set-up has not revealed any obvious mechanism that causes the $\hat{Y}$ signal to be sensitive to the tip-sample potential.

It is possible that the tip acts like a local gate accumulating or depleting charge. The tip is held at DC ground, if the tip-sample work function difference is $-0.3\,\mathrm{V}$ at a sample bias of $-0.6\,\mathrm{V}$ the tip has a potential of $0.3\,\mathrm{V}$ with respect to the 2DEG. With a sample bias of $0\,\mathrm{V}$ the tip has potential of $-0.3\,\mathrm{V}$ with respect to the 2DEG. In the image series the tip potential relative to the 2DEG is getting more negative as the sample bias is increased and the effect of this would be to deplete the 2DEG. The filling factor ν is given by:

$$\nu = \frac{h}{e}\frac{n_s}{B} \tag{7.4}$$

The magnetic field is fixed so, as the local density is reduced, the local filling factor, ν, decreases. The scans as a function of magnetic field show that in the vicinity of integer filling a decrease in filling factor (increase in field) leads to the stripe gradually getting wider and brighter. This can be seen in the point graphs shown in Figure 7.22. This change in the local filling factor could explain the change in the images as a function of bias. This hypothesis could be investigated further using a backgated sample to modulate the density.

7.7 Scanning measurements with an applied current

Previous experiments have shown that above some critical current the quantum Hall effect breaks down [6]. There are a number of proposed mechanisms for this breakdown including electron heating [122], intra [123] and inter [124] Landau level transitions and tunnelling between Landau levels caused by the Hall field [125]. No conclusive theory of the breakdown is available yet and scanning probe techniques might be able to help solve this by making local measurements.

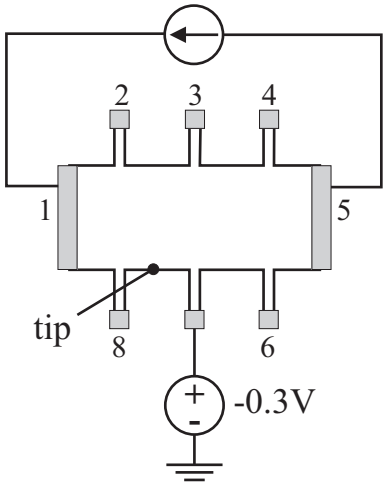

Figure 7.27: Schematic showing the connections to the sample during the current measurements. A floating current source applies a constant current. The edge where the tip is located is fixed at potential of $-0.3\,\mathrm{V}$ to compensate the tip-sample work function difference.

Measurements in the breakdown regime are a future aim of the research and as a first step it has been possible to demonstrate that the technique can image edge states with an applied current.

Figure 7.27 shows the electrical connections to the sample and the location of the tip during the current experiments. The current was provided by a battery powered constant current source. One contact was fixed at a potential of $-0.3\,\mathrm{V}$ relative to ground to compensate the tip-sample work function difference. The tip was positioned along the same edge. In the quantum Hall regime this edge and therefore the scan area will be fixed at the potential of the voltage source. This was the last set of experiments on this sample and unfortunately problems with some of the contacts meant that it was not possible to make magnetoresistance measurements at the same time.

7.7.1 Description of the data

Figure 7.28 shows a series of images at the edge of the sample at filling factor $\nu = 2$ as a function of the applied current.

With no applied current a stripe of high signal is seen close to the edge and the

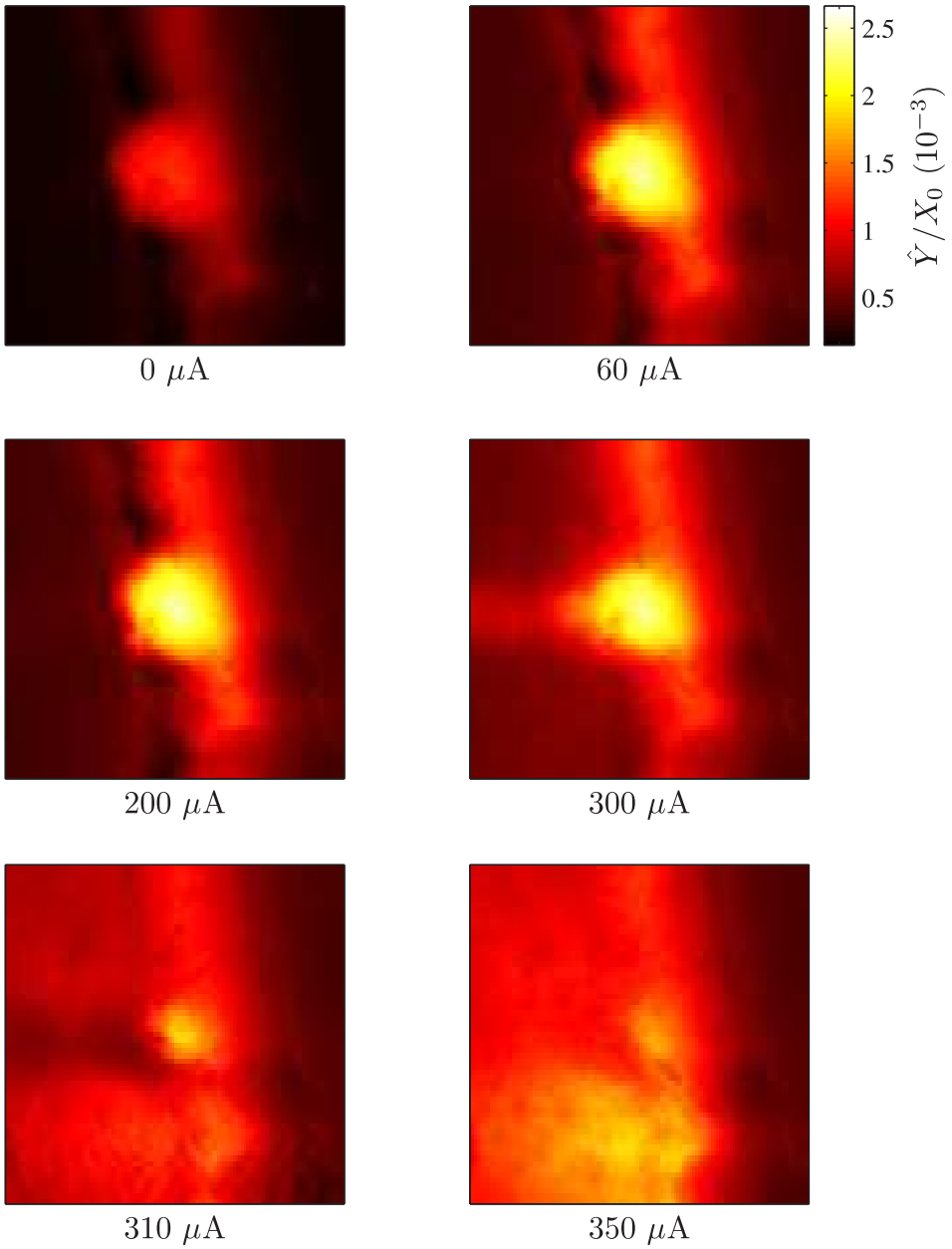

Figure 7.28: Series of $4.25 \times 4.25\,\mu$m $\hat{Y}$ images taken as a function of DC current through the sample at 2.2 K and filling factor $\nu = 2$.

signal towards the bulk region (left of the image) is the same as the etched region. At the edge of the bright stripe a narrow dark stripe can be seen which is very similar to previous images. There is a bright region in the centre of the scan which is an artefact; the cause is uncertain but might be due to charging of surface states. As the current is increased the stripe gets brighter and appears to get wider. Between 300 μA and 310 μA the structure of the image changes dramatically, the stripe is no longer well defined and the brightest regions extend into the bulk part of the sample. The potential along this edge should be held constant in the quantum Hall regime so the increase in brightness cannot be explained by a change in the tip-sample potential as seen in the bias experiments. The change in structure might indicate that quantum Hall breakdown has occurred, previous measurements made on same wafer by Shashkin *et al* found a breakdown current of 150 μA with a 280 μm wide Hall bar [120].

Without corresponding magnetoresistance data it is difficult to interpret these measurements. However, they have demonstrated that the measurement technique is able image edge states with an applied current.

7.8 Summary

In this chapter measurements were made over a near surface 2DEG. At integer filling factors a stripe of high conductivity develops at the edge of the device. Well away from integer filling factors then the response over the 2DEG is homogeneous similar to the zero field case. A simple model was developed to account for the major features of the images. In the next, and final, chapter the major findings of this research will be summarized and suggested directions for further research will be discussed.

Chapter 8

Conclusions and suggestions for future work

This thesis has discussed the implementation of a scanning capacitance microscope which can operate at low-temperatures and high magnetic fields. Studies of a 2DEG in a magnetic field were performed and the formation of highly conductive stripes at the physical edge of the sample were observed in agreement with theoretical predictions. This chapter includes a brief summary of the main areas of the project and some suggestions for future work.

8.1 Summary

8.1.1 Experimental setup

An SPM has been developed which allows simultaneous AFM, SCM and transport measurements to be made at low temperatures and high magnetic fields. AFM measurements are made in a dynamic mode using a quartz tuning fork force sensor and electrochemically etched tungsten tip. The microscope has a lateral resolution better than 50nm and a scan area of $7 \times 7\,\mu$m at low temperature. Measurements can made in a low pressure of helium gas or superfluid helium. The temperature range of the microscope is 1.5-300 K and magnetic fields of 0-12 T can be applied perpendicular to

the sample. Quartz tuning fork (QTF) force sensors are used as they are piezoelectric and can be applied in self exciting/sensing configuration without the need for an optical deflection detection system. They have a very low power consumption and operate reliably at low temperatures and high magnetic fields. QTF's are cheap, readily available and large enough to make production of novel sensors relatively easy. SEM analysis of the tungsten tips has shown that the electrochemical etching technique is routinely able to produce tips with typical radii of 30 nm. Dynamic AFM is performed using a frequency-modulation technique. A phase-locked loop (PLL) was used to drive the tuning fork on resonance. A separate feedback loop maintained a constant oscillation amplitude. This technique enabled the frequency shift and dissipation of the tuning fork to be measured separately. These measurements can be related to the conservative and non-conservative components of the tip-sample force respectively.

8.1.2 SCM measurements

A capacitance detector based on an RF tuned filter design was implemented. This enabled capacitance measurements to be made with a resolution of 0.1 aF with a bandwidth adequate for scanning. The tuned filter approach was chosen as it could be implemented with the constraints of limited space, low-temperature and high magnetic field. An equivalent circuit model of the tuned filter was developed and detailed calibrations of the individual components were made. This model was successful in reproducing the experimentally measured response. The oscillation of the tuning fork modulates the tip-sample capacitance. This modulation was used to isolate the local contribution to the tip-sample capacitance from a huge background.

8.1.3 Measurements of a gold film

The tip-sample system was modelled by an RC circuit. The tip-sample coupling is represented by a capacitance and the sample as a resistive plate. Using analytical analysis of the tuned filter and tip-sample interaction it was possible to demonstrate that over a highly conductive surface then the $\hat{Y}$ measurement can be interpreted as

the tip-sample capacitance.

The tip-oscillation is typically much larger than the length scale of the tip-sample interaction and complicates the interpretation of the measured quantities. The capacitance as a function of tip-sample separation, $C(z)$ was extracted from the measured quantities with a deconvolution scheme usually used for tip-sample forces. Point spectra measurements were made with different oscillation amplitudes and the tip-sample force and capacitance were reconstructed from each. The reconstructed curves were essentially identical which demonstrated the validity of the deconvolution technique. The tip-sample force had a length scale much larger than theoretical predictions but was comparable to experiments under similar conditions in the literature. The larger length scale is attributed to electrostatic forces originating from the tip-sample work function difference and distortion of the tip and sample at the smallest separations. The tip-sample capacitance variation was found to be a few aF/nm at the smallest separations. The form of the curve was fitted to a simple analytical expression. At the smallest separations the interpretation is more difficult as the $C(z)$ curve is modified by the tip coming into contact with the surface.

8.1.4 Measurements of a 2DEG

Measurements were made on Hall bar devices fabricated from a GaAs/GaAlAs heterostructure with a 2DEG 50 nm below the surface. At zero-field scans were made close to the physical edge of the device. High contrast is seen between the regions on and off the device which demonstrated the measurement technique is sensitive to the presence of a sub-surface 2DEG. A depletion region parallel to the edge of the device was observed with a length scale comparable to theoretical predictions. Finite element simulations were performed to understand the geometric effect of a step edge on the tip-sample capacitance.

Point spectroscopy measurements were made over the bulk region of the device as a function of magnetic field. Oscillations in the signal were observed with $1/B$ periodicity. With some simple modelling it was possible to show that the $\hat{Y}$ measurement can be

interpreted as local conductivity.

At non integer filling factors signal over the 2DEG is homogeneous (apart from artefacts caused by topographic features) similar to the zero-field case. At integer filling factors the bulk becomes insulating and a highly conductive stripe forms at the edge of the sample. A series of images were taken at filling factors around $\nu = 2$ and $\nu = 4$ and the evolution of the stripe has been observed. The variation of the stripe with filling factor is qualitatively in agreement with theoretical predictions. It is difficult to make quantitative predictions as at low filling factors the theory is only valid for small deviations from integer filling.

Measurements were made in a different position along the edge close to where some point spectroscopy had been performed. An anomalously broadened stripe was seen around a locally depleted region of the 2DEG. The local depletion is attributed to charging of the surface by the point spectroscopy measurements and the increased width to a shallower potential gradient compared to the physical sample edge.

Images of the edge were made close to $\nu = 2$ whilst passing a current through the sample. At some critical current this stripe structure is no longer seen and the signal over the 2DEG becomes homogeneous. Measurements made on the same wafer indicate that this current is about the right order of magnitude to cause breakdown of the quantum Hall effect and this might be associated with the disappearance of the stripe. These measurements are difficult to interpret as transport measurements were not made at the same time. However, this does demonstrate that it is possible to image at the edge of a real device whilst passing current, something that has not been demonstrated in the literature.

8.2 Suggestions for future work

Some suggestions for improvements to the microscope and other types of measurements that could be made are outlined in this section.

8.2.1 Microscope

The features seen at the sample edge are on a length of a micron at low integer filling factors. At higher filling factors and away from integer filling factors the stripe structure exceeds the scan range of the microscope. A larger scan range would be a big improvement and could be achieved by replacing the scan tube with one with a smaller diameter and greater length.

Etched tungsten tips are easy to fabricate but the oxide layer on the surface makes it difficult to predict the work function of the tip. The tip material could be replaced with a PtIr alloy, this is more difficult to sharpen but does not form an oxide layer.

In some measurements contamination of the surface is seen, one cause of this might be water vapour condensing on to the sample whilst loading the microscope into the cryostat. A heater could be incorporated into the sample mount to prevent this happening.

The z coarse positioner is the most unreliable part of the microscope and needs careful adjustment of the clamping springs to make it operate correctly at low temperature. There were a number of measurement runs where the motor did not function at low temperature or slipped during the cool down. Work needs to be done to improve this part of the microscope.

The main source of noise in the AFM measurements is mechanical vibrations caused by acoustic excitation of the cryostat by the vacuum pump. Work is under way to relocate the pump outside the laboratory.

8.2.2 Measurements

The surface of the gold sample had topographic features with a height of 10 nm. The point spectra measurements were made over similar length scale and it might be better to repeat this measurements with a flatter sample, for example highly-orientated pyrolytic graphite (HOPG). To study the effect of the topography on the capacitance signal then a sample with a well defined set of topographic features would be required, for example a grating with a metallic coating.

The scanning measurements close to the edge of 2DEG could be improved by scanning a larger area and making measurements at more magnetic fields. It would be interesting to make measurements on a narrower Hall bar, 50 μm for example, where it is possible to image across the whole width of the device in a few scans. A sample with a lower density would make it possible to image around filling factor $\nu = 1$.

The measurements as a function of applied current need to be repeated with simultaneous transport measurements. In a large device then the most likely place that quantum hall breakdown would originate is close to the contacts. A better device to study this effect would be a large Hall bar but with a narrow constriction in the middle. Studies in the literature suggest that with this type of sample geometry then the breakdown occurs in this constricted region where the current density is higher [124].

Recent publications have demonstrated transport measurements of the quantum Hall effect in graphene [126]. It would be really interesting to see if it possible to image edge states in this system using our technique.

Appendix A

Analytical model of a 2DEG in a magnetic field

Benedict et al describe an analytical model of a disordered, non-interacting 2DEG in a magnetic field [127]. The model consists of electrons moving in a plane under the influence of a perpendicular magnetic field and some random potential $V(r)$. They consider various statistical forms of the disorder potential and the results for a Gaussian white noise distribution were used in this work. Figure A.1(a) shows the DOS calculated with the analytical model. Figure A.1(b) shows the conductivity calculated with the model and from transport measurements. The adjustable parameters of this model were the Fermi energy, which was calculated from the measured electron density and the size of the disorder potential; this was adjusted so that the widths of the peaks were comparable to those of the measured data.

The analytical model shows the same periodicity as the experimental curve and the conductivities are very similar in magnitude. At higher magnetic fields a change in shape and width of the peaks is seen in the experimental curve and is due to spin splitting which is not included in the model. In the analytical model the DOS is zero between Landau levels and therefore so is the conductivity, in the real sample there would be a finite DOS between Landau levels due to localised states and the conductivity remains finite.

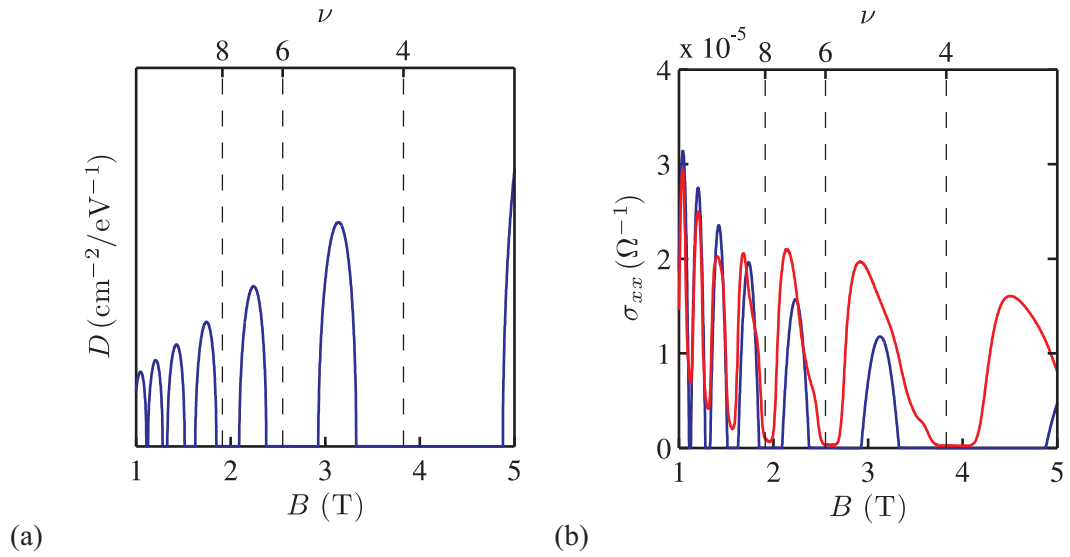

Figure A.1: (a)DOS at the Fermi energy calculated using the analytical model of Benedict et al [127]. (b)Longitudinal conductivity σ_{xx} as a function of magnetic field, (blue) from analytical model, and (red) experimentally measured.

Bibliography

[1] K. von Kiltzing, G. Dorda, and M. Pepper, Phys. Rev. Lett. **45**, 494 (1980).

[2] M. Greiter, Int. J. Mod. Phys. B **13**, 1293 (1998).

[3] A. P. Balachandran, A. Momen, and L. Chandar, Nucl. Phys. B. **461**, 581 (1996).

[4] M. Fabinger, J. High Energy Phys. **5** (2002).

[5] B. Jeckelmann and B. Jeanneret, Rep. Prog. Phys. **64**, 1603 (2001).

[6] G. Nachtwei, Physica E **4**, 79 (1999).

[7] G. Binnig, H. Rohrer, C. Gerber, and E. Weibel, Phys. Rev. Lett. **49**, 57 (1982).

[8] G. Binnig, H. Rohrer, C. Gerber, and E. Weibel, Phys. Rev. Lett. **50**, 120 (1983).

[9] F. J. Giessibl, Science **267**, 68 (1995).

[10] C. D. Frisbie, L. F. Rozsnyai, A. Noy, M. S. Wrighton, and C. M. Lieber, Science **265**, 2071 (1994).

[11] G. J. Leggett, Nanotechnology **17**, 1547 (2006).

[12] G. J. Leggett, Chem. Soc. Rev. **35**, 1150 (2006).

[13] D. M. Eigler and E. K. Schweizer, Nature **344**, 524 (1990).

[14] A. Moser, H. J. Hug, B. Stiefel, and H. J. Guntherodt, J. Magn. Magn. Mater. **190**, 114 (1998).

[15] B. R. Pamplin, *Molecular Beam Epitaxy* (Pergamon Press, 1980).

[16] A. Baumgartner, Ph.D. thesis, ETH Zurich (2005).

[17] J. H. Davies, *The physics of low-dimensional semiconductors: an introduction* (Cambridge university press, 1997), 1st ed.

[18] R. E. Prange and S. M. Girvin, eds., *The quantum Hall effect* (Springer-verlag, 1990), 2nd ed.

[19] A. I. M. Rae, *Quantum Mechanics* (Cambridge university press, 1986), 4th ed.

[20] E. H. Hall, Am. J. Math **2**, 287 (1879).

[21] R. E. Prange, Phys. Rev. B **23**, 4802 (1981).

[22] E. Gornik, R. Lassnig, G. Strasser, H. L. Stormer, A. C. Gossard, and W. Wiegmann, Phys. Rev. Lett. **54**, 1820 (1985).

[23] R. B. Laughlin, Phys. Rev. B **23**, 5632 (1981).

[24] B. I. Halperin, Phys. Rev. B **25**, 2185 (1982).

[25] M. Büttiker, Phys. Rev. B **38**, 9375 (1982).

[26] S. Datta, *Electronic Transport in Mesoscopic Systems* (Cambridge University Press, 1995).

[27] D. B. Chklovskii, B. I. Shklovskii, and L. I. Glazman, Phys. Rev. B **46**, 4026 (1992).

[28] K. Lier and R. R. Gerhardts, Phys. Rev. B **50**, 7757 (1994).

[29] J. P. Eisenstein, L. N. Pfeiffer, and K. W. West, Phys. Rev. B **50**, 1760 (1994).

[30] S. A. Trugman, Phys. Rev. B **27**, 7539 (1993).

[31] R. Woltjer, R. Eppenga, J. Mooren, C. E. Timmering, and J. P. Andre, Europhysics Lett. **2**, 149 (1986).

[32] D. J. Thouless, Phys. Rev. Lett. **71**, 1879 (1993).

[33] K. Tsemekhman, V. Tsemekhman, C. Wexler, and D. J. Thouless, Solid State Commun. **101**, 549 (1997).

[34] E. K. Sichel, H. H. Sample, and J. P. Salerno, Phys. Rev. B **32**, 6975 (1985).

[35] H. Z. Zheng, D. C. Tsui, and A. M. Chang, Phys. Rev. B **32**, 5506 (1985).

[36] G. Ebert, K. von Klizing, and G. Weimann, J. Phys. C **18**, L257 (1985).

[37] P. F. Fontein, K. J. A., P. Hendriks, F. A. P. Blom, J. H. Wolter, H. G. M. Lochs, F. A. J. M. Driessen, L. J. Giling, and C. W. J. Beenakker, Phys. Rev. B **43**, 12090 (1991).

[38] R. Knott, W. Dietsche, K. von Klitzing, K. Eberl, and K. Ploog, Semicond. Sci. Technol. **10**, 117 (1995).

[39] J. Weis, Y. Y. Wei, and K. von Klizing, Physica E **3**, 23 (1998).

[40] T. Chakraborty and P. Pietilainen, *The quantum Hall effects: fractional and integer* (Springer-verlag, 1995), 1st ed.

[41] D. Yoshioka, *The quantum Hall effect* (Springer-verlag, 2002), 1st ed.

[42] N. W. Ashcroft and N. D. Mermin, *Solid state physics* (Saunders College Publishing, 1976).

[43] F. J. Giessibl, Phys. Rev. B **56**, 16010 (1997).

[44] J. Israelachvili, *Intermolecular and Surface Forces* (Academic Press, London, 1991), 2nd ed.

[45] F. Giessibl, Rev. Mod. Phys. **75**, 949 (2003).

[46] G. Binnig, C. F. Quate, and C. Gerber, Phys. Rev. Lett. **56**, 930 (1986).

[47] S. Akamine, R. C. Barrett, and C. F. Quate, Appl. Phys. Lett. **57**, 316 (1990).

[48] Y. Martin, C. C. Williams, and H. K. Wickramasinghe, J. Appl. Phys **61**, 4723 (1987).

[49] D. Sarid, *Scanning Force Microscopy* (Oxford, 1991), 1st ed.

[50] M. Tortonese, R. C. Barrett, and C. F. Quate, Appl. Phys. Lett. **62**, 834 (1993).

[51] T. Itoh, C. Lee, and T. Suga, Appl. Phys. Lett. **69**, 2036 (1996).

[52] P. Günther, U. C. Fischer, and K. Dransfield, Appl. Phys. B: Lasers Opt. **48**, 89 (1989).

[53] F. J. Giessibl, S. Hembacher, H. Bielefeldt, and J. Mannhart, Science **289**, 422 (2000).

[54] F. J. Giessibl and B. G., Ultramicroscopy **42-44**, 281 (1992).

[55] T. R. Albrecht, P. Grütter, D. Horne, and D. Rugar, J. Appl. Phys **69**, 668 (1990).

[56] U. Dürig, O. Züger, and A. Stalder, J. Appl. Phys **727**, 1778 (1992).

[57] F. J. Giessibl and H. Bielefeldt, Phys. Rev. B **61**, 9968 (2000).

[58] M. J. Yoo, T. A. Fulton, H. F. Hess, R. L. Willett, L. N. Dunkleberger, R. J. Chichester, L. N. Pfeiffer, and K. W. West, Science **276**, 579 (1997).

[59] M. Nonnenmacher, M. P. Oboyle, and W. H. K., Appl. Phys. Lett. **58**, 2921 (1991).

[60] J. M. R. Weaver and D. W. Abraham, J. Vac. Sci. Technol. B **9**, 1559 (1991).

[61] K. Okamoto, Y. Sugawara, and S. Morita, Appl. Surf. Sci. **188**, 381 (2002).

[62] Y. Rosenwaks, R. Shikler, T. Glatzel, and S. Sadewasser, Phys. Rev. B **70**, 085320 (2004).

[63] A. Kikukawa, S. Hosaka, and R. Imura, Appl. Phys. Lett. **66**, 3510 (1995).

[64] J. R. Matey and J. Blanc, J. Appl. Phys **57**, 1437 (1985).

[65] C. D. Bugg and P. J. King, J. Phys. E.:Sci. Instrum. **21**, 147 (1988).

[66] R. C. Barrett and C. F. Quate, J. Appl. Phys **70**, 2725 (1991).

[67] C. C. Williams, Annu. Rev. Mater. Sci **29**, 471 (1999).

[68] V. V. Zavyalov, J. S. McMurray, and C. C. Williams, J. Appl. Phys **85**, 7774 (1999).

[69] R. J. Hamers and D. G. Cahill, Appl. Phys. Lett. **57**, 2031 (1990).

[70] R. C. Palmer, E. J. Denlinger, and H. Kawamoto, RCA Rev. **43**, 194 (1982).

[71] S. Lányi, Rev. Sci. Instrum. **73**, 2923 (2002).

[72] T. T., T. Hantschel, S. R., P. De Wolf, W. Vandervorst, L. Hellemans, A. Malave, D. Buchel, E. Oesterschulze, W. Kulisch, et al., J. Vac. Sci. Technol. B **18**, 418 (2000).

[73] S. Sze, *Physics of semiconductor devices* (Wiley New York, 1981), 2nd ed.

[74] K. Goto and K. Hane, Rev. Sci. Instrum. **68**, 120 (1997).

[75] T. Tran, D. R. Oliver, D. J. Thompson, and G. E. Bridges, Rev. Sci. Instrum. **72**, 2618 (2001).

[76] R. Stephenson, A. Verhulst, P. De Wolf, M. Caymax, and W. Vandervorst, Appl. Phys. Lett. **73**, 2597 (1998).

[77] H. Edwards, R. McGlothlin, R. U. E. San Martin, M. Gribelyuk, R. Mahaffy, C. K. Shih, R. S. List, and V. A. Ukraintsev, Appl. Phys. Lett. **72**, 698 (1998).

[78] D. Goghero, V. Raineri, and F. Giannazzo, Appl. Phys. Lett. **81**, 1824 (2002).

[79] J. J. Kopanski and S. Mayo, Appl. Phys. Lett. **72**, 2469 (1990).

[80] G. H. Buh and J. J. Kopanski, Appl. Phys. Lett. **83**, 2486 (2003).

[81] Y. Naitou and N. Ookubo, Appl. Phys. Lett. **85**, 2131 (2004).

[82] E. Meyer, H. J. Hug, and R. Bennewitz, *Scanning probe microscopy: The lab on a Tip* (Springer-Verlag, 2004), 1st ed.

[83] F. D. Callaghan, X. Yu, and M. C. J., Appl. Phys. Lett. **81**, 916 (2002).

[84] F. Giessibl, Appl. Phys. Lett. **73**, 3956 (1998).

[85] J. P. Ibe, P. P. Bey, S. L. Brandow, R. A. Brizzolara, N. A. Burnham, D. P. Dilella, K. P. Lee, C. R. K. Marrian, and R. J. Colton, J. Vac. Sci. Technol. A **8**, 3570 (1990).

[86] Y. Nakamura, Y. Mera, and K. Maeda, Rev. Sci. Instrum. **70**, 3373 (1999).

[87] J. Rychen, T. Ihn, P. Studerus, A. Herrmann, K. Ensslin, H. J. Hug, P. J. A. van Schendel, and H. J. Guntherodt, Rev. Sci. Instrum. **71**, 1695 (2000).

[88] R. D. Grober, J. Acimovic, J. Schuck, D. Hessman, P. J. Kindlemann, J. Hespanha, A. S. Morse, K. Karrai, I. Tiemann, and S. Manus, Rev. Sci. Instrum. **71**, 2276 (2000).

[89] J. E. Sader, T. Uchihashi, M. J. Higgins, A. Farrell, Y. Nakayama, and S. P. Jarvis, Nanotechnology **16**, S94 (2005).

[90] R. V. Jones and J. C. S. Richards, J. Phys. E **6**, 589 (1973).

[91] C. B. Scruby and H. N. G. Wadley, J. Phys. D **11**, 1487 (1978).

[92] M. Avinor and A. Hasson, Journal of Physics E:Scientific Instruments **10**, 771 (1977).

[93] B. Gotsmann, B. Anczykowski, C. Seidel, and H. Fuchs, Appl. Surf. Sci. **140**, 314 (1999).

[94] F. Giessibl, Appl. Phys. Lett. **78**, 123 (2001).

[95] U. Dürig, Appl. Phys. Lett. **75**, 433 (1999).

[96] G. Cross, A. Schirmeisen, A. Stalder, P. Grütter, M. Tschudy, and U. Durig, Phys. Rev. Lett. **80**, 4685 (1998).

[97] H. J. Pain, *The Physics of Vibrations and Waves* (John Wiley and sons, 1993), 4th ed.

[98] K. L. McCormick, M. T. Woodside, M. S. Huang, Wu, P. L. McEuen, C. Duruoz, and J. S. Harris, Phys. Rev. B **59**, 4654 (1999).

[99] M. T. Woodside, V. C., M. P. L., C. Kadow, K. D. Maranowski, and A. C. Gossard, Phys. Rev. B **64**, 041310 (2001).

[100] S. H. Tessmer, P. I. Glicofridis, R. C. Ashoori, L. S. Levitov, and M. R. Melloch, Nature **392**, 51 (1998).

[101] A. Yacoby, H. F. Hess, T. A. Fulton, L. N. Pfeiffer, and W. K. W., Solid State Commun. **111**, 1 (1999).

[102] E. Ahlswede, P. Weitz, J. Weis, K. von Klitzing, and K. Eberl, Physica B **298**, 562 (2001).

[103] P. Weitz, E. Ahlswede, J. Weis, K. von Klitzing, and K. Eberl, Physica E **6**, 247 (2000).

[104] E. Ahlswede, J. Weis, K. von Klitzing, and K. Eberl, Physica E **12**, 165 (2002).

[105] G. Finkelstein, P. I. Glicofridis, S. H. Tessmer, R. C. Ashoori, and M. R. Melloch, Phys. Rev. B **61**, R16323 (2000).

[106] G. Finkelstein, P. I. Glicofridis, R. C. Ashoori, and M. Shayegan, Science **289**, 90 (2000).

[107] G. Finkelstein, P. I. Glicofridis, S. H. Tessmer, R. C. Ashoori, and M. R. Melloch, Physica E **6**, 251 (2000).

[108] P. I. Glicofridis, G. Finkelstein, R. C. Ashoori, and M. Shayegan, Phys. Rev. B **65**, 121312 (2002).

[109] R. C. Ashoori, H. L. Stormer, J. S. Weiner, L. N. Pfeiffer, S. J. Pearton, K. W. Baldwin, and K. W. West, Phys. Rev. Lett. **68**, 3088 (1992).

[110] S. H. Tessmer, Phys. Rev. B **66**, 125308 (2002).

[111] I. Kujanishvili, S. Chakraborty, I. J. Maasilta, S. H. Tessmer, and M. R. Melloch, Ultramicroscopy **102**, 7 (2004).

[112] M. A. Eriksson, R. G. Beck, M. Topinka, K. J. A., R. M. Westervelt, K. L. Campman, and A. C. Gossard, Appl. Phys. Lett. **69**, 671 (1996).

[113] M. A. Topinka, B. J. LeRoy, R. M. Westervelt, S. E. J. Shaw, R. Fleischmann, E. J. Heller, K. D. Maranowski, and A. C. Gossard, Nature **410**, 183 (2001).

[114] M. A. Topinka, B. J. LeRoy, S. S. E. J., E. J. Heller, R. M. Westervelt, K. D. Maranowski, and A. C. Cossard, Science **289**, 2323 (2000).

[115] B. J. LeRoy, M. A. Topinka, R. M. Westervelt, K. D. Maranowski, and A. C. Gossard, Appl. Phys. Lett. **80**, 4431 (2002).

[116] B. J. LeRoy, J.Phys.: Condens. matter **15**, R1835 (2003).

[117] T. Ihn, J. Rychen, T. Vancura, K. Ensslin, W. Wegscheider, and M. Bichler, Physica E **13**, 671 (2002).

[118] S. Kičin, A. Pioda, T. Ihn, K. Ensslin, D. C. Driscoll, and A. C. Gossard, Phys. Rev. B **70**, 205302 (2004).

[119] A. Baumgartner, T. Ihn, K. Ensslin, K. Maranowski, and A. C. Gossard, Phys. Rev. B **76**, 085316 (2007).

[120] A. A. Shashkin, A. J. Kent, P. A. Harrison, L. Eaves, and M. Henini, Phys. Rev. B **49**, 5379 (1994).

[121] R. K. Goodall, R. J. Higgins, and J. P. Harrang, Phys. Rev. B **31**, 6597 (1985).

[122] T. Takamasu, S. Komiyama, S. Hiyamizu, and S. Sasa, Surface science **170**, 202 (1986).

[123] P. Streda and K. von Klitzing, J. Phys. C. **17**, L483 (1984).

[124] L. Eaves and F. Sheard, Semiconductor science and technology **1**, 346 (1986).

[125] S. A. Trugman, Phys. Rev. B **27**, 7539 (1983).

[126] Y. B. Zhang, Y. W. Tan, H. L. Stormer, and P. Kim, Nature **438**, 201 (2005).

[127] K. A. Benedict and J. T. Chalker, J.Phys. C:Solid state Phys. **19**, 3587 (1986).